Understanding Underground Hydrogen Storage Across Scales

Numerical Simulations, Experiments, and Site Selection

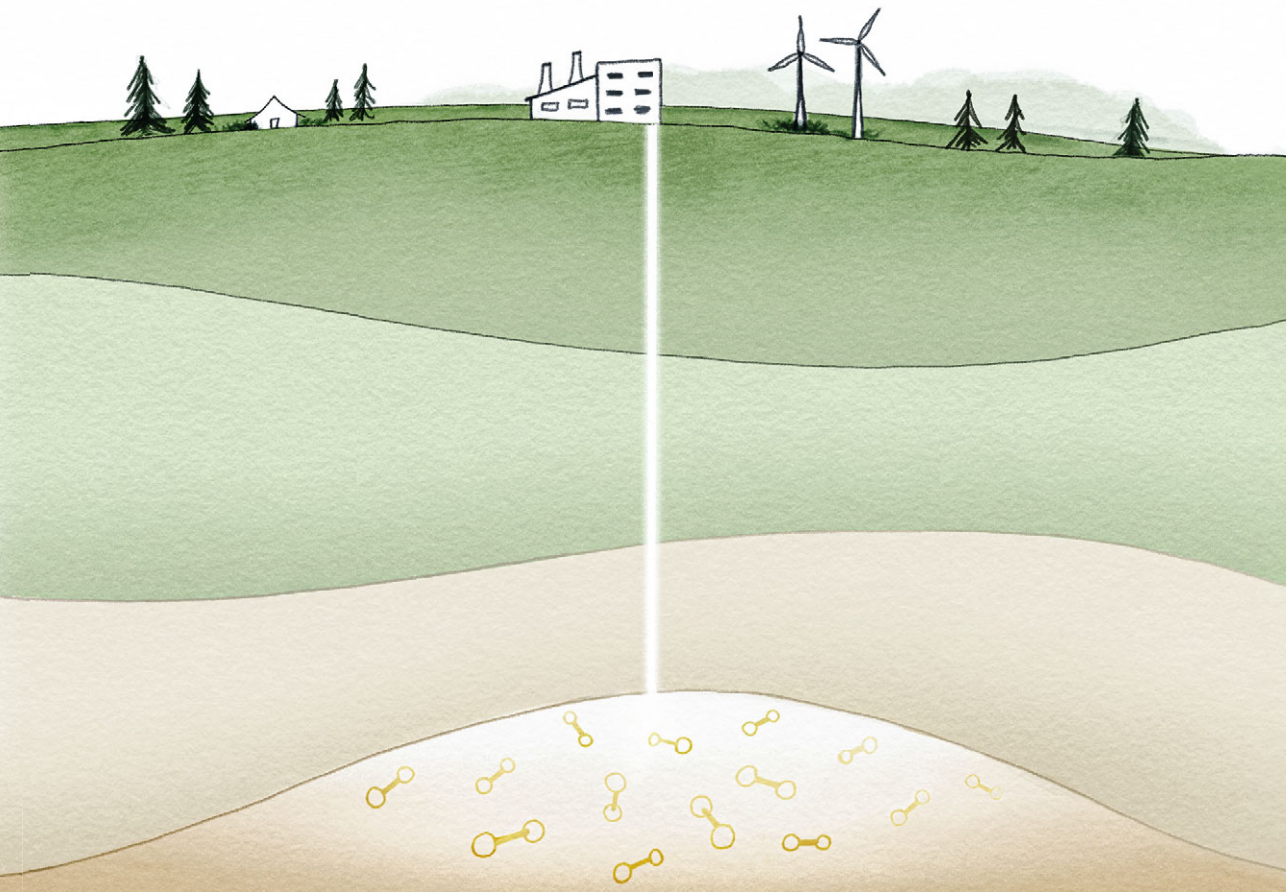

Willemijn van Rooijen

Understanding Underground Hydrogen Storage Across Scales:

Numerical Simulations, Experiments, and Site Selection

Understanding Underground Hydrogen Storage Across Scales:

Numerical Simulations, Experiments, and Site Selection

Proefschrift

ter verkrijging van de graad van doctor
aan de Technische Universiteit Delft,
op gezag van de Rector Magnificus prof. dr. ir. H. Bijl,
voorzitter van het College voor Promoties,
in het openbaar te verdedigen
op dinsdag 24 februari 2026 om 12:30

door

Willemijn Adriënne VAN ROOIJEN

Master of Science in Applied Earth Sciences,
Technische Universiteit Delft, Nederland,
geboren te Nieuwegein, Nederland.

Dit proefschrift is goedgekeurd door de promotoren.

Samenstelling promotiecommissie bestaat uit:

Rector Magnificus,	voorzitter
Prof. dr. H. Hajibeygi,	Technische Universiteit Delft, promotor
Em. prof. dr. ir. J.D. Jansen,	Technische Universiteit Delft, promotor
Onafhankelijke leden:	
Prof. dr. C.A. Peters,	Princeton University
Prof. dr. K. Edlmann,	University of Edinburgh
Prof. dr. ir. E.C. Slob,	Technische Universiteit Delft
Prof. dr. ir. L.J. Sluys,	Technische Universiteit Delft
Prof. dr. P.J. Vardon,	Technische Universiteit Delft, reservelid
Overig lid:	
Dr. M.M. Boon,	University of Stuttgart

Dit onderzoek is uitgevoerd in de ADMIRE-groep aan de TU Delft en financieel ondersteund door NWO.

Keywords: Energy storage, underground hydrogen storage, microfluidic experiments, contact angle measurement, wettability, molecular simulations, pore-scale simulation, multiphase flow, site selection

Printed by: Ridderprint | www.ridderprint.nl

ISBN 978-94-6537-166-5

An electronic version of this dissertation is available at http://repository.tudelft.nl/.

Contents

Summary

To enable the energy transition, renewable energy sources such as wind and solar are playing an increasingly central role. However, their weather-dependent nature makes balancing energy supply and demand challenging. While short-term fluctuations can often be managed with batteries or other local storage solutions, many countries, such as the Netherlands, are expected to face large seasonal energy imbalances of several tens of terawatt-hours (TWh), far beyond the capabilities of conventional technologies such as batteries.

Underground Hydrogen Storage (UHS) has therefore emerged as a promising solution. Storing hydrogen in geological formations such as depleted gas reservoirs or aquifers at depths of several kilometers can provide storage capacities on the order of several terawatt-hours. These reservoirs are porous rocks of solid grains and interconnected voids, where hydrogen is stored in the pore space. This introduces complex flow dynamics and technical challenges across multiple scales: from the molecular interactions of hydrogen with other fluids present in the reservoir, to the flow through micrometer-scale pore channels, up to reservoir-scale processes spanning several kilometers.

This thesis advances the understanding of UHS by addressing knowledge gaps across multiple scales, combining molecular simulations, microfluidic experiments, pore-scale modeling, and the development of a site selection framework.

At the molecular scale, missing datasets of thermophysical properties of hydrogen–brine systems were obtained by using molecular simulations. These properties, including densities, viscosities, interfacial tensions, solubilities, and diffusivities, are essential for accurate large-scale reservoir simulations.

At the pore scale, microfluidic experiments were conducted to measure dynamic contact angles in glass micromodels that mimic the micrometer-scale channels of porous rocks. These measurements reveal how wettability depends on pore geometry and governs flow dynamics. Complementary pore-scale simulations using the lattice Boltzmann method were performed to explore mechanisms of hydrogen trapping and bypassing under varying flow rates, pore shapes, and capillary conditions. Together, these results improve our understanding of multiphase flow processes critical for predicting and maximizing hydrogen flow behaviour and recovery efficiency.

At the reservoir scale, a systematic site selection framework was developed for identifying suitable depleted gas fields for UHS. This framework integrates multidisciplinary criteria including reservoir performance, geomechanical stability, bio-geochemistry, and techno-economic feasibility providing a practically accessible and reliable method for screening and ranking potential storage sites.

By linking insights across scales and disciplines, this thesis strengthens the scientific foundation for the safe, efficient, and reliable deployment of UHS. The findings contribute critical data, improve predictions, and support decision-making toward enabling large-scale UHS.

Samenvatting

Om de energietransitie mogelijk te maken, spelen hernieuwbare energiebronnen zoals wind en zon een steeds centralere rol in ons energiesysteem. Hun weersafhankelijke karakter maakt het echter uitdagend om vraag en aanbod van energie in balans te houden. Terwijl korte termijn schommelingen vaak kunnen worden opgevangen met batterijen of andere lokale opslagoplossingen, zullen veel landen, zoals Nederland, te maken krijgen met een grote seizoensgebonden energiedisbalans van enkele tientallen terawattuur (TWh). Deze overschotten en tekorten overstijgen ruimschoots de opslagcapaciteit van conventionele technologieën zoals batterijen.

Ondergrondse waterstofopslag (UHS) is daarom naar voren gekomen als een veelbelovende oplossing. Het opslaan van waterstof in geologische formaties zoals lege gasvelden of diepe zoutwateraquifers op enkele kilometers diepte kan opslagcapaciteiten bieden in de orde van meerdere terawattuur. Deze reservoirs bestaan uit poreuze gesteenten, opgebouwd uit vaste korrels en onderling verbonden poriën, waarin de waterstof wordt opgeslagen. Dit leidt tot complexe stromingsdynamica en technische uitdagingen op verschillende schalen: van de moleculaire interacties van waterstof met andere vloeistoffen aanwezig in het reservoir, via de stroming door micrometer-kanalen, tot processen op reservoirschaal die zich uitstrekken over meerdere kilometers.

Dit proefschrift draagt bij aan een beter begrip van ondergrondse waterstofopslag door kennishiaten op verschillende schalen te adresseren, met behulp van moleculaire simulaties, microfluïdische experimenten, porieschaalmodellering en de ontwikkeling van een locatieselectiekader.

Op moleculair niveau zijn uitgebreide datasets verkregen van de thermofysische eigenschappen van systemen van waterstof en reservoirvloeistoffen met behulp van moleculaire simulaties. Deze eigenschappen, waaronder dichtheden, viscositeiten, grensvlakspanningen, oplosbaarheden en diffusiviteiten, zijn essentieel voor het uitvoeren van nauwkeurige grootschalige reservoirsimulaties.

Op porieschaal zijn microfluïdische experimenten uitgevoerd om dynamische contacthoeken te meten in glazen micromodellen die de micrometerschaalkanalen van poreuze gesteenten nabootsen. Deze metingen laten zien hoe contacthoeken afhankelijk zijn van de breedte van de kanalen, wat van belang is voor het begrijpen van multifase stromingsprocessen. Daarnaast zijn porieschaalsimulaties uitgevoerd met de lattice Boltzmann-methode om mechanismen van opgesloten waterstof te onderzoeken, de fractie die in de poriën achterblijft en niet kan worden teruggewonnen. De simulaties werden uitgevoerd bij verschillende stromingssnelheden en poriegeometrieën en vergeleken met andere gassen. Gezamenlijk verbeteren deze resultaten ons inzicht in multifase stromingsprocessen die cruciaal zijn voor het voorspellen en maximaliseren van het rendement van waterstofterugwinning.

Op reservoirschaal is een systematisch locatieselectiekader ontwikkeld voor het identificeren van geschikte lege gasvelden voor ondergrondse waterstofopslag op basis van de

verschillende eigenschappen die de reservoirs kenmerken. Dit kader integreert multidisciplinaire criteria, waaronder reservoirprestaties, geomechanische stabiliteit, bio-geochemische interacties en techno-economische haalbaarheid en biedt zo een praktisch en betrouwbaar hulpmiddel voor het screenen en rangschikken van potentiële opslaglocaties.

Door inzichten over verschillende schalen en disciplines te verbinden, versterkt dit proefschrift de wetenschappelijke basis voor de veilige, efficiënte en betrouwbare toepassing van ondergrondse waterstofopslag. De bevindingen leveren cruciale gegevens, verbeteren de voorspellende mogelijkheden en ondersteunen besluitvorming voor de implementatie van grootschalige ondergrondse waterstofopslag.

1

Introduction

1

1.1 Motivation

Climate change presents an urgent global challenge, attracting growing attention from scientists, companies, policymakers, the media, and the general public. To reduce greenhouse gas emissions, the energy system is shifting toward renewable sources such as wind and solar power. However, the inherent intermittency of these sources complicates the balance between supply and demand, making large-scale energy storage a critical component of a sustainable energy system [1–4].

While short-term storage solutions, such as home battery systems, are effective for daily or weekly fluctuations, many regions experience seasonal mismatches between energy generation and consumption. For example, in the Netherlands, it is estimated that annual seasonal energy storage requirements will reach tens of terawatt-hours (TWh) by 2050 [5]. Conventional storage options, such as electrochemical batteries or above-ground pressurized tanks, cannot provide such capacities [5].

Hydrogen (H_2) is recognized as a key energy carrier due to its high energy content per unit mass and clean combustion byproducts [4, 6–8]. Storing large quantities of hydrogen in geological formations, referred to as Underground Hydrogen Storage (UHS), provides a promising solution to the long-standing challenge of large-scale energy storage needed for the energy transition [9–12].

1.2 Underground Hydrogen Storage (UHS)

Hydrogen can be stored in various geological formations, including lined rock caverns, salt caverns, depleted gas reservoirs, and deep saline aquifers (Figure 1.1) [9–13]. Among these, salt caverns currently have the highest Technology Readiness Level (TRL) [14, 15], offering several advantages such as high gas purity, efficient cycling performance, and rapid production rates[11]. On the other hand, the volumetric storage capacity of porous formations, such as depleted gas reservoirs or aquifers, is significantly larger [16–18]. Of these, depleted gas reservoirs are generally preferred over aquifers due to their proven sealing integrity, detailed reservoir characterization, and existing infrastructure [19].

The capacity of a single salt cavern is typically in the order of 0.1-0.25 TWh, while lined rock caverns provide only about 0.01–0.03 TWh. By contrast, depleted gas fields can offer storage capacities of up to several tens of TWh [14, 15]. As an example, in the Netherlands, the projected hydrogen storage demand for 2050 is estimated to be 7 - 18.5 TWh [5]. This highlights that while salt caverns and lined rock caverns are well-suited for short-term system flexibility, seasonal storage will likely require porous reservoirs such as depleted gas fields. For this reason, this thesis is focussed on hydrogen storage in porous media.

The idea of a “hydrogen economy” has been discussed for decades [20], yet systematic investigation of UHS has only recently gained significant momentum. While large-scale underground storage of pure hydrogen remains relatively novel, underground gas storage (UGS) has been widely practiced since the 1950s [15]. Several early UGS projects stored town gas, a blend of hydrogen and methane (approximately 50–60% hydrogen), providing a valuable foundation for UHS development and demonstrating the feasibility of subsurface hydrogen storage. There are also two early examples of pure hydrogen storage: the first dedicated underground hydrogen site was established in 1972 in Teesside, UK, using small salt caverns with a capacity of only 30 GWh [21], followed by larger and deeper caverns

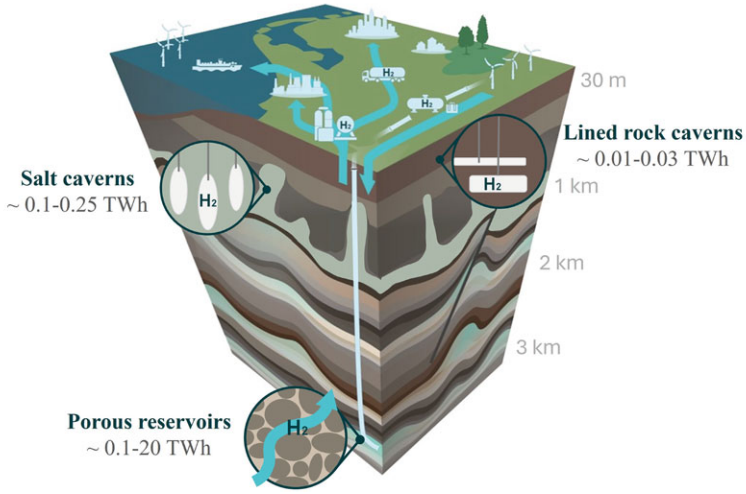

Figure 1.1: Schematic geological cross-section showing various types of underground hydrogen storage technologies and their typical storage capacity ranges. Numbers are taken from [14, 15].

in Texas, USA, in 1983 with a capacity of 157.4 GWh [22]. Both sites remain operational today [21].

Despite these early examples, the scale of commercial UHS deployment remains limited. So far, no commercial projects aim to provide seasonal energy balancing [15]. However, interest has grown rapidly in recent years, leading to numerous pilot and demonstration projects worldwide. Regarding UHS in porous media, in Argentina, the Hychhio pilot project is testing a hydrogen/methane blend in depleted gas fields [22], and a pilot project in Austria is testing pure hydrogen storage in a depleted gas field, and preliminary results are promising [23, 24]. Nevertheless, UHS in salt caverns is closest to commercial readiness, whereas UHS in porous reservoirs is less mature and requires further technical validation. Besides the few operational projects, numerous additional pilot projects in both salt caverns and depleted fields have been announced or are being prepared for development [15].

1.3 Key challenges of UHS in porous reservoirs

Porous reservoirs, such as depleted gas fields and deep saline aquifers, offer substantial potential for large-scale UHS, but their deployment is associated with several technical and operational challenges, which should be carefully considered for safe and efficient implementation. Due to hydrogen's unique thermophysical properties, such as its low density and viscosity compared to other gases, flow patterns can be significantly different compared to the storage of natural gas or CO_2 [25]. Processes such as gravity override, viscous fingering, phase segregation, and upconing can strongly influence the spatial distribution of hydrogen within the reservoir and affect its overall recoverability. Furthermore, gas mixing and residual trapping reduce the fraction of retrievable hydrogen and thereby impact storage efficiency [11]. Hydrogen's small molecular size and high diffusivity could

potentially introduce additional containment challenges, particularly in the presence of old wells, faults, or imperfect sealing formations, making thorough site characterization and well integrity assessments essential [19].

Cyclic injection and withdrawal of hydrogen impose repeated pressure fluctuations on the subsurface, altering the local stress regime and potentially inducing rock deformation. These variations can modify porosity and permeability, reduce caprock sealing capacity, and in some cases trigger induced seismicity through fault reactivation, subsidence, uplift, or wellbore instability [11, 19, 26]. In addition, introducing hydrogen into porous formations disturbs the existing geochemical equilibrium between reservoir fluids, dissolved gases, and the surrounding rock matrix, potentially initiating a range of reactions that affect both storage performance and integrity [11]. Hydrogen also acts as an electron donor for various microbial communities present in the subsurface [27, 28], which can consume hydrogen or produce unwanted byproducts such as hydrogen sulphide. These bio-geochemical processes may reduce usable storage capacity, degrade gas quality, promote biofilm formation, clog flow pathways, alter injectivity through mineral dissolution or precipitation, and compromise caprock sealing integrity [11, 27, 29].

Despite significant progress in laboratory experiments and pilot studies, the coupled effects of geochemistry, microbiology, geomechanics, and multiphase flow in porous formations remain a challenge. This knowledge gap highlights the importance of ongoing field-scale demonstrations and integrated monitoring strategies to de-risk large-scale UHS deployment [15].

1.4 Understanding UHS across scales and disciplines

From the wide variety of risks that may play a role in UHS in porous media, it becomes clear that implementing this technology involves both multiscale and multidisciplinary challenges. Safe and efficient UHS systems require understanding processes across a range of scales from the molecular behavior of hydrogen at the nanometer scale to reservoir-scale dynamics spanning several kilometers. Because hydrogen is stored in porous media, resulting in complex flow behaviour, understanding the processes at intermediate scales (e.g. mm, cm, and dm) becomes particularly important.

In addition to these scale-related complexities, UHS research spans multiple disciplines, including bio-geochemistry, reservoir engineering and multiphase flow, geomechanics, and techno-economic site assessment. Within reservoir engineering and multiphase flow, both thermodynamics and hydrodynamics play a central role, providing essential inputs for reservoir-scale investigations. Addressing these challenges requires a combination of experimental studies, numerical modeling, and field-based investigations, together with the integration of insights from these diverse fields. Figure 1.2 illustrates the range of relevant scales and highlights examples of research approaches commonly used in UHS, as well as the types of insights they provide.

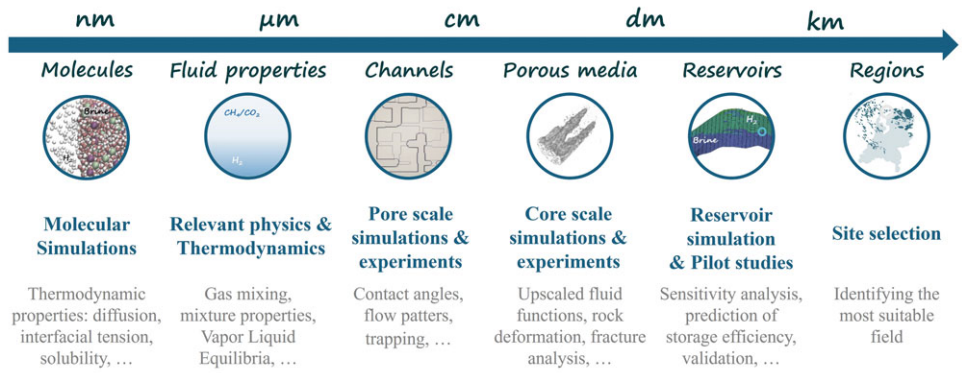

Figure 1.2: Schematic overview of the scales and corresponding structures relevant to UHS in porous media (top arrow). Example research methods are shown beneath each scale, along with the types of insights or results these methods can provide (bottom). Images are taken from [30–32]

1.5 Research goals and approaches

Underground Hydrogen Storage in porous media is receiving increasing attention as a key enabling technology for large-scale, seasonal energy storage, and getting closer to implementation [15]. However, despite this growing interest, many fundamental questions remain unanswered across various scales. Improving our understanding of UHS systems is essential to ensure their safe, efficient, and reliable implementation.

The overarching goal of this thesis is to advance the understanding of UHS processes in porous media across multiple scales and disciplines by addressing a set of research questions that remained unresolved at the time of this work. To achieve this, the following objectives were defined:

1. **Establish missing thermophysical datasets:** Generate essential data for the hydrogen–brine system, including densities, viscosities, interfacial tensions, solubilities, and self-diffusivities, to enable more accurate reservoir-scale simulations.

2. **Characterize dynamic wetting behavior:** Quantify dynamic contact angles relevant for UHS and investigate their dependency on channel width to improve the understanding of upscaled fluid functions.

3. **Understanding trapping mechanisms:** Study the underlying geometrical and operational controls on hydrogen trapping.

4. **Develop a site screening and selection framework:** Establish a methodology to identify suitable depleted gas fields for UHS by integrating reservoir performance, geomechanics, bio-geochemistry, and techno-economics into a unified decision-support framework.

By linking these scales and combining computational, experimental, and theoretical approaches, this thesis aims to build a comprehensive understanding of the governing processes in UHS systems in porous media. The findings help understanding UHS systems

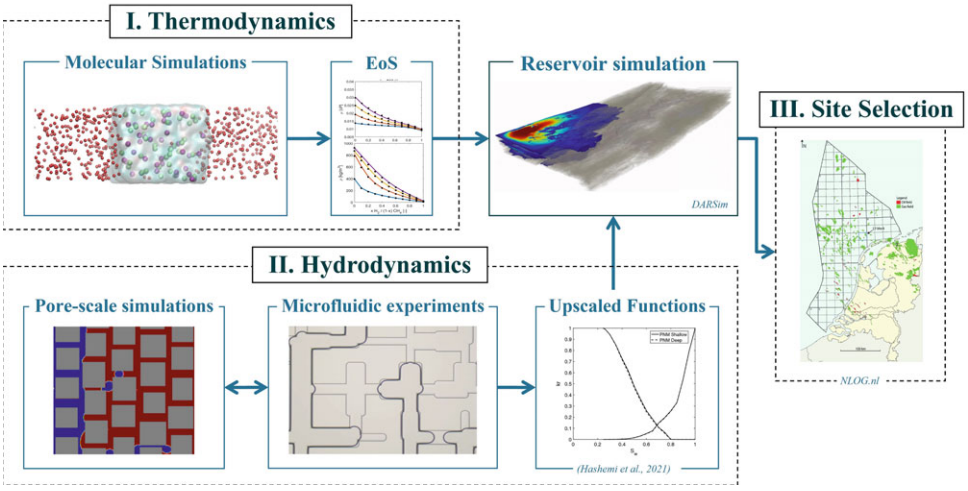

Figure 1.3: Schematic overview of how various subprojects of this thesis are connected and how they can contribute to the understanding of UHS.

and provide insights that support the safe and efficient large-scale deployment of hydrogen storage in porous media.

Achieving these objectives required combining complementary methods across multiple scales and disciplines, ranging from molecular simulations to site selection. The input for reservoir simulations can be subdivided into thermodynamics and hydrodynamics, which are both adressed in this thesis. The following sections provide a general introduction of each approach and its role within this thesis. Figure 1.3 summarizes how these methodologies are connected and how they contribute to the individual research objectives.

1.5.1 Molecular simulations

Molecular simulations provide a powerful tool to investigate the thermophysical properties of the hydrogen–brine system under a wide range of pressures, temperatures, and salinities that are often challenging or expensive to access experimentally. Molecular simulations are a complementary approach to experiments to obtain accurate and large datasets at a wide range of conditions. Molecular dynamics (MD) simulations track the trajectories of individual atoms and molecules over time by solving Newton's equations of motion, using interatomic force fields to describe their interactions [33]. Monte Carlo (MC) simulations explore the statistical behavior of molecular systems by sampling a wide range of configurations based on probabilistic rules [33]. Using these methods, key properties including densities, viscosities, interfacial tensions, solubilities, and self-diffusivities were computed for conditions relevant to UHS. The resulting datasets are essential inputs for developing accurate equations of state (EoS), which form a key building block for modeling thermodynamic processes, and they also directly support reservoir-scale simulations by providing reliable property data where experimental measurements are scarce or inconsistent.

1.5.2 Microfluidic experiments

Microfluidic experiments provide an effective approach to study hydrodynamical pore-scale processes [34]. In these experiments, transparent micromodels with engineered geometries are used to directly visualize the displacement of fluids and to measure key properties such as dynamic contact angles. Unlike natural rock samples, where the complex pore structure makes systematic analysis challenging [35, 36], microfluidic systems allow for controlled variation of channel widths and wettability, enabling a direct assessment of how pore size influences hydrogen–brine contact angles. Understanding the wettability of a system is essential, as contact angles strongly affect residual trapping and multiphase flow dynamics, which in turn govern the shape of upscaled fluid functions such as relative permeability and capillary pressure curves. These fluid functions form a critical input for reservoir simulations, and accurate parameterization is therefore vital for predicting the performance and efficiency of UHS systems [31].

1.5.3 Pore-scale simulations

Pore-scale simulations provide a numerical framework to study multiphase flow mechanisms in porous geometries under controlled conditions relevant to UHS [37–43]. In this work, the lattice Boltzmann method (LBM) [44] is employed, which simulates fluid flow by tracking the evolution of particle distribution functions on a discrete lattice using the Boltzmann equation [45]. These hydrodynamic simulations allow for systematic investigation of how physical and geometrical factors, such as channel width ratios, pore shapes, flow rates, and fluid properties, control residual trapping. The results provide quantitative insights into pore-scale mechanisms governing hydrogen mobility and bypassing, which are essential for deriving accurate upscaled fluid functions, such as relative permeability and capillary pressure, that serve as critical inputs for reservoir-scale simulations of UHS performance.

1.5.4 Site selection

Selecting suitable sites for UHS is critical to ensuring safe, reliable, and efficient systems [46]. In the Netherlands, there are around 500 depleted gas fields with varying geological and operational characteristics [32], making a structured framework essential to identify the most promising candidates efficiently. Site selection involves assessing a wide range of interdisciplinary factors, including reservoir performance (e.g., injectivity and deliverability), geomechanical stability, containment security, bio-geochemical interactions, and techno-economic feasibility. Developing an effective screening framework therefore requires defining the most relevant criteria to systematically rank and eliminate potential sites. These criteria should ideally be grounded in scientific evidence and obtained across multiple scales. For example, reservoir-scale sensitivity analyses help identify parameters that dominate storage performance, pore-scale studies reveal how rock properties affect hydrogen trapping or hydrodynamic flow behaviour, and thermodynamic studies help understanding how operational conditions influence fluid properties and therefore provide additional insights into the efficiency of UHS systems.

1

1.6 Thesis outline

This thesis is structured into three main parts, six chapters and two appendices as follows:

- **Part I: Thermodynamics**
  - **Chapter 2:** Presents *molecular simulations* to obtain missing thermophysical datasets, including densities, viscosities, interfacial tensions, solubilities, and self-diffusivities of the H_2/brine system under reservoir-relevant conditions. These datasets are essential inputs for equations of state and reservoir-scale modeling.
- **Part II: Hydrodynamics**
  - **Chapter 3:** Reports on *microfluidic experiments* designed to measure dynamic contact angles of H_2/brine systems across a range of channel widths. The results provide insights into wettability behavior at the pore scale and its influence on upscaled flow functions relevant to UHS.
  - **Chapter 4:** Investigates residual hydrogen trapping mechanisms through *pore-scale simulations* using the lattice Boltzmann method. The study explores the effect of pore geometry, channel width ratios, flow conditions, and fluid properties on bypass trapping phenomena.
- **Part III: Site selection**
  - **Chapter 5:** Develops a systematic framework for *site selection* of underground hydrogen storage in depleted gas reservoirs. The framework integrates reservoir simulations, sensitivity analyses, and findings from targeted studies at smaller scales from literature to identify the most influential selection criteria and enable efficient field ranking.
- **Chapter 6:** Summarizes the main findings of this thesis, integrates insights across different scales, and provides recommendations for future research directions.
- **Appendix A:** Provides supplementary details on the microfluidic experiments, including sensitivity analyses and method validation.
- **Appendix B:** Presents the derivation of a full set of dimensionless variables describing the functional dependence of trapped saturation, complementing the theoretical analysis in Chapter 4.

I

Thermodynamics

2

Molecular Simulations: Thermophysical properties of the Hydrogen/Brine system

Data for several key thermodynamic and transport properties needed for technologies using hydrogen (H_2), such as underground H_2 storage and H_2O electrolysis are scarce or completely missing. Force field-based Molecular Dynamics (MD) and Continuous Fractional Component Monte Carlo (CFCMC) simulations are carried out in this work to cover this gap. Extensive new data sets are provided for (a) Interfacial tensions of H_2 gas in contact with aqueous NaCl solutions for temperatures of (298 to 523) K, pressures of (1 to 600) bar, and molalities of (0 to 6) mol NaCl/kg H_2O, (b) self-diffusivities of infinitely diluted H_2 in aqueous NaCl solutions for temperatures of (298 to 723) K, pressures of (1 to 1000) bar, and molalities of (0 to 6) mol NaCl/kg H_2O, and (c) solubilities of H_2 in aqueous NaCl solutions for temperatures of (298 to 363) K, pressures of (1 to 1000) bar, and molalities of (0 to 6) mol NaCl/kg H_2O. The force fields used are the TIP4P/2005 for H_2O, the Madrid-2019 and the Madrid-Transport for NaCl, and the Vrabec and Marx for H_2. Excellent agreement between the simulation results and available experimental data is found with average deviations lower than 10%.

This chapter was published in the Journal of Chemical & Engineering Data **Vol. 69(2)**, (2023) [47].

2.1 Introduction

Due to the vastly growing global energy demand and the resulting climate change, a transition from fossil-fuel based energy production to clean renewable energy production is crucial [1, 2]. As a green energy carrier, hydrogen (H_2) plays a crucial role in this transition, because of its high gravimetric energy density and clean combustion products [6–8]. Important technologies in the H_2 value chain include underground H_2 storage [9, 12, 16, 48] and H_2O electrolysis [49, 50]. To enable the design and optimization of these technologies, accurate knowledge of thermodynamic, interfacial, and transport properties of H_2 is essential [9, 51–54]. More specifically, the diffusivities and solubilities of H_2 in aqueous solutions, and the interfacial tensions of H_2 gas in contact with aqueous electrolyte solutions are crucial properties. The interplay of these properties determine the efficiency of the technologies, and allow for accurate predictions of the processes involved, which are e.g., required for safety. These properties depend on pressure, temperature, and salt concentration [55]. H_2 technologies cover a wide range of operational conditions. For example, in underground H_2 storage sites, the pressure, temperature, and salt molality can be as high as 300 bar, 333 K, and 5 mol NaCl/kg H_2O, respectively [12]. Typically, H_2O electrolysers operate at atmospheric pressure, temperatures of ca. (348 to 372) K, and molalities of ca (3 to 4) electrolyte/kg H_2O [56, 57]. Other types of electrolysis require much higher pressures and temperatures, i.e., up to 700 bar and 1400 K, respectively [58–60]. Thus, to cover the conditions for important H_2 applications, the interfacial tensions, self-diffusivities, and solubilities need to be available for a very wide range of pressures, temperatures, and salt concentrations.

Traditionally, these thermophysical properties are measured experimentally [61–63]. Nevertheless, only a small number of experimental studies on the interfacial tension of H_2/pure H_2O [35, 61, 64–66] is available, while only two studies report measurements of interfacial tension of H_2/aqueous solutions (with NaCl and NaCl+KCl) [35, 66]. These experiments are performed by using the capillary rise [67] and the pendant drop [35, 64, 66, 68] techniques. Interfacial tensions of H_2/aqueous solutions are reported for temperatures up to 423 K, pressures up to 345 bar, and molalities of up to 5 mol (NaCl + KCl)/kg H_2O. As far as the solubility of H_2 in aqueous NaCl solutions is concerned, for an overview of the available experimental data the reader is referred to the works of Chabab *et al.* [69], Torín-Ollarves and Trusler [70], and Ansari *et al.* [71]. Although a lot of experimental data are available for H_2 in pure H_2O, solubility measurements of H_2 in aqueous NaCl solutions are scarce, and in many cases conflicting [62, 69, 72–76]. The two main sources of experimental data of solubilities of H_2 in aqueous solutions at concentrations above 1 mol NaCl/kg H_2O, at temperatures above 300 K, and at pressures above 10 bar by Torín-Ollarves and Trusler [70], and Chabab *et al.* [69] show conflicting results as the measured solubilities differ by ca. 30%. For the self-diffusivity of H_2 in H_2O, experimental data are available [63, 77–84] but mostly at atmospheric pressure and for limited temperatures below 340 K. Similarly to the solubilities, the experimental measurements also differ by up to 70 %. To the best of our knowledge, no experimental data are available for the self-diffusivity of H_2 in aqueous NaCl solutions.

Based on the available experimental data, it is evident that only a limited range of the required interfacial tensions, solubilities, and self-diffusivities of the H_2/H_2O/NaCl system has been measured, while in some cases, there are significant discrepancies between the

data reported from different sources. The reason for the scarcity of and deviation in the data may be that experimental measurements are rather challenging and expensive to perform, especially at high pressures and temperatures. To this end, a widely used complementary approach for obtaining thermophysical data is molecular simulation, especially at conditions which are challenging for experimental measurements.

Numerous studies have used Molecular Dynamics (MD) to compute the interfacial tension of gases (e.g., CO_2, CH_4) and liquids (e.g., hydrocarbons) in contact with H_2O (pure or saline) [85–95]. However, no molecular simulation studies on the interfacial tension of H_2 and aqueous solutions are available. MD simulations have also been performed to compute self-diffusivities (i.e., self-diffusion coefficients) of H_2 in pure H_2O [96–100]. Recently, Tsimpanogiannis *et al.* [98] reported such data for pressures in the range of (1 to 2000) bar and temperatures in the range of (275 to 975) K spanning vapor, liquid, and supercritical H_2O. The Marx [101], Vrabec [102], Buch [103], Hirschenfelder [104], Cracknell [105], and Silvera-Goldman [106] H_2 force fields were used in combination with the TIP4P/2005 [107] H_2O force field. The Buch [103] and Vrabec [102] H_2 force fields were shown to yield the best agreement with experimental data. In contrast, self-diffusivities of H_2 in aqueous NaCl solutions computed from MD simulations have not yet been reported, while there are a few studies available reporting computations of self-diffusivities of CO_2 in aqueous NaCl solutions [108–111]. Lopez-Lazaro *et al.* [112] have computed solubilities of H_2 in aqueous NaCl solutions using Monte Carlo (MC) simulations for molalities up to a maximum of 2 mol NaCl/kg H_2O. To the best of the authors knowledge, this was the only molecular simulation study on H_2 solubilities in aqueous NaCl solutions. Molecular simulations have been used for computing solubilities of other gases (e.g., CO_2, CH_4) in water and aqueous NaCl solutions [90, 95, 113–115].

Despite the urgency and importance of reliable data of interfacial tension of H_2 in contact with aqueous NaCl solutions, self-diffusivity of H_2 in aqueous NaCl solutions, and solubility of H_2 in aqueous NaCl solutions, only very limited experimental and simulation studies are available. The objective of this work is to generate reliable data for these properties for a wide range of conditions relevant to H_2 technologies, such as underground H_2 storage and H_2O electrolysis. We present new data sets of (a) interfacial tensions of H_2 and aqueous NaCl solutions for temperatures, pressures, and molalities of (298 to 523) K, (1 to 600) bar, and (0 to 6) mol NaCl/kg H_2O, respectively, (b) self-diffusivities of H_2 in aqueous NaCl solutions for temperatures, pressures, and molalities of (298 to 723) K, (1 to 1000) bar and (0 to 6) mol NaCl/kg H_2O, respectively, and (c) solubilities of H_2 in aqueous NaCl solutions for temperatures, pressures, and molalities of (298 to 363) K, (1 to 1000) bar and (0 to 6) mol NaCl/kg H_2O, respectively. The interfacial tensions and self-diffusivities are computed using MD simulations, and the solubilities are computed using CFCMC [116–118] simulations. Densities and viscosities of the aqueous NaCl solutions are also computed for a wide range of conditions and are compared to available experimental data. The TIP4P/2005 [107] force field is used for H_2O, the Madrid-2019 [119] force field for NaCl, and the Vrabec [102] and Marx [101] force fields are used for H_2. A modified version of the Madrid-2019 force field by Vega and co-workers [120] (i.e., the Madrid-Transport [115, 120]), optimized for viscosities of aqueous NaCl solutions for salinities up to the experimental solubility limit, is also used.

The paper is structured as follows. Details of the force fields used and the molecular

simulation techniques are given in section 4.2. In section 4.5, the computed interfacial tensions, viscosities, densities, self-diffusivities, and solubilities obtained are presented and compared with experimental data when possible. Finally, concluding remarks are presented in section 5.11. All data computed in this study are provided in a tabulated format in the Supporting Information of Ref. [47].

2.2 Methodology

2.2.1 Force Fields

The four-site TIP4P/2005 [107] force field is used to model H_2O. Previous studies have shown that this force field can accurately capture thermodynamic, transport, and interfacial properties of pure H_2O and H_2O/NaCl solutions in contact with gases for a wide range of conditions [85, 87, 98, 121–126]. For the Na^+ and Cl^- ions, the Madrid-2019 [119] force field is used, which is parameterized for the TIP4P/2005 H_2O model [127]. A new version of the Madrid-2019 force field (i.e., Madrid-Transport force field [115, 120]) is currently being developed by Vega and co-workers [120], which performs better for transport properties, especially at high NaCl molalities. The difference of Madrid-Tranport from Madrid-2019 is that ion charges are scaled by 0.75 instead of 0.85, and the Lennard-Jones (LJ) parameters are slightly altered. Interfacial tensions and self-diffusivities are computed using the single-site Vrabec [102] H_2 force field, while for the solubilities of H_2 in the aqueous NaCl solutions the three-site Marx [101] model is used. Tsimpanogiannis *et al.* [122] showed that the Vrabec [102] H_2 force field yields very accurate self-diffusivities of H_2 in pure TIP4P/2005 H_2O. The solubilities computed using the Vrabec [102] force field deviate from experimental data of H_2 in pure water by ca. 50%. In sharp contrast, the solubilities computed using the Marx [101] force field show excellent agreement with experimental data. A comparison of the solubilities computed using the Marx and Vrabec force fields in pure TIP4P/2005 H_2O are listed in Table S1 and shown in Figure S1 of the Supporting Information of Ref. [47]. At low temperatures, H_2 exhibits quantum effects which can be accounted for by using potentials such as the Feynman-Hibbs effective interaction potential [128–130]. At the temperatures considered in this work (i.e., 298 K and above) these quantum effects can be neglected [131]. All force field parameters are listed in Tables S2-S5 in the Supporting Information of Ref. [47]. A list of the chemical formulas, CAS numbers, and force fields of all species studied here is shown in Table 2.1.

Component	Chemical formula	CAS number	Force field
Water	H_2O	7732-18-5	TIP4P/2005 [107]
Hydrogen	H_2	133-74-0	Vrabec [102]
Hydrogen	H_2	133-74-0	Marx [101]
Sodium	Na^+	7440-23-5	Madrid-2019 [119]
Sodium	Na^+	7440-23-5	Madrid-Transport [115, 120]
Chloride	Cl^-	7782-50-5	Madrid-2019 [119]
Chloride	Cl^-	7782-50-5	Madrid-Transport [115, 120]

Table 2.1: Details of all the species simulated in this work.

2.2.2 Molecular Simulation Details

MD simulations

The MD simulations are used to calculate (a) the interfacial tensions of H_2 in contact with aqueous NaCl solutions, (b) self-diffusivities of H_2 in aqueous NaCl solutions, (c) densities, and (d) viscosities of aqueous NaCl solutions. For all MD simulations, the Large-scale Atomic/Molecular Massively Parallel Simulator (LAMMPS) [132] is used (version 29 Sep 2021). For the integration of the equations of motion, the velocity-Verlet algorithm is used with a time step of 1 fs. The bond length and bending angle of H_2O are fixed using the SHAKE algorithm [132, 133]. The intermolecular interactions are described by Lennard-Jones and Coulombic interaction potentials. The Lorentz-Berthelot combining rules [134] are used for interactions between different types of molecules, with the exception of $Na^+ - H_2O$, $Na^+ - Cl^-$, and $Cl^- - H_2O$ LJ interactions as specified in Table S5. Long-range electrostatic energies are computed using the particle-particle particle-mesh (PPPM) method [33, 135] with a relative error [136] of 10^{-5}. The temperature and pressure are regulated by the Nosé-Hoover thermostat and barostat [33]. Initial configurations are created using the PACKMOL software [137]. Periodic boundary conditions are imposed in all directions. All MD simulations for a specific set of conditions are repeated 5 times using different initial velocity distributions from which the average quantities are calculated. The reported uncertainties are standard deviations from the results of these 5 simulations.

Computation of interfacial tension

The following procedure is used for computing the interfacial tensions: An initial configuration is created by combining separately equilibrated bulk phases of aqueous sodium chloride solutions and H_2 gas. An equilibration run of 5 ns is carried out in the NPT ensemble using anisotropic pressure coupling, i.e., only the z-direction of the simulation box is allowed to fluctuate. The last 2 ns of the equilibration run are used to calculate the average simulation box dimensions, which are used for an equilibration run of 3 ns in the NVT ensemble. Next, production runs of 2 ns are carried out for computing the interfacial tension. In all simulations, 2088 H_2O molecules are used. Depending on the pressure, the number of H_2 molecules varied between 64 - 640. 0 - 188 Na^+ and Cl^- ions are used, depending on the molality. The exact numbers of species along with the simulation box sizes for all simulations are listed in Table S6 of the Supporting Information of Ref. [47]. A cutoff radius of 12 Å is used for the short-range LJ and short-range electrostatic energies. Because the system is inhomogeneous, analytic corrections were not used. Instead, Long-range LJ and electrostatic interactions are computed using the Particle-Particle Particle-Mesh (PPPM) method [33, 135, 138]. For the real and reciprocal space computations for the dispersion part of the PPPM method the desired accuracies are set to 0.0001 and 0.002, respectively. A relative error of 10^{-5} is used for the long-range electrostatic energies. The adequacy of the PPPM method for computing the LJ interactions has been recently validated by Salehi *et al.* [139] in interfacial MD simulations of deep eutectic solvents with water.

Figure 2.1 (top panel) shows a typical MD simulation snapshot at T = 343 K, P = 100 bar, and m = 3 mol NaCl/kg H_2O. The bulk liquid H_2O phase containing the Na^+ and Cl^- ions, which is shown as the transparent blue surface, occupies a domain of ca. 40 × 40 × 40 Å in the middle of the simulation box. H_2 gas is in contact with the liquid phase from both sides,

in the z-direction. This creates two H_2/H_2O interfaces perpendicular to the z-direction. The density profile of this system, averaged over 1 ns, is shown in Figure 2.1 bottom panel.

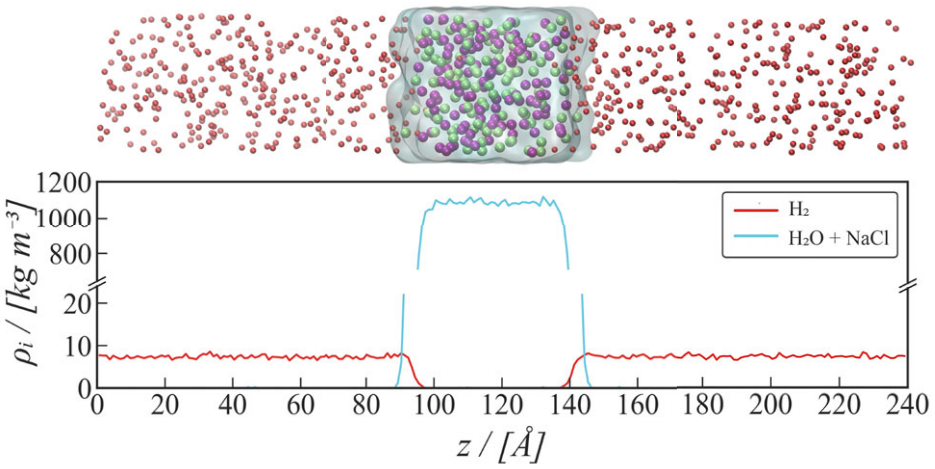

Figure 2.1: Top: Typical snapshot from a Molecular Dynamics simulation used to calculate the interfacial tension of H_2 and an aqueous NaCl solution (3 mol NaCl/kg H_2O) at 343 K and 100 bar. H_2 molecules are represented by red spheres, Na^+ and Cl^- are represented by purple and green spheres, respectively, H_2O is represented by the transparent blue surface. Bottom: Density profile in the z-direction of H_2 and the aqueous NaCl solution of the same simulation, averaged over 1 ns. z is the direction perpendicular to the interface.

The interfacial tension γ is calculated from the principal components of the diagonal elements of the stress tensor (P_{zz}, P_{xx}, and P_{yy}) [140]:

$$\gamma = \frac{1}{2} h_z \left[P_{zz} - \frac{1}{2} \left(P_{xx} + P_{yy} \right) \right], \tag{2.1}$$

where h_z is the simulation cell length in z-direction.

Computation of self-diffusivities and viscosities

The scheme used for computing self-diffusivities and viscosities follows from Ref. [141]. Initially, energy minimizion of the system is performed, followed by equilibration runs in the NPT and NVT ensembles for 1 – 2 ns. Next, production runs in the NVT ensemble for 10 ns are carried out. The system consists of 700 H_2O molecules, 2 H_2 molecules, and 0 – 76 Na^+ and Cl^- ions, depending on the molality. The exact numbers of species used for every state point are provided in Table S7 of the Supporting Information of Ref. [47]. A cutoff radius of 10 Å is used for Lennard-Jones and electrostatic interactions. Analytic tail corrections for energies and pressures are applied.

To compute the self-diffusivities and the shear viscosities, the OCTP plugin [141] in LAMMPS is used. In this plugin, the Einstein relations are used in combination with the order-n algorithm[33] as implemented by Dubbeldam *et al.* [142]. Self-diffusivity D_i of species i is computed based on the mean-squared displacements using:

$$D_i = \lim_{t\to\infty} \frac{1}{6N_i t} \left\langle \sum_{j=1}^{N_i} \left(\boldsymbol{r}_{j,i}(t) - \boldsymbol{r}_{j,i}(0) \right)^2 \right\rangle, \tag{2.2}$$

where $\boldsymbol{r}_{j,i(t)}$ is the position vector of the j-th molecule of species i at time t and N_i is the number of molecules of species i. All self-diffusivities in this work are corrected for finite-size effects using the Yeh-Hummer equation [143–145]:

$$D = D_i + \frac{k_B T \xi}{6\pi\eta L}, \tag{2.3}$$

where D is the finite-size corrected self-diffusivity, T is the temperature in K, ξ is a dimensionless constant equal to 2.837298, η is the shear viscosity from Equation 2.4, and L is the simulation box length. In this work, the finite-size correction magnitude was ca. 5 – 10 % of the computed self-diffusivities.

Shear viscosity η is computed from:

$$\eta = \lim_{t\to\infty} \frac{1}{10\cdot 2t} \frac{V}{k_\mathrm{B} T} \left\langle \sum_{\alpha\beta} \left(\int_0^t P_{\alpha\beta}^{\mathrm{os}}\left(t'\right) \mathrm{d}t' \right)^2 \right\rangle, \tag{2.4}$$

where

$$P_{\alpha\beta}^{\mathrm{os}} = \frac{P_{a\beta} + P_{\beta a}}{2} - \delta_{\alpha\beta} \left(\frac{1}{3} \sum_k P_{kk} \right), \tag{2.5}$$

where V is the volume of the system, k_B is the Boltzmann constant, $P_{\alpha\beta}^{\mathrm{os}}$ denotes the components of the traceless pressure tensor, $\delta_{\alpha\beta}$ is the Kronecker delta, and $\langle..\rangle$ indicates an ensemble average. The compution of η does not depend on the size of the system [146–148].

Computation of Solubilities

Continuous Fractional Component Monte Carlo [116–118] simulations in the isobaric-isothermal (CFCNPT) ensemble are used to compute solubilities and excess chemical potentials of H_2 in NaCl solutions. The open-source Brick-CFCMC software [116, 149, 150] is used for all simulations. A 10 Å cutoff radius is used for both the LJ and Coulombic interactions. The Ewald summation with a relative precision of 10^{-6} is used for the electrostatics. Analytic tail corrections for energies and pressures are applied [33]. The infinite dilution excess chemical potential of H_2 can be computed using a single "fractional" molecule of H_2. Fractional molecules have their interactions scaled with a continuous order parameter λ [116, 131]. In CFCNPT simulations, λ ranges from 0 to 1. $\lambda = 0$ indicates that the fractional molecule does not interact with the surrounding molecules/atoms (i.e., the fractional molecule behaves as an ideal gas molecule), and $\lambda = 1$ corresponds to full interactions. For the specifics regarding the scaling of the interactions the reader is referred elsewhere [151–153]. To improve the sampling in the λ-space, a biasing weight function ($W(\lambda)$) is created using the Wang-Landau algorithm [154, 155]. This biasing weight function is used to ensure a flat probability distribution in the λ-space ($p_{\mathrm{obs}}(\lambda)$). To compute the probability of occurrence of each λ value, a histogram with 100 bins is used. The Boltzmann averaged probability distributions of λ ($p(\lambda)$) can be computed using [115, 156]

$$p(\lambda) = \frac{\langle p_{\mathrm{obs}}(\lambda) \exp[-W(\lambda)] \rangle}{\langle \exp[-W(\lambda)] \rangle}. \tag{2.6}$$

The Boltzmann sampled probability distribution of λ ($p(\lambda)$) can be related to the infinite dilution chemical potential (μ^{ex}) using [115, 116, 156]

$$\mu^{ex} = -k_B T \ln \frac{p(\lambda = 1)}{p(\lambda = 0)}, \tag{2.7}$$

where $p(\lambda = 1)$ and $p(\lambda = 0)$ are the Boltzmann averaged probability distributions of λ at 1 and 0, respectively.

5×10^5 equilibration cycles, and 5×10^5 production cycles are performed for all simulations. A cycle contains N number of trial moves, with N being the total number of molecules, with a minimum of 20. The following probabilities are used for selecting the trial moves: 35% translations, 29% rotations, 1% volume changes, 25% λ changes, and 10% reinsertions of the fractional molecules at random locations inside the simulation box. The maximum displacements for molecule translations, volume changes, rotations, and λ changes are adjusted to obtain ca. 50% acceptance. Another method that can be used to compute μ^{ex} is the Widom's Test Particle Insertion method (WTPI) [33, 134, 157, 158]. In dense fluid phases WTPI yields inaccurate results compared to the CFCMC method as successful insertion of test particles is a highly unlikely event due to the significant potential energy increase in case of overlap with other particles [116, 159].

The solubilities of H_2 in aqueous NaCl solutions are computed at temperatures in the range (298 to 363) K and at H_2 partial pressures of 1, 10, 100, 400, and 1000 bar. At H_2 partial pressures of 1 bar and 10 bar, the H_2 solubilities are computed using Henry coefficients (H):

$$H = \lim_{f_i \to 0} \frac{f_i}{\langle \rho_{H_2,L} \rangle / \rho_0}, \tag{2.8}$$

where f_i is the fugacity of H_2 in the gas phase, $\langle \rho_{H_2,L} \rangle$ is the average number density of H_2 in the aqueous solution in units of $1/m^3$, and ρ_0 is a reference number density in the same unit as $\rho_{H_2,L}$ (set to 1 molecule per m^3)[156]. At H_2 partial pressures of 1 bar and 10 bar, the fugacity coefficient of H_2 is assumed to be 1 (i.e., the fugacity of H_2 is equal to the partial pressure of H_2). The validity of Eq. 2.8 at H_2 partial pressures of 1-100 bar is discussed in Figure S3 of the Supporting Information of Ref. [47]. From the MC simulations, H can be computed using [156]

$$H = \rho_0 k_B T \exp\left[\frac{\mu^{ex}_{H_2,L}}{k_B T}\right], \tag{2.9}$$

where $\mu^{ex}_{H_2,L}$ is the infinite dilution chemical potential of H_2 in the aqueous solution. A single fractional molecule of H_2, 300 H_2O molecules, and varying number of NaCl molecules depending on the molality (ranging from 0 to 6 mol NaCl/kg H_2O) are used to compute $\mu^{ex}_{H_2,L}$. The exact numbers of ions used for each molality are listed in Table S8 of the Supporting Information of Ref. [47]. To calculate solubilities of H_2 in aqueous NaCl solutions at pressures of 100, 400, and 1000 bar, the chemical potentials of H_2 in the liquid and in the gas phase are equated at constant pressure and temperature. The chemical potential of H_2 in the gas phase ($\mu_{H_2,G}$) is equal to [33]

$$\mu_{H_2,G} = \mu^0_{H_2} + k_B T \ln\left(\frac{\langle \rho_{H_2,G} \rangle}{\rho_0}\right) + \mu^{ex}_{H_2,G}, \tag{2.10}$$

where $\mu^0_{H_2}$ is the reference state of the chemical potential, $\langle \rho_{H_2,G} \rangle$ is the average number density of H_2 in the gas phase in units of $1/m^3$, and $\mu^{ex}_{H_2,G}$ is the excess chemical potential of H_2 in the gas phase. At pressures above 100 bar and at temperatures between (298 to 363) K, the gas phase contains very few H_2O molecules (a H_2O mole fraction below 0.01)[131]. $\mu^{ex}_{H_2,G}$ is calculated in separate CFCNPT simulations, containing a single fractional molecule of H_2, and 300 H_2 molecules in the gas phase. At conditions where the gas phase is non-ideal and the H_2O content in the gas phase is not negligible (i.e., temperatures above 363 K and pressures above 100 bar), Gibbs ensemble simulations can be performed to simulate the gas and the liquid phase simultaneously [131]. These simulations are beyond the scope of this work. The chemical potential of H_2 in the liquid phase ($\mu_{H_2,L}$) is equal to [33]

$$\mu_{H_2,L} = \mu^0_{H_2} + k_B T \ln\left(\frac{\langle \rho_{H_2,L} \rangle}{\rho_0}\right) + \mu^{ex}_{H_2,L}. \tag{2.11}$$

$\langle \rho_{H_2,L} \rangle$ can be computed by equating Eq. 2.10 and Eq. 2.11. The mole fractions of H_2 (x_{H_2}) in aqueous NaCl solutions are computed using

$$x_{H_2} = \frac{\langle \rho_{H_2,L} \rangle \langle V \rangle}{N_{H_2O} + N_{NaCl} + \langle \rho_{H_2,L} \rangle \langle V \rangle}, \tag{2.12}$$

where $\langle V \rangle$ is the average volume of the simulation box, computed in the CFCNPT ensemble. N_{H_2O} and N_{NaCl} are the numbers of H_2O and NaCl molecules in the simulation box, respectively. For each condition (concentration, temperature, and pressure), 20 independent simulations are performed. These 20 simulations are divided into 5 blocks from which the Boltzmann sampled probability distribution of λ ($p(\lambda)$) are averaged. The averaged distributions ($p(\lambda)$) of all blocks are used to compute mean values and standard deviations for the excess chemical potentials and solubilities of H_2.

2.3 Results and Discussion

2.3.1 Interfacial tensions

Figure 2.2 shows the computed interfacial tensions of H_2/H_2O/NaCl as a function of pressure (Figure 2.2a), molality (Figure 2.2b) at temperatures in the range of (298 to 523) K, and as a function of temperature (Figure 2.2c) for molalities in the range of (0 to 6) mol NaCl/kg H_2O. Tabulated raw data of the interfacial tension along with their statistical uncertainties are listed in Table S9 of the Supporting Information of Ref. [47]. Figure 2.2a and 2.2c also show the available experimental data from Hosseini *et al.* [66]. For the whole range of conditions a close agreement with the experimental results is found. The MD results differ on average 6.4 % from the experimental values. The simulations at 523 K cannot be directly validated due to lack of experimental data.

The interfacial tensions computed in this work are fitted to an engineering equation:

$$\gamma = c_1 + c_2 m + c_3 T^{c_4}, \tag{2.13}$$

where c_1, c_2, c_3 and c_4 are fitting parameters, which are listed in Table 2.2. Eq. 2.13 is valid for temperatures, pressures, and molalities of (298 to 523) K, (1 to 600) bar, and (0 to 6) mol

NaCl/kg H_2O, respectively. The results of this engineering equation are shown as solid lines in Figure 2.2. Eq. 2.13 is a very good fit to MD results, and can be used for calculating values at a specific combination of conditions in a fast and reliable way.

c_1 / [mN/m]	89.6
c_2 / [(mN·kg_{H_2O})/(m·mol_{NaCl})]	1.44
c_3 / [mN/(m·$K^{1.65}$)]	-2.04 ×10^{-3}
c_4 / [-]	1.65

Table 2.2: Parameters of Eq. 2.13 for predicting interfacial tension of H_2 in contact with aqueous NaCl solutions obtained using the NaCl Madrid-2019 [119] force fields, TIP4P/2005 [107] H_2O force field and Vrabec [102] H_2 force field. These parameters are valid for NaCl molalities of (0 to 6) mol NaCl/kg H_2O, temperatures of (298 to 523) K, and pressures of (1 to 600) bar.

As shown in Figure 2.2a, no significant pressure dependence of interfacial tension is observed. The data of experimental studies also show no significant or small pressure dependence [35, 61, 64, 66]. In particular, Higgs *et al.* [35] did not observe a significant pressure dependence for H_2 in contact with aqueous NaCl solutions. Other studies observed a small decrease in interfacial tension of H_2 and pure H_2O [61, 64, 66] and H_2 and aqueous (NaCl+KCl) solutions[66]. Interestingly, the pressure dependence of H_2/H_2O interfacial tension is small compared to the CO_2/H_2O [160–162] and CH_4/H_2O [89, 163, 164] systems. This is because the interfacial tension is related to the density difference between the two phases [55]. The change in density difference between H_2 and H_2O is very small at varying pressures because the density of H_2 is very low in comparison to H_2O, and H_2O is almost incompressible at these pressures.

As shown in Figure 2.2b, the interfacial tension increases linearly with solution molalities, in agreement with the available experimental data [66]. This behavior is also observed for other gases such as CO_2 and CH_4 [165–167]. This increase is mainly due to the increased density of saline H_2O compared to pure H_2O as well as the arrangement of cations and anions at the interface [166, 168–172]. The hydrogen bond network of H_2O is strengthened by cations [169–171], while anions cause the opposite effect [169–171]. Therefore, cations are absorbed into the bulk phase while anions are depleted from the bulk phase. This phenomenon can be observed in Figure S2 of the Supporting Information of Ref. [47], where it is shown that the number density of Cl^- ions at the interface is higher than Na^+ ions, and Na^+ ions are drawn into the bulk phase. The strengthening of the hydrogen bond network of H_2O leads to an increase in interfacial tension [166, 168].

In Figure 2.2c, a non-linear decrease of interfacial tension with temperature can be observed. This is in line with the experimental data of Chow *et al.* [64]. In sharp contrast, Hosseini *et al.* [66] reported a linear decrease of interfacial tension with temperature. The fact that interfacial tension depends non-linearly on the density difference between the two phases in contact [55] combined with the non-linear effect of temperature on the density difference between H_2 and H_2O, results in the expectation that the interfacial tension is also non-linearly related to temperature. Therefore, the observed non-linear relationship between interfacial tension and temperature in our results is expected.

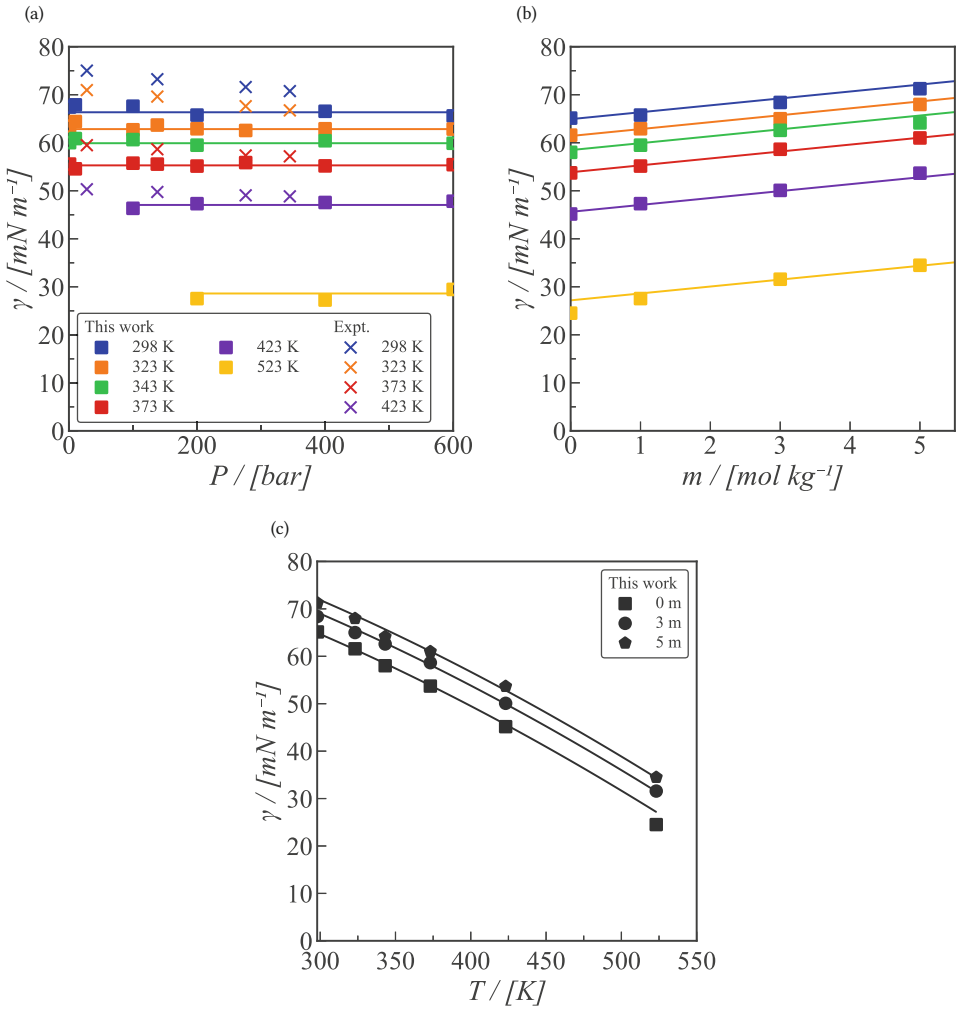

Figure 2.2: MD results of interfacial tension γ of H_2 and aqueous NaCl solutions using the NaCl Madrid-2019 [119] force fields, the TIP4P/2005 [107] H_2O force field, and the Vrabec [102] H_2 force field (a) as functions of pressure P for temperatures in a range of (298 to 523) K with a molality m of 1 mol NaCl/kg H_2O in combination with the experimental results of Hosseini *et al.* [66], (b) as functions of molality at a pressure of 200 bar of the solution for similar temperatures, and (c) as functions of temperature at a pressure of 200 bar and molalities of (0 to 6) mol NaCl/kg H_2O. The statistical uncertainties are comparable to or smaller than the symbols and can be found in Table S9 of the Supporting Information of Ref. [47]. The error bars have been omitted for clarity. The solid lines represent fits using Eq. 2.13 for temperatures in the range of (298 to 523) K.

2.3.2 Viscosities and Densities

Figure A.1 shows the computed densities and viscosities of aqueous NaCl solutions as functions of NaCl molalities at 298 and 343 K. The densities are computed from the average volume calculated from the *NPT* ensemble. Eq. 2.4 is used to compute the viscosities. Densities and viscosities of aqueous NaCl solutions have a weaker dependence on pressure (in the range of 0 – 1000 bar) compared to temperature and NaCl molalities. Figure S4 and S5 in the Supporting Information of Ref. [47] show the densities, and viscosities as functions of pressure. The results for the Madrid-2019 [119] and the Madrid-Transport [115, 120] NaCl force fields are shown in Figure A.1. Laliberté [173] and Laliberté and Cooper [174] developed models on the basis of experimental data for viscosities and densities, respectively. These fits are shown in Figure A.1. The raw data of these properties, as well as their statistical uncertainties, are listed in Table S10 of the Supporting Information of Ref. [47]. Both the Madrid-2019 [119] and Madrid-Transport [115, 120] capture the experimental data of density very accurately (within 1%). As shown in Figure 2.3a, the Madrid-Transport [115, 120] force field yields a better agreement with the experimental data of viscosity compared to the Madrid-2019 [119] force field. The discrepancy between the two force fields starts at molalities above 2 mol NaCl/kg H_2O. The viscosities computed using the Madrid-2019 force field deviate on average ca. 20 % from the experimental data, while this deviation is is only ca. 3% when the Madrid-Transport force field is used. Based on the excellent performance of Madrid-Transport in reproducing experimental viscosities, which is necessary for reliable diffusivity predictions [175], only this force field was used for computing the self-diffusivities of H_2 in NaCl solutions.

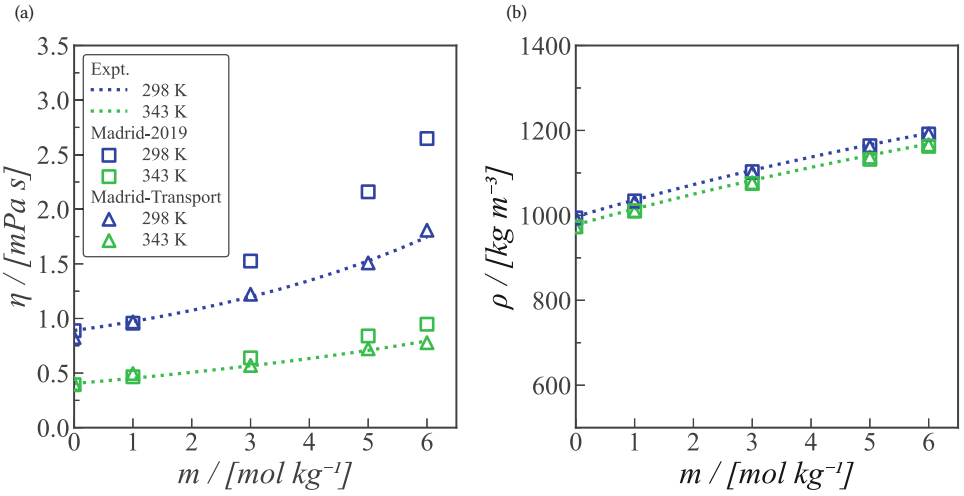

Figure 2.3: Computed (a) viscosities η and (b) densities ρ of aqueous NaCl solutions as a function of molality m (mol NaCl/kg H_2O) at a pressure of 1 bar and temperatures of 298 and 343 K. The fit to the experimental data is created by (a) Laliberté [173] and (b) Laliberté and Cooper [174]. The statistical uncertainties can be found in Table S10 of the Supporting Information of Ref. [47]. The error bars are smaller or comparable to the symbol size and have been omitted for clarity.

2.3.3 Self-diffusivities of H_2

Figure 2.4 shows the computed finite-size corrected self-diffusivities of H_2 in aqueous NaCl solutions as a function of (a) pressure, (b) NaCl molality, and (c) temperature. These simulation are performed with the Madrid-Transport [115, 120] force field for NaCl, the TIP4P/2005 [107] H_2O, and the Vrabec [102] force field for H_2. All the self-diffusivities of H_2 computed in this work are listed in Tables S11 and S12 of the Supporting Information of Ref. [47]. Simulations using the Madrid-2019 [119] NaCl force field are performed for comparison. These data are shown in Table S12 of the Supporting Information of Ref. [47].

The self-diffusivities of H_2 shown in Figure 2.4 are fitted to an engineering correlation:

$$D = c_1 \exp\left[c_2 m + c_3\left(\frac{1}{T}\right) + c_4 P\right], \tag{2.14}$$

where c_1, c_2, c_3, and c_4 are fitting parameters, which are listed in Table 2.3. As shown in Figure 2.4, this correlation provides an excellent fit for the MD results. Note that Eq. 2.14 is only valid for conditions at which H_2O is in the liquid phase, and therefore, data points at temperatures of 723 K or higher are excluded as the solution is in the supercritical phase. In this work, self-diffusivities for temperatures of 723 K and pressures lower than 400 bar are not calculated, because at those conditions, H_2O is in the gas phase. Eq. 2.14 is an empirical model.

c_1 / [m^2/s]	1.24×10^{-6}
c_2 / [$(mol_{NaCl}/kg_{H_2O})^{-1}$]	-7.29×10^{-2}
c_3 / [K]	-1.70×10^{3}
c_4 / [bar^{-1}]	-1.84×10^{-4}

Table 2.3: Parameters of Eq. 2.14 for predicting the computed finite-size corrected self-diffusivities D of H_2 in aqueous NaCl solutions obtained using the NaCl Madrid-Transport [115, 120] force fields, the TIP4P/2005 [107] H_2O force field, and the Vrabec [102] H_2 force field. These parameters are valid for NaCl molalities of (0 to 6) mol NaCl/ kg H_2O, temperatures of (298 to 523) K, and pressures of (1 to 1000) bar. Note that Eq. 2.14 should only be used at conditions in which water is in the liquid state.

In Figure 2.4a a weak pressure dependence of the self-diffusivities of H_2 is observed. The logarithm of the self-diffusivities decays linearly with respect to variations in pressure, similarly to what is reported by Tsimpanogiannis *et al.* [122]. The pressure dependence of the self-diffusivities of H_2 is more significant at 723 K (Figure 2.4a) as the solution is more compressible at these conditions. As shown in Figure 2.4b, the logarithm of the self-diffusivities is also found to decay linearly with respect to variation in the NaCl molalities. Laliberté [173] has shown that the viscosities of aqueous NaCl solutions increase exponentially with respect to NaCl molalities. As the self-diffusivities of gases dissolved in liquids are inversely proportional to the viscosities of the solution [55, 175], the self-diffusivities of H_2 are expected to decay exponentially with respect to the NaCl molalities. The computed self-diffusivities of H_2 follow an Arrhenius-type[33] relation with respect to variations in temperature ($D \propto \exp[\frac{c}{T}]$) as shown in Figure 2.4c. This behavior is also observed in literature for gases (e.g., O_2, H_2) dissolved in aqueous solvents [98, 124, 176–178].

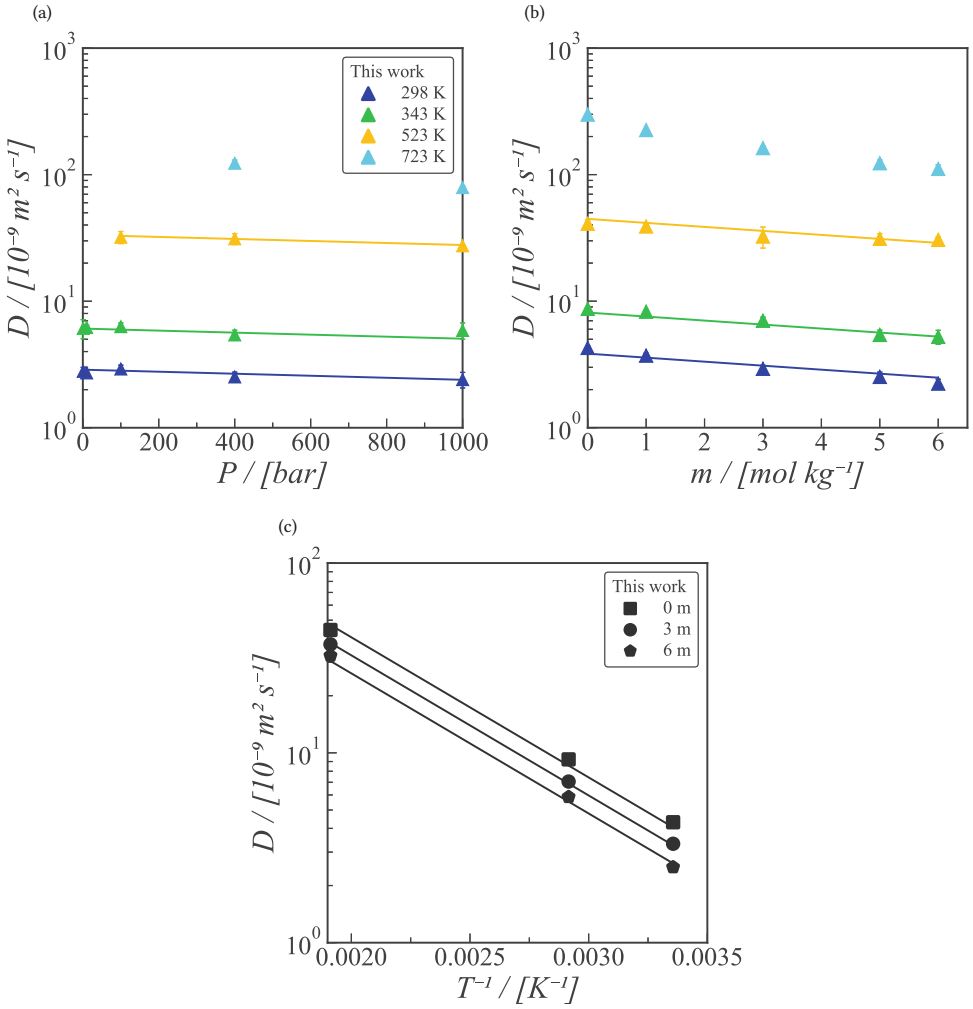

Figure 2.4: Computed finite-size corrected self-diffusivities (D) of H_2 in aqueous NaCl solutions (a) with a molality (m) of 5 mol NaCl/kg H_2O solution as a function of pressure P for temperatures of (298 to 723) K, (b) at a pressure of 400 bar as a function of m of the solution for the similar temperatures, and (c) as a function of the reciprocal temperature at a pressure of 100 bar. The results are obtained using the NaCl Madrid-Transport [115, 120] force fields, TIP4P/2005 [107] H_2O force field, and Vrabec [102] H_2 force field. The statistical uncertainties are comparable to or smaller than the symbols and can be found in Table S11 of the Supporting Information of Ref. [47]. The solid lines are fits calculated using Eq. 2.14 for temperatures of (298 to 523) K. Data points at a temperature of 723 K and a pressure of 400 bar are excluded from the fit because H_2O is supercritical at these conditions.

2.3.4 Solubilities

In Figure 2.5, the solubilities of H_2 computed using CFCMC are shown as a function of (a) NaCl molality, (b) temperature, and (c) pressure. The computed solubilities are compared to the experimental measurements of Chabab *et al.* [69], Torín-Ollarves and Trusler [70], and their corresponding experimental correlations (also shown in Figure 2.5). The correlation of Torín-Ollarves and Trusler [70] is based on the experimental measurements for NaCl molalities of 0 and 2.5 mol NaCl/kg H_2O, the experimental data by Wiebe and Gaddy [179], Wiebe *et al.* [180], Kling and Maurer [181], and Choudhary *et al.* [182] for H_2 solubility in pure H_2O, and the experiments by Crozier and Yamamoto [75] and Gordon *et al.* [76] for solubility of H_2 in saline solutions. Chabab *et al.* [69] provide an extensive experimental data set and a correlation for H_2 solubilities at temperatures of (323 to 373) K, and NaCl molalities in the range of (0 to 5) mol/kg H_2O. Lopez-Lazaro *et al.* [112] obtained the Henry constants of H_2 in aqueous NaCl solutions for molalities up to 2 mol NaCl/kg H_2O using excess chemical potentials computed using the WTPI method [33, 134, 157, 158]. Using the Henry constants reported by Lopez-Lazaro *et al.* [112], the solubilities of H_2 at a partial pressure of 100 bar are computed and shown in Figures 2.5a and 2.5b. The simulations of Lopez-Lazaro *et al.* [112] show large error bars (ca. 10-20%). This may be due to the use of the WTPI method [33, 134, 157, 158], which requires a large number of MC cycles to obtain low standard deviations for excess chemical potentials in the liquid phase [112, 116]. The solubilities computed in this work using CFCMC simulations [117, 118, 149, 150] have uncertainties of less than 5 %.

Figure 2.5a shows the decrease of the solubilities of H_2 at increasing molalities of NaCl (i.e., salting-out effect). The salting-out of non-polar gases (e.g., H_2, O_2, and CO_2) in presence of salts such as NaCl, KCl, and KOH is a well observed phenomenon [95, 115, 172]. As shown in Figure 2.5a, the models by Torín-Ollarves and Trusler [70] and Chabab et al. [69] agree for H_2 solubilities in pure H_2O and at NaCl molalities below 0.5 mol NaCl/kg H_2O. For NaCl concentrations higher than 0.5 mol NaCl/kg H_2O the two models predict different H_2 solubilities. The salting-out effect of H_2 observed in this work using the Madrid-2019 [119] Na^+ and Cl^-, TIP4P/2005 [107] H_2O, and the Marx [101] H_2 force fields show better agreement to the salting-out effect observed by Torín-Ollarves and Trusler [70] as shown in Figure 2.5a. The correlation of Torín-Ollarves and Trusler [70] also shows agreement with our simulations at H_2 partial pressures ranging from (1 to 400) bar in the temperature range (298 to 363) K, as shown in Figures 2.5b and 2.5c. Our simulation results also agree with the MC simulations by Lopez-Lazaro *et al.* [112] both for different NaCl molalities, and for different temperatures in the range of (298 to 523) K, even though the choice of the force fields for Na^+, Cl^-, and H_2 is different. Lopez-Lazaro *et al.* [112] have used the OPLS force field [183] for Na^+, and Cl^-, combined with the model by Darkim et al. [184] for H_2.

In Table S13 of the Supporting Information of Ref. [47], we provide an extensive database for solubilities of H_2 at temperatures of (298 to 363) K, H_2 partial pressures of (1 to 1000) bar, and at NaCl molalities of (0 to 6) mol/kg H_2O. The solubilities of H_2 at partial pressures up to 100 bar are computed for a wider temperature range i.e., (298 to 523) K. These data can be further used to test and train existing machine-learning models [71] or equations of state [185] for predicting H_2 solubilities in saline solutions at conditions relevant to geological H_2 storage.

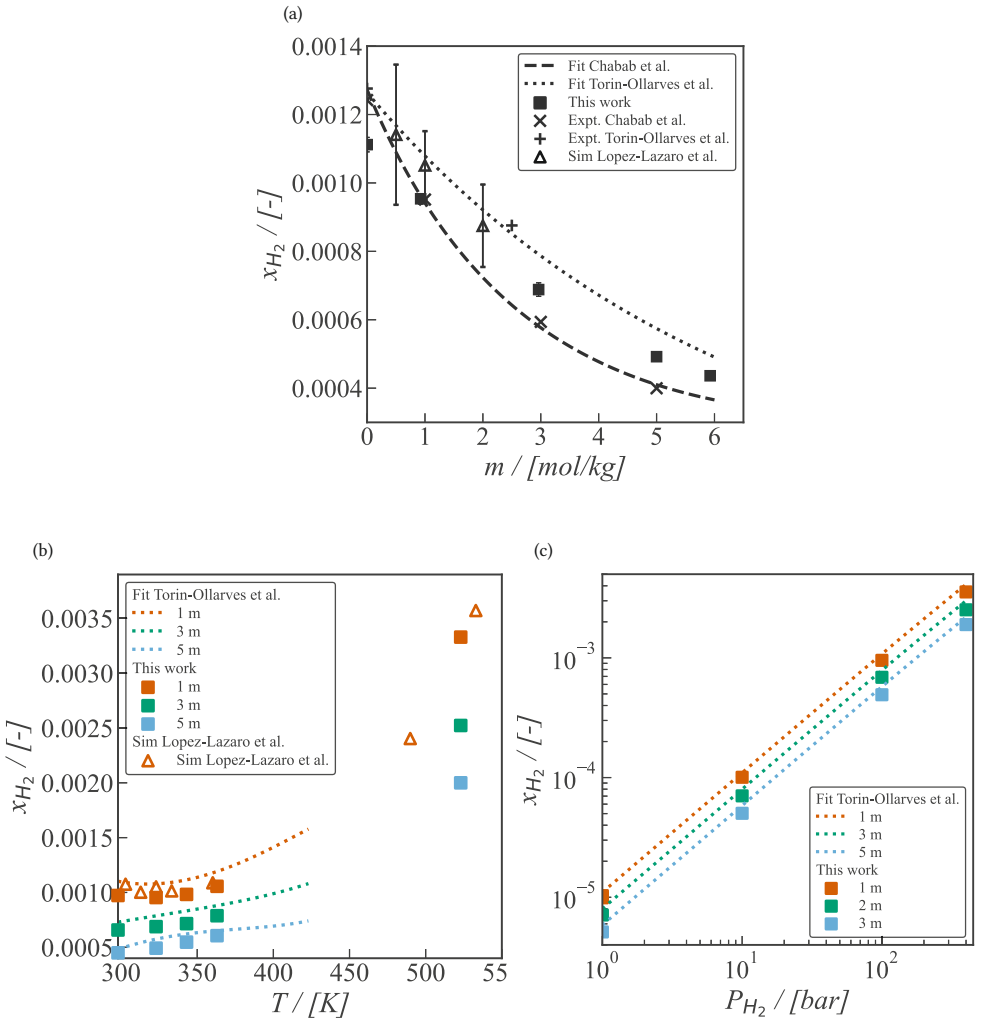

Figure 2.5: Computed solubilities of H_2 in aqueous NaCl solutions using the NaCl Madrid-2019 force field [119], TIP4P/2005 [107] H_2O force field, and Marx [101] H_2 force field as functions of (a) NaCl molality (m) in units of mol NaCl/kg H_2O for a H_2 partial pressure of 100 bar, at 323 K, (b) temperature for a H_2 partial pressure of 100 bar, and (c) H_2 partial pressure at 323 K. The dashed lines represent the experimental correlation provided by Torín-Ollarves and Trusler [70], and the dotted lines represent the experimental correlation results of Chabab et al. [69] The experimental data of Chabab et al. [69], and Torín-Ollarves and Trusler [70], and the simulation results of Lopez-Lazaro *et al.* [112] (converted from Henry constants) are also shown. The error bars of the simulations of this work are comparable (Figure 2.5a) or smaller than (Figure 2.5b and 2.5c) the symbol size.

2.4 Conclusions

Molecular simulations are used to compute (a) interfacial tensions of H_2 and aqueous NaCl solutions for temperatures, pressures, and molalities of (298 to 523) K, (1 to 600) bar, and (0 to 6) mol NaCl/kg H_2O, respectively, (b) self-diffusivities of H_2 in aqueous NaCl solutions for temperatures, pressures, and molalities of (298 to 723) K, (1 to 1000) bar and (0 to 6) mol NaCl/kg H_2O, respectively, and (c) solubilities of H_2 in aqueous NaCl solutions for temperatures, pressures, and molalities of (298 to 363) K, (1 to 1000) bar and (0 to 6) mol NaCl/kg H_2O, respectively. The simulations for computing H_2 self-diffusivities are also used to yield predictions for densities and viscosities of the NaCl solutions. The interfacial tensions and self-diffusivities are computed using MD simulations, and the solubilities are computed using CFCMC simulations. The H_2O TIP4P/2005 [107] force field, the NaCl Madrid-2019 [119] force fields, and H_2 Vrabec [102] and Marx [101] force fields are used. In addition, a modified version of the Madrid-2019 force field (i.e., the Madrid-Transport [115, 120] force field) is used, which is optimized for transport properties of aqueous solutions. Our results are validated against the available experimental data, models, and simulations. Excellent agreement between the results and experimental data is found with deviations smaller than 10% for the vast majority of the data points. The results of the NaCl Madrid-Transport force field were in better agreement with experimental data for transport properties, while the Madrid-2019 force field was sufficiently accurate for interfacial tensions and solubilities. The new data are used to develop engineering equations for interfacial tension and self-diffusion capturing the effect of pressure, temperature, and solution molality.

II

Hydrodynamics

3

Microfluidic experiments: Dynamic contact angle measurement

Underground Hydrogen Storage (UHS) is an attractive technology for large-scale (TWh) renewable energy storage. To ensure the safety and efficiency of the UHS, it is crucial to quantify the H_2 interactions with the reservoir fluids and rocks across scales, including the micro scale. This paper reports the experimental measurements of advancing and receding contact angles for different channel widths for a H_2/water system at P = 10 bar and T = 20 °C using a microfluidic chip. To analyse the characteristics of the H_2 flow in straight pore throats, the network is designed such that it holds several straight channels. More specifically, the width of the microchannels range between 50 µm and 130 µm. For the drainage experiments, H_2 is injected into a fully water saturated system, while for the imbibition tests, water is injected into a fully H_2-saturated system. For both scenarios, high-resolution images are captured starting the introduction of the new phase into the system, allowing for fully-dynamic transport analyses. For better insights, N_2/water and CO_2/water flows were also analysed and compared with H_2/water. Results indicate strong water-wet conditions with H_2/water advancing and receding contact angles of, respectively, $13^\circ - 39^\circ$, and $6^\circ - 23^\circ$. It was found that the contact angles decrease with increasing channel widths. The receding contact angle measured in the 50 µm channel agrees well with the results presented in the literature by conducting a core-flood test for a sandstone rock. Furthermore, the N_2/water and CO_2/water systems showed similar characteristics as the H_2/water system. In addition to the important characterisation of the dynamic wettability, the results are also crucially important for accurate construction of pore-scale simulators.

This chapter was published in Advances in Water Resources **Vol. 164**, (2022) [186].

3.1 Introduction

The contribution of renewable energy, especially wind and solar, in the future global energy mix is expected to increase significantly [187]. The intermittent nature of these energy resources makes the development of large-scale (TWh) energy storage facilities an essential component of future green energy systems [11]. Hydrogen (H_2) is considered an attractive energy carrier because of its high energy content per mass, and its clean combustion products. However, because of its low density, being the tiniest molecule, surface-based storage facilities do not offer the volumes required for large-scale (TWh) energy storage. Geological formations, such as depleted oil and gas reservoirs, aquifers and salt caverns have proven to provide safe storage options for gasses such as methane and carbon dioxide, and could also offer potential solutions for hydrogen storage [9, 11, 12, 188].

The feasibility of underground hydrogen storage in porous reservoirs highly depends on the flow and transport behaviour of hydrogen during subsequent injection and withdrawal cycles in the reservoir, which is governed by complex pore-scale processes [11, 48, 51, 189–191]. A common approach to investigate the impact of pore-scale processes on continuum-scale behaviour, as well as to derive meaningful continuum-scale transport parameters such as relative permeability and capillary pressure, is pore-network modelling [192–197]. In pore-network modelling the relevant physics at the pore-scale (e.g., contact angles and interfacial tension) is explicitly taken into account. However, for pore-network models to be successful, representative models of the pore-structure of the porous medium are required, as well as accurate descriptions of the wettability of the system [198–200]. The wettability can be then characterized by the contact angle between the H_2/brine/rock interfaces (Section 3.2.1, Figure 3.1) [45, 189, 201]. The contact angle is a function of, among other factors, pore size and pore geometry [202–204]. Furthermore, the contact angle can potentially be different during drainage and imbibition cycles, even in tube-like channels, used in pore-network systems. This phenomena is known as the contact angle hysteresis. Contact angle hysteresis is the result of the pore-structure heterogeneity, chemical interactions between the fluid and solid rock surface, as well as surface roughness [202, 205, 206]. Contact angle hysteresis has a direct impact on the amount of residual and capillary-trapped non-wetting phase [207], in this case H_2, and the economic feasibility of UHS, as the trapped H_2 cannot be produced from the reservoir.

Contact angles can be directly measured experimentally using the Captive bubble method [189, 208], Sessile drop method [209–211], Capillary tubes [212–215], Tilted plate method [216], Wilhelmy plate method [217], Microfluidic chips [215, 218], and In-situ μCT measurements [35, 36, 211, 219], of which μCT measurements of the contact angles are most representative of local pore geometries.

Morrow [220] studied the dependence of the advancing and receding contact angles on intrinsic contact angles. The intrinsic contact angles were measured on a smooth PTFE surface, for different fluid pairs. However, importantly to note, the corresponding advancing and receding contact angles were measured in roughened PTFE tubes. Under these conditions, Morrow [220] showed a systematic dependency of the advancing and receding contact angles on the intrinsic contact angle. Note that on smooth surfaces no hysteresis was expected to be observed. As such, the advancing and receding contact angles for

smoothed surfaces were assumed to be equal to the intrinsic contact angle. It is, therefore, expected that in the relatively new pore-scale simulation studies, Morrow's curves have been modified to obtain meaningful simulations [9]. In general, there are only limited experimental data sets available for H_2/water contact angles in porous reservoirs. Moreover, no direct measurements to quantify the effect of pore size/channel width on this parameter have been reported. Furthermore, no direct measurement of H_2 dynamic contact angles in tube-like micro channels have been done. The analyses of hydrogen transport properties in tube-like channels sheds new lights on meaningful design of pore-scale network simulation frameworks.

Relevant to UHS, in the literature, some experimental studies to characterize hydrogen transport properties have been conducted. Yekta *et al.* [221] performed core-flooding tests, in which hydrogen was injected into a water-saturated Vosges sandstone rock, to derive drainage relative permeability and capillary pressure curves. The experiments were carried out to represent shallow (50 bar – 20 °C) and deep (100 bar – 45 °C) aquifers. By combining the capillary pressure results with mercury injection capillary pressure (MICP) measurements and using the Young-Laplace scaling, they found the receding contact angles of 21.6° and 34.9° for the first and second conditions, respectively. Iglauer *et al.* [222] used the tilted plate experimental technique to determine advancing and receding contact angles for the H_2/brine/quartz system. The experiments were performed for a pressure range of 50 – 250 bar, and a temperature range of 23 – 70 °C. A brine with a salinity of 100,000 ppm NaCl was used. They found that increasing pressure, temperature, and organic surface concentration increased the hydrogen wettability, with contact angles ranging between 0° to maximum 50°. Hashemi *et al.* [189, 223] performed direct static contact angle measurements for H_2/brine/sandstone rock using a captive-bubble cell device. No correlations between the static contact angle and the pressure (20 – 100 bar), temperature (20 – 50 °C) and salinity (0 – 50 000 ppm NaCl) of the brine were found. Intrinsic contact angles between 25° (min) to 45°(max) were found for a variety of tests. Most recently, Higgs *et al.* [35] determined wettability of H_2/brine/quartz systems, using captive bubble, pendant drop and in-situ 3D micro-CT methods. They found contact angles of 29° – 39° at pressures of 69 – 210 bar and salinities of 0 – 5000 ppm NaCl. Consistent with the earlier findings [189], in their results, no conclusive impact of salinity or pressure was observed on the contact angle. Although, water-wet conditions were commonly found in all the past experiments, a wide variation in the currently reported H_2/brine contact angle data exists. This could possibly be explained by differences in the measurement techniques, where pore size/channel width could play a defining factor.

In order to provide valuable and missing wettability information for pore-network models, as well as to improve the scientific community's understanding of currently reported data on H_2-brine contact angles, in this work, we present a systematic study to measure H_2-brine contact angles for different channel widths in microfluidic systems for both drainage (receding) and imbibition (advancing) processes.

Experimental microfluidic investigations can provide insight in the dynamics of pore-scale processes [34, 224], and provide a bridge between the pore and the core scale [225].

Microfluidic experiments at early stages were based on simple micromodels, but later involved more complex network geometries [34]. The main limitations of most micromodels to represent actual subsurface systems, however, include their restriction to 2D networks, with a uniform etch depth in the third dimension, uniform surface chemistry and minimum channel width of 10 μm [226]. There are a few examples of micromodels which resemble actual 3D rock systems more closely [227, 228]. Micromodels have widely been used for experiments on the fundamentals of multiphase flow [229, 230], transport [231, 232] and wettability [218, 225, 226, 233–235]. Micromodels can, for example, be used to simulate drainage and imbibition processes and to study underlying processes like viscous or capillary fingering and snap-off [236–239]. The complex pore-geometries in real rocks make it difficult to systematically analyse the impact of factors such as pore size on the in-situ contact angle measurements [35, 36]. The advantage of using microfluidic chips is that the in-situ dynamic contact angles can be measured in simplified systems but with channel widths that are representative of porous media in the subsurface formations. However, to the best of the authors' knowledge, no study has been reported, in which micromodels are used to directly measure dynamic contact angles of H_2/brine systems.

The objective of this work is to characterize dynamic contact angles for different channel widths in a H_2/water/glass microfluidic system. In addition, the experiments will be carried out for CO_2 and N_2 to allow for the comparison with more commonly stored gasses in subsurface reservoirs. The results reported in this study can directly be used to take into account the impact of pore size/channel width on contact angle in pore-scale modelling approaches such as the one performed by Hashemi *et al.* [9], in order to find meaningful relative permeability and capillary pressure curves. Furthermore, this work can be used to improve our understanding of the wide variation in the limited H_2/brine contact angle data that is currently reported. The remainder of the paper is structured as follows. First, the experimental setup and procedure will be described, followed by the method of image analysis. Then, the results and their relevance for UHS will be provided and discussed. Finally, concluding remarks will be presented.

3.2 Materials and Methods

In this study, microfluidic chips are utilized to measure dynamic contact angles of gas-solid-liquid interfaces for the H_2/water, N_2/water, and CO_2/water systems. The experimental test groups and conditions are summarized in Table 3.1.

Test Group	Gas	Liquid	Rate [μl/min]	Temperature [°C]	Pressure [bar]
A	H_2	Pure Water	0.1	20	10
B	N_2	Pure Water	0.1	20	10
C	CO_2	Saturated Water	0.1	20	10

Table 3.1: Summary of the test groups and experimental conditions.

3.2.1 Theory

The wettability is a measure of the ability of a fluid to interact with a solid surface in combination with another fluid, and can be represented by the contact angle. The contact

angle is defined as the angle that a two-fluid interface makes with the solid surface. A contact angle bigger than 90° defines the non-wetting phase, while a contact angle smaller than 90° defines the wetting phase [45, 201]. In cases where the interface is not moving, the contact angle is static (SCA). Dynamic contact angles can be measured during drainage, where the non-wetting phase is displacing the wetting phase, corresponding to the injection of hydrogen in the reservoir. The contact angles measured during drainage are receding contact angles (RCA). When the process is reversed and hydrogen is withdrawn from the reservoir, the wetting phase is displacing the non-wetting phase, which is called imbibition. The contact angles measured during imbibition are advancing contact angles (ACA). An illustration is provided in Figure 3.1. Hysteresis is defined as the difference in contact angle during the drainage and imbibition phase of the process [240]. When the surface is smooth and the fluids are at rest and free of polar impurities, the static contact angle is a fundamental property of the system and is called the intrinsic contact angle (ICA) [220].

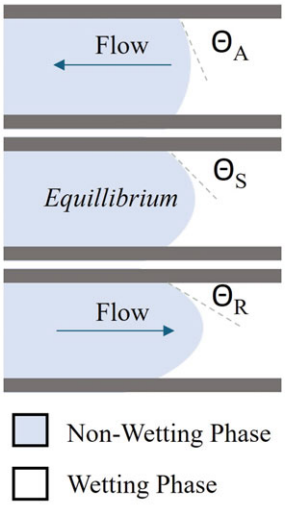

Figure 3.1: Schematic showing interface between phases. Contact angles: advancing θ_A, receding θ_R, static θ_S.

3.2.2 Materials

The microfluidic device used in the experiments consisted of a microchip (10 × 20 mm) supplied by Micronit Company. The material of the chip is borosilicate glass, with a pattern of a random square network. The channels have widths of 50, 70, 90, 110 and 130 µm measured in the widest part of the channel (see Figure 3.2). The width of the smallest channel is in the range of the most common pore sizes measured in Berea and Bentheimer sandstones [189, 241]. The depth of the channels is 20 µm. The shape of the channels is near-rectangular, with edged sides at the bottom. The permeability of the chip is 1.6 D, which is comparable with the permeability found for Bentheimer sandstone [242]. An overview of the chip can be found in Figure 3.2. H_2, N_2 and CO_2 gas with respective purity of 99.99%, 99.7% and 99.7% were used. Degassed deionized water was used during the experiments. For the CO_2 experiments the water was pre-saturated with CO_2, because

of the high solubility of CO_2 in water. H_2 and N_2 solubility in water is very low, with no expected impact on the contact angle [223]. Therefore, the water used in these experiments was not pre-equilibrated.

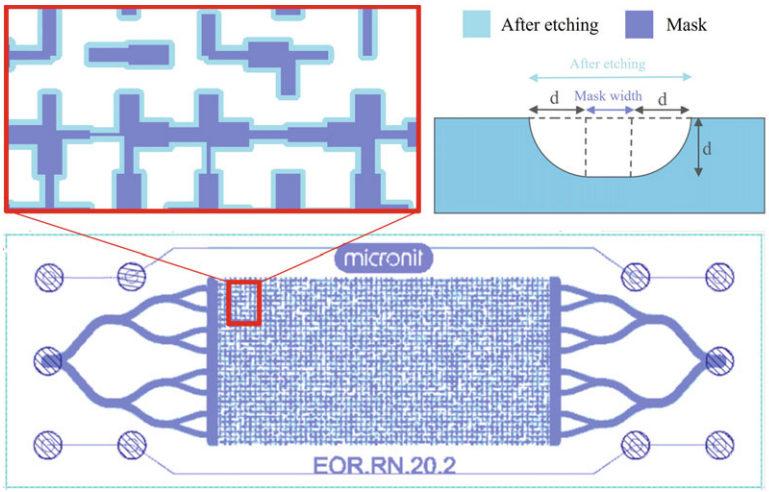

Figure 3.2: Schematic drawing of the borosilicate glass chip (based on the drawing on the website of Micronit Company). The chip is 10 mm × 20 mm. The channels have widths of 50, 70, 90, 110 and 130 µm and the depth of the channels is 20 µm.

3.2.3 Experimental apparatus

Figure 3.3 provides a schematic overview of the microfluidic apparatus. The microscope is a Leica DMi8 DFC7000 and was used in combination with a lens with a magnifying factor of 10. Videos of the experiments were taken with a Leica DFC7000T camera with LAS software. The frame rate of the videos was approximately 5 frames per second. The resolution of the videos was 1920 × 1440 pixels, with a pixel size of 0.75 × 0.75 µm. To prevent the chip from being contaminated, multiple filters were incorporated in the apparatus. The injected water (and ethanol) was filtered with a 0.2 µm VICI filter. In addition, there were two extra 0.5 µm filters (VICI Jour PEEK-encased frits) installed in the liquid and the gas lines. Two pumps were included in the setup, a quizix QX6000 pump and a PHD Ultra™ 4400 Programmable Syringe Pump - Harvard Apparatus with a 250 µL syringe. The Quizix pump was used to refill the highly accurate syringe pump, which can deliver flow rates as small as a few nanolitres per minute. The syringe pump was used for the injection into, and the withdrawal from, the microchip. The valves installed (Swagelok) were all 1/16" in size. Also, the tubes with 0.25 mm inner diameter (ID) with FEP transparent material were used to connect the pumps to the chip. The gas cylinder served to maintain the pressure. The pressure was monitored by the Quizix Pump. The experimental setup was limited to a pressure of 10 bar.

Safety aspects are crucially important when working with H_2. Therefore, in this study, the small volume of H_2 needed for the experiments was obtained from the gas regulator so that the gas cylinders could be closed during experiments. The volume of the regulator is

approximately 99 mL, which is large enough to carry out several experiments, but small enough to pose limited safety risks in a well-ventilated lab.
The setup was calibrated against the existing literature data of Jafari and Jung [218], in which the same chip was used to measure dynamic contact angles for the CO_2/water system. An important difference between the experimental apparatus of Jafari and Jung [218] and the one used in this study is the presence of several filters. The filters keep the system clean and avoid any impact of impurities on the contact angle measurements. More details about the validation tests and the impact of impurities on contact angle measurements can be found in A.1 and A.2.

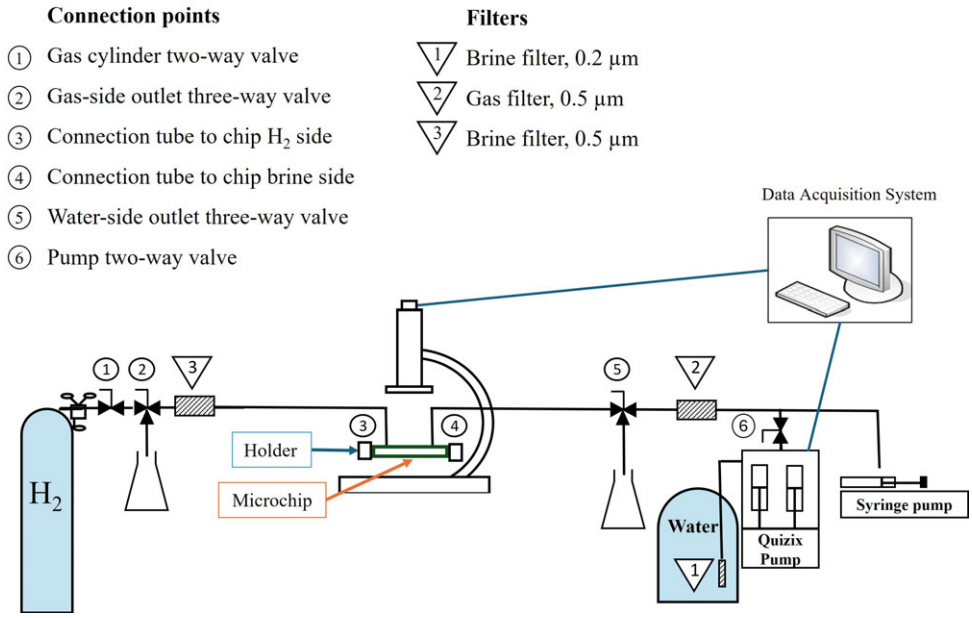

Figure 3.3: Schematic drawing of the experimental apparatus used to measure dynamic contact angles in microfluidic chips.

3.2.4 Experimental procedure

In this study, drainage and imbibition experiments are carried out as separate experiments. The objective is to measure dynamic contact angles as a function of channel width for these two different displacement processes. During the experiments, videos were taken to capture the moving gas-water interfaces within the channels. The drainage and imbibition tests were repeated until a sufficient amount of measurements for each channel width could be derived from the videos. A flow rate of 0.1 µl/min has been used during all experiments. This corresponds to an interstitial velocity (V) of $\approx 10^{-4}$ m/s. A capillary number ($Ca = \mu V/\sigma$) of $\approx 10^{-8}$ was calculated using an interfacial tension (σ) of 72.9 mN/m [243] and a dynamic viscosity (μ) of 9 µPa·s [244], which indicates a capillary-dominated flow regime.

Cleaning procedure

Prior to each experiment, the microchips were thoroughly cleaned. The cleaning procedure involved rinsing the chips with 5 mL of filtered ethanol, followed by flushing with filtered N_2 until no liquid was visible in the chip. The cleaning procedure was carried out at ambient pressure. To remove the N_2 from the clean chip, the system was flushed with the gas used in the experiment, followed by thoroughly rinsing with deionized water.

Drainage experiments

Before the start of the drainage experiments, the chips were saturated with deionized water at ambient pressure, after which the system was pressurized to the experimental pressure of 10 bar. However, for the experiments where the deionized water was pre-equilibrated with CO_2 (see Table 3.1), the system was saturated at the experimental pressure of 10 bar to avoid exolution of dissolved CO_2 from the water. For these experiments, back-pressure regulators were installed at the outlets of valve 2 and 5. The drainage experiments were conducted by withdrawing water from the fully water-saturated chips with a flow rate of 0.1 μL/min.

Imbibition experiments

Before the start of an imbibition test, the chip was flushed with the gas of the experiment until the water inlet was completely filled with gas. This forced the injected water during the imbibition experiment to flow through channels filled with gas instead of pre-existing wet flow paths, which was necessary to be able to make measurements in all channel widths. The flushing was carried out at ambient pressure, after which the pressure was increased to the experimental pressure of 10 bar, except for the experiments in which the deionized water was equilibrated with CO_2. For these experiments the flushing pressure was kept at 10 bar. The imbibition experiments were conducted by injecting water with a flow rate of 0.1 μL/min into the microchip.

3.2.5 Image analysis

To calculate the dynamic contact angles, snapshots from videos of the moving gas-water interfaces in different channel widths were captured throughout the entire chip. Snapshots were taken at locations where the interfaces met the following requirements: 1) the interface is moving, 2) the interface is not too close to the corners of the channels, and 3) the meniscus snapshot is sharp. Furthermore, only one snapshot per straight channel was taken to obtain a good representation of the whole microchip.

Interfaces which met the three requirements were analysed using an in-house code. To process an image, first it was converted to a grey-scale format and the desired interface within a channel was cropped. Then, by using the scale factor of the microscope and selecting two points on the channel walls, the channel width was identified. To detect the boundary of the meniscus, the cropped section of the image was binarized and contact points, in addition to the apex, were identified. The best polynomials on each half of the curvature were fitted by both minimizing the error at the contact points (RMSE) and choosing a polynomial that optimally fits the meniscus [245, 246]. All the steps of the image analysis are shown in Figure 3.4.

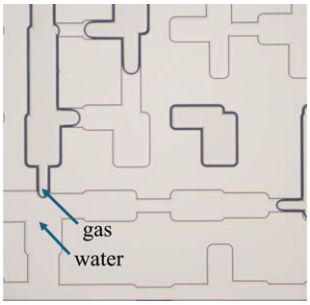

(a) Original image

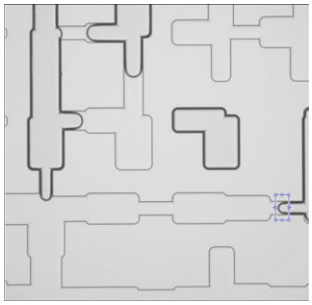

(b) Grey-scale image

(c) Binarized and cropped image

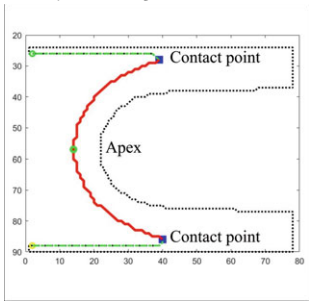

(d) Detection of interface and channel walls

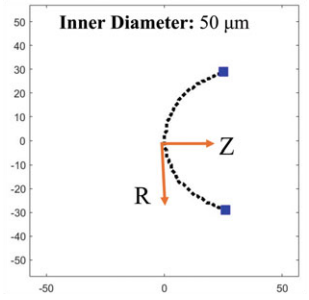

(e) Curvature from image

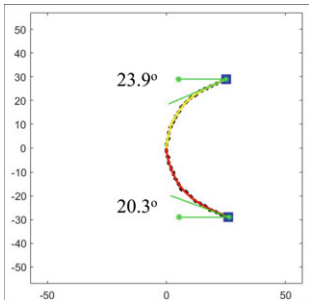

(f) Fitted 6th order polynomial on curvature

Figure 3.4: Procedure of the image analysis to identify the contact angles.

Contact angles are found first by fitting a polynomial of order n on the image, i.e.,

$$Z = c_1 R^n + c_2 R^{(n-1)} + c_i R^{n-(i-1)} + ... + c_{(n+1)}. \tag{3.1}$$

Here, c_i coefficients are constants, allowing the Z curve to be found as a function of R. Naturally, the derivative of Z with respect to R reads

$$\frac{dZ}{dR} = n c_1 R^{(n-1)} + (n-1) c_2 R^{(n-2)} + ... + c_{(n)}. \tag{3.2}$$

As such, the contact angle θ is found at the gas/liquid/solid contact point according to

$$\theta = \frac{\pi}{2} - tan^{-1}(\frac{dZ}{dR}). \tag{3.3}$$

As shown in Figure 3.4e, the origin of the coordinate system was placed at the apex point. The Z-axis is parallel to the flow direction and the R-axis perpendicular to the flow direction. Therefore, by solving Equation 3.1, 3.2 and 3.3, at the contact points the contact angle (θ) can be found. A validation of the image analysis code is provided in A.3.

3.3 Results

Figure 3.5a shows an overview image of a drainage experiment for the H_2/water system at the point of breakthrough. The flow path is different during each experiment. The small images on the right-hand-side of Figure 3.5 show drainage and imbibition examples used for measurement of advancing and receding contact angles for channel width of 70 μm and 110 μm. From left to right, the columns show the results for H_2, N_2 and CO_2, respectively. No significant difference between the wettability behaviour of these three gasses can be seen. However, in some cases a difference in interface properties (visibility of water films) could be observed between advancing and receding contact angles.

The drainage and imbibition tests were repeated until a sufficient amount of contact angle measurements for each channel width were obtained for each of the gasses, and for both drainage and imbibition. The advancing and receding contact angles (ACA and RCA) for the H_2/water, N_2/water and CO_2/water systems at a pressure of 10 (±1) bar and a temperature of 20 (±2) °C (Test A, B and C), measured in channel widths varying from 50 to 130 μm are presented in Figure 3.6. The error bars represent the standard deviation of the measurements. Table 3.2 shows the number of measurements per measurement category. Based on this data, Figure 3.7 was created in order to compare the results of all channel widths, gasses, and for both drainage and imbibition. The bars represent the mean values of of the measurements shown in Figure 3.6, and the error bars represent the standard deviation, similar to the error bars in Figure 3.6. The intrinsic contact angle of H_2/water/sandstone, measured by Hashemi *et al.* [189] (P=20 bar and T=20 °C) is indicated by the horizontal dashed line.

H_2/water receding contact angles of 6 - 23 ° and advancing contact angles of 13 - 39 ° were determined based on the microfluidic experiments. The highest angles were measured in the smallest channels and the lowest angles were measured in the widest channels. No significant difference in the receding contact angles was observed for the three different gases. The wider spread of measurements of the advancing contact angles compared to the

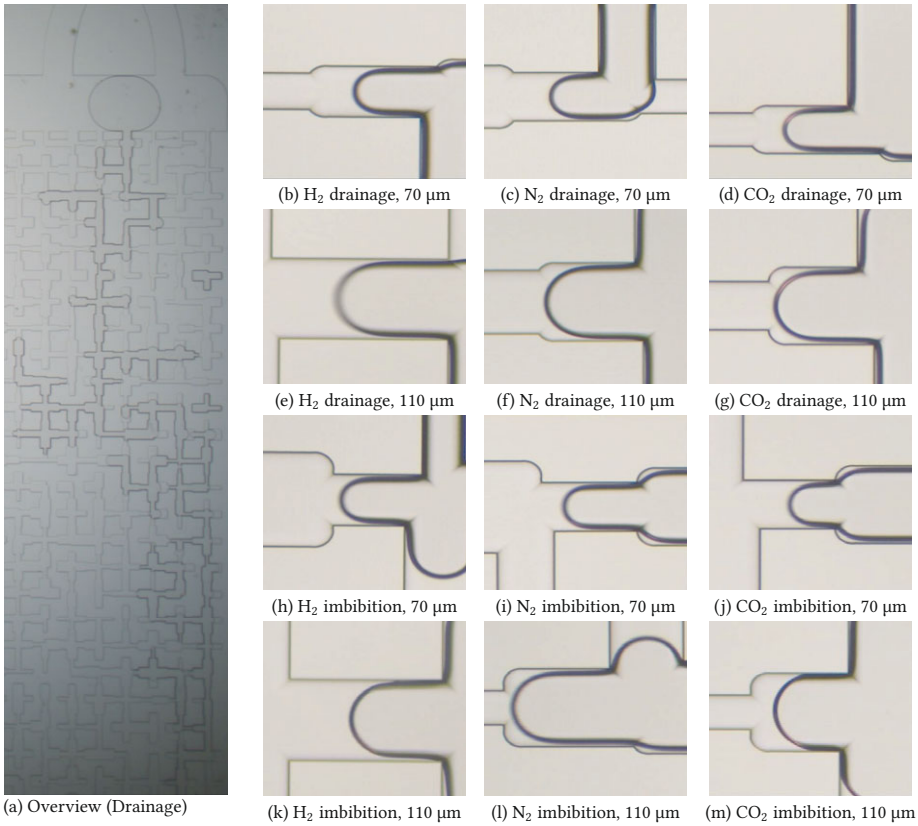

Figure 3.5: Examples of experimental images. (a) Overview image; (b–m) Drainage and imbibition for H_2, N_2, and CO_2 in 70 and 110 µm channels.

receding contact angles imply that the advancing contact angles are less reproducible. The advancing contact angles measured for the H_2/water system are larger (1 - 14°) compared to N_2/water and CO_2/water systems. However, the overlap in error bars shows that this difference is not evident and is within the experimental accuracy. This is because the error bars represent the standard deviation of the measurements, and the range in measurements is much larger than the measured difference between the gases.

The overlap in the error bars between advancing and receding contact angles for all cases studied indicates that there was no significant difference in the measured advancing contact angles and receding contact angles.

	H_2		N_2		CO_2	
Channel Width	**RCA**	**ACA**	**RCA**	**ACA**	**RCA**	**ACA**
50 µm	28	18	20	14	10	12
70 µm	24	32	22	20	12	12
90 µm	22	30	22	18	14	22
110 µm	18	24	18	14	16	20
130 µm	18	12	20	8	18	22

Table 3.2: Number of measurements.

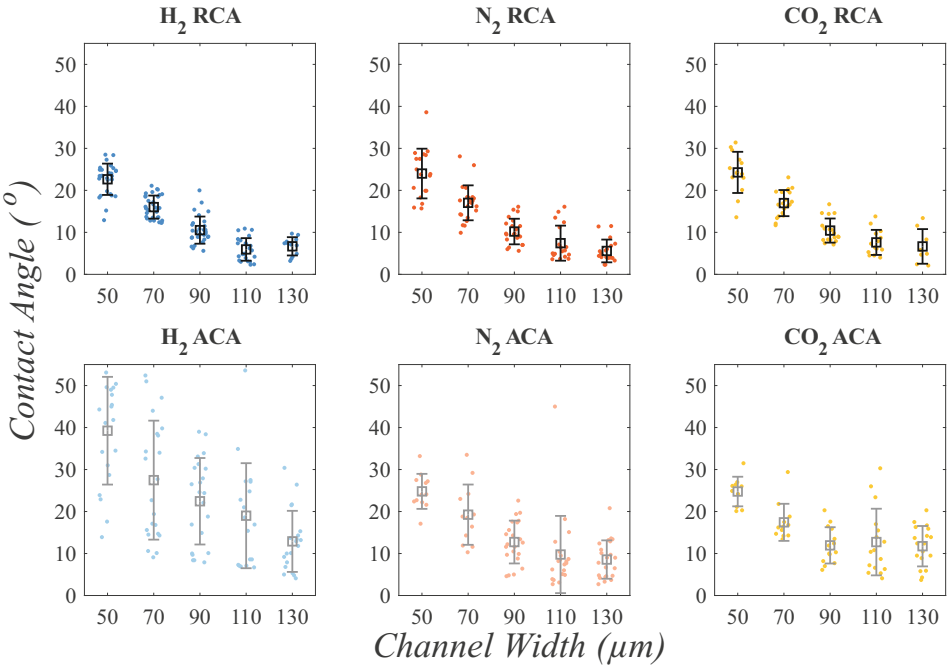

Figure 3.6: All measurement points of advancing and receding contact angles (ACA and RCA) for H_2/water, N_2/water and CO_2/water systems at P=10 bar and T=20 °C. Pure water was used for measurements with H_2 and N_2 and for the experiment with CO_2 the water was pre-equilibrated with CO_2. The error bars represent the standard deviation of the measurements.

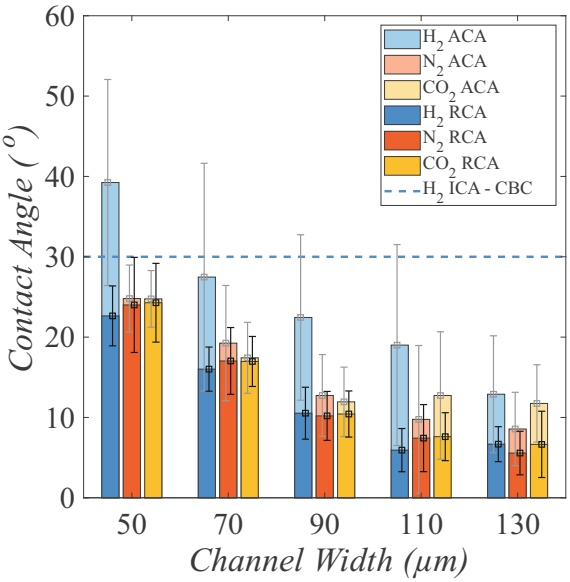

Figure 3.7: Advancing and receding contact angles (ACA and RCA) for H_2/water, N_2/water and CO_2/water systems at P=10 bar and T=20 °C. Pure water was used for measurements with H_2 and N_2 and for the experiment with CO_2 the water was pre-equilibrated with CO_2. The dashed blue line represents the results found by Hashemi *et al.* [189] at P=20 bar and T=20 °C using the captive bubble cell (CBC). The error bars represent the standard deviation of the measurements.

3.4 Discussion

The microfluidic system used in these experiments is not an accurate representation of a subsurface system because of the uniform etch depth, uniform surface chemistry, simplified pore network of the chip and relatively low temperature and pressure. However, the objective of the experiments is to derive contact angles for different channel widths and the random network of the microfluidic chip used in the experiments allowed for this. In order to find representative average values for each channel width, measurements were taken throughout the entire chip, taking into account a range of velocities and other effects like flow patterns. This type of systematic analysis would have been difficult to carry out in real rocks with complex pore-geometries. The experiments provide valuable information about the impact of channel width on the contact angle, which is needed for a basic understanding of tube flow, and can be used to improve the wettability characterization in pore-network modelling approaches. Pore-network models can be applied to derive meaningful continuum scale transport parameters such as relative permeability and capillary pressure by correctly taking into account the pore-scale physics. These hysteretic transport parameters are important input parameters for reservoir scale simulations methods which are needed for the optimization of underground hydrogen storage as well as to ensure its safety.

Underground hydrogen storage is relatively new compared to the much more mature technology of geological storage of CO_2. Understanding the similarities and differences between the H_2/water, N_2/water and CO_2/water system will help in the advancement of underground hydrogen storage, which is another objective of this study.

Because H_2 is very prone to leakage, the setup was designed such that the least amount of connections and pumps were involved. This resulted in a setup where during drainage, instead of injecting hydrogen which is the most common approach during these type of experiments, water was withdrawn. In both approaches, H_2 will first enter the pores with the lowest capillary entry pressure. When the non-wetting phase is injected, the capillary pressure ($P_c = P_{nw} - P_w$) is increased by increasing the pressure of the non-wetting phase. When the wetting phase is withdrawn as in our case, the capillary pressure is increased by lowering the pressure in the wetting phase.

3.4.1 Characteristics of the interface

During the drainage and imbibition experiments for H_2/water, N_2/water, and CO_2/water, different kind of interfaces were observed. The main difference was in the existence or non-existence of visible water films. It is important to mention that the term water film is used for all cases where water was observed on the channel walls of gas filled channels. Water on the channel walls can be caused by both corner flow and actual water films, but we will refer to it as water films, as we are not able to distinguish between the two. A water film is expected to be present in all cases [247], however, in some of our cases the water film was so thin that it was not visible with the camera. During drainage, when the receding contact angles (RCA) were measured, water films were visible on both sides of the channel (Figure 3.8d). For the measurements of advancing contact angles (ACA) during imbibition, interfaces were observed both with and without visible water films (Figure 3.8a, 3.8b and 3.8c). This was caused by the mainly dry channel walls at the start of the imbibition experiments. During the experiment, in some cases the walls of the channels were first covered with a water film before the interface arrived, while in other cases this

effect was not visible. The differences in thickness of water films caused the spread of measurements to be bigger for advancing contact angles compared to receding contact angles. Due to the curved interface of the channel walls, as well as the limitations of the microscope and camera used, the thickness of the water film could not be measured.

Figure 3.9 shows the type of interface (with or without visible water film) that was encountered at each advancing contact angle measurement for all three gasses. It can be seen that in bigger channel widths fewer measurements are without water film, since a water film can more easily enter the bigger channels. Furthermore, higher values of advancing contact angles are mainly measured without a visible water film present.

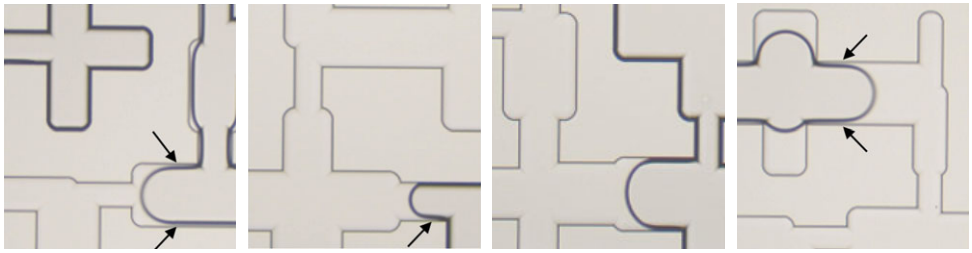

(a) ACA with water films visible on both sides (b) ACA with a visible water film on one side (c) ACA without visible water films (d) RCA with visible water films on both sides

Figure 3.8: Types of interfaces encountered during imbibition when the advancing contact angle (ACA) is measured (a–c) and during drainage when the receding contact angle (RCA) is measured (d). The visible water films are marked with an arrow.

The interfaces are very sensitive to contamination within the gas/water/glass system. The differences in contact angle measurements between clean and impure systems, as well as example images of the polluting particles can be found in A.2.

3.4.2 Influence of channel width on contact angles

According to Behnoudfar *et al.* [202], the contact angle (θ) is, besides the pore size (r), related to the radius of curvature of the interface (R) and the convergence angle of the pores (ϕ), by:

$$\theta = cos^{-1}\frac{R}{r} - \phi. \tag{3.4}$$

Because the microchip consisted of straight channels, the convergence angle in our study is equal to zero. Using this equation it can be calculated that the average radius of curvature ranges from 27 to 65 µm for the H_2/water receding contact angles and 32 to 67 µm for the H_2/water advancing contact angles. This shows that the channel width not only affects the contact angle but also the radius of curvature of the interface. In dynamic systems the radius of curvature is impacted by the velocity. In our system, a wide range of velocities were measured for each channel width. However, no systematic relationship between velocity and contact angle was observed. Furthermore, similar velocities were measured for each channel width, which suggests that the dependency of contact angle on channel width was not due to differences in velocity. Further explanation can be found in A.4.

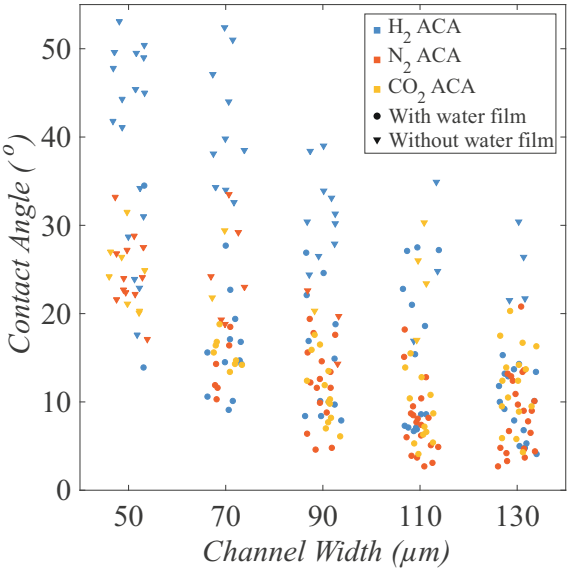

Figure 3.9: Indication of the existence or nonexistence of a visible water film in advancing contact angle (ACA) measurements for H_2, N_2 and CO_2. Note that the smallest channel, i.e., 50 μm, has only a few cases with visible water films, while the visible water films almost always exist in the channel width of 130 μm.

The results show a relationship where dynamic contact angles increase with decreasing channel width. Similar trends have been observed in the literature for CO_2/water system [218]. To theoretically explain the observed behaviour, i.e., increasing contact angle with decreasing channel width, two main situations were considered on the basis of (1) equal capillary pressure in all channel widths and (2) equal average velocity in all channel widths. Both approaches provide a trend between contact angles and channel width. The trend resulting from the first approach, i.e., equal capillary pressure in rectangular pores, derived by Joekar Niasar *et al.* [239] and explained in Eq. 4.28 A.4, does not fully match with our experimental observations. However, the trends found based on the second approach, i.e., constant velocities, as explained in Eq. A.8 A.4, matched our experimental observations pretty well. This shows that, for our specific setup and experimental condition (unsteady state), it is highly unlikely that the capillary pressure is constant across channel widths. The scientific basis for the observed trend of our study, therefore, can be found by the fact that in average the velocities across the channel widths, in our experimental condition, are comparable.

3.4.3 Comparison between advancing and receding contact angles

Besides the spread of measurements mentioned in the previous section, there was no significant difference found between the advancing and receding contact angles. Contact

angle hysteresis (the difference between advancing and receding contact angles) is the result of pore structure heterogeneity, chemical interactions between the fluid and solid rock surface, as well as surface roughness [202, 205, 206, 220]. The microchips used were made of smooth, pure borosilicate glass, and although the chip consisted of different channel widths there were no tapered structures that could lead to snap-off. Furthermore, the fluids used in the experiments were very pure since they were filtered before injection into the chip. No significant hysteresis is therefore expected. Surprisingly, the results of the work of Jafari and Jung [218] did show contact angle hysteresis for the CO2/water system using the same chip. We believe, however, that this is likely the result of impurities in the system. This is discussed in detail in A.2, which shows that impurities can cause an increase in hysteresis of contact angles due to chemical/structural imperfections.

The systematic dependency of the advancing and receding contact angles on the intrinsic contact angle that Morrow [220] found on roughened tubes was not observed in our measurements, because of the smooth channel walls of the microchip used in this experiment.

3.4.4 Comparison of gases

H_2/water, N_2/water, and CO_2/water systems behaved similarly during drainage when the receding contact angles were measured. However, a larger spread of measurements was observed in H_2 advancing contact angles in comparison to N_2 and CO_2 advancing contact angles. The minimum values of contact angles measured are similar for the three gases, while the maximum of the range of measurements of H_2 advancing contact angles is higher than N_2 and CO_2. This can be explained by the fact that more contact angles without water films were observed in the case of H_2, resulting in higher contact angles. The reason for this is currently unknown and will be part of our future work.

The similar wettability behaviour of CO_2 and N_2 has previously been observed using core-flooding experiments [248, 249]. The data on hydrogen wettability compared to other gases, however, is still limited. Note that the interfacial tension of H_2/water, N_2/water and CO_2/water at 10 bar and 25°C are, respectively, 72.9, 71.4 and 65.7 mN/m [160, 243, 250]. These values are within 10% of each other. The close interfacial tension values could provide insight on the comparable contact angles found in our experiments. Note also to the point that in a gas/liquid interface, the neighbouring molecules of the liquid are all in close proximity, while the neighbouring molecules of the gas are relatively far away. Therefore, the energy of a molecule at the interface is expected to be mainly determined by the fluid phase, while the gas phase is expected to have little impact.

3.4.5 H_2/water contact angles compared with literature

The bar plot of Figure 3.10 compares the findings on H_2/water dynamic contact angles, both advancing and receding, with the currently available literature data on dynamic contact angles measured for this system. The dynamic contact angles for the H_2/water system measured with the microfluidic device of this study (Test A) for channel widths ranging from 50 to 130 μm are presented together with the H_2/brine/quartz results of the tilted plate experiment of Iglauer *et al.* [222] (P=50 bar, T=23 °C and salinity = 100 000 ppm), referred to as TPM, and the H_2/water/sandstone core-flooding experiment of Yekta *et al.* [221] (P=50 bar and T=20 °C), referred to as CF. In addition, the horizontal blue

dashed line represents the intrinsic contact angle for the H_2/water/sandstone found by the captive-bubble experiments of Hashemi *et al.* [189] (P=20 bar and T=20 °C), referred to as CBC.

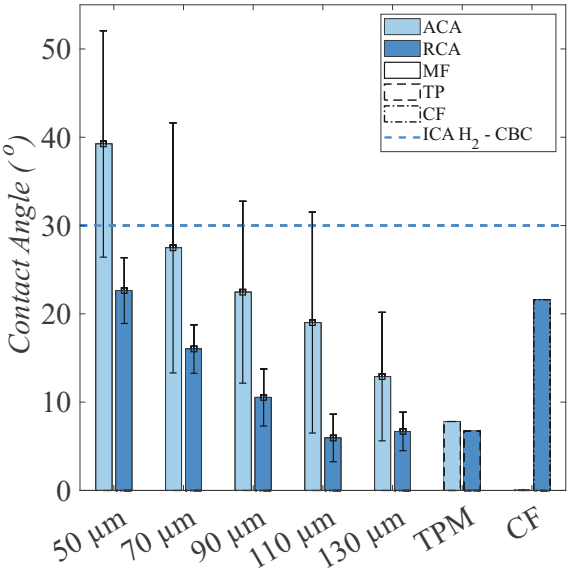

Figure 3.10: H_2/water advancing and receding contact angles (ACA and RCA) for channel widths of 50 to 130 µm found by the microfluidic experiments of this study (MF). The results of the tilted plate method of Iglauer *et al.* [222] (TPM), and the core flooding method of Yekta *et al.* [221] (CF), are represented by the bars on the right. The dashed blue line represents the results found by Hashemi *et al.* [189] at P=20 bar and T=20 °C using the captive bubble cell (CBC). The error bars represent the standard deviation of the measurements.

When comparing the results of Iglauer *et al.* [222] with the results of our microfluidic experiment, it can be seen that the results of Iglauer *et al.* [222] are similar to the results of the 130 µm channel. The receding contact angles are the same. The advancing contact angles, however, differ by 5°. In both experimental methods, the advancing contact angles are found to be less reproducible, which could explain the difference. The receding contact angle found by Yekta *et al.* [221] is very similar to the receding contact angle measured in channels of 50 µm in width, with only 1° difference. Yekta *et al.* [221] used a Vosges Sandstone for the core flooding experiment. It is possible that the common pore sizes in this sandstone are in the range of 50 µm.

3.5 Conclusions

Prediction of rock wettability in contact with brine and hydrogen is crucial for modelling the displacement processes in underground hydrogen storage (UHS). This paper reports experimental measurements of the advancing and receding contact angles of H_2/water,

N_2/water and CO_2/water systems at P = 10 bar and T = 20 °C using a microfluidic device. The channel widths of the microfluidic chip, ranged between 50 and 130 µm, and the size of the smallest channel corresponds to the range of most common pore sizes found in typical sandstones [9, 241]. Results of this study allow for more accurate design of pore-scale pore-network systems, as they require dynamic contact angles as input data. Furthermore, it can be used to understand the wide variation in the limited H_2/brine contact angle data which is currently reported. The results indicate water-wet conditions with H_2/water advancing contact angles ranging between 13 - 39 °, and receding contact angles between 6 - 23 °. The contact angles decreased with increasing channel widths. The receding contact angle measured for the smallest channel width (50 µm) is in agreement with the receding contact angle determined by Yekta *et al.* [221] on the Vosges Sandstone, suggesting that this channel width could be representative of actual subsurface systems. The N_2/water and CO_2/water systems showed similar behaviour to the H_2/water system and no significant differences were observed for the three different gases.

4

Pore-scale simulations: Geometric and operational conditions of H_2 trapping

Residual trapping is a critical mechanism influencing the efficiency of Underground Hydrogen Storage (UHS). This study investigates the underlying processes of residual trapping by by-passing, through bifurcating geometries, focusing on how geometrical parameters and flow characteristics affect the trapping process. We develop a dynamic simulation framework based on the lattice Boltzmann method (LBM) to simulate full drainage/imbibition cycles. Various geometries, based on the pore doublet model, were investigated and supported by theoretical analysis. In addition, trapping behaviour of hydrogen was compared to that of CO_2 and CH_4. It is found that the channel width ratio, specially across the local bifurcating geometries, and the roundness of the grains, are among the key factors which control hydrogen trapping. Results indicate that the suited reservoirs for underground hydrogen storage have narrower channel-size ratios and smoother edges at micro-scale. Operational conditions also play a significant role. Lower flow rates enhance bypassing, which increases trapping.

This chapter was published in the International Journal of Hydrogen Energy **Vol. 177**, (2025) [251].

4.1 Introduction

For a successful transition towards net-zero goals, it is crucial to upscale green energy systems, from production to transportation and specially storage [1–4]. Hydrogen, H_2, with its high gravimetric energy density and clean combustion products, can be a remedy to the long-standing challenge of TWh-scale energy storage [6–8]. Indeed, hydrogen can be stored in large quantities in geological formations, such as depleted hydrocarbon reservoirs, aquifers, and salt caverns [9–13].

The efficiency of underground hydrogen storage (UHS) in porous reservoirs is highly dependent on the flow and transport behaviour during alternating injection and withdrawal cycles in the reservoir, which is governed by complex pore-scale processes [9, 31, 48]. Among the major mechanisms influencing UHS efficiency, residual trapping plays a critical role and is considered a significant source of hydrogen loss [48, 252]. This is specially due to the fact that for UHS, hydrogen has to be trapped only temporarily and become mobile when extracted [253]. Residual trapping, however, is a mechanism that permanently traps hydrogen molecules in the subsurface microchannels. As such, residual trapping of hydrogen needs to be extensively investigated and properly managed in field-scale operations. Note that experimental studies have reported residually-trapped hydrogen saturation values as high as 44 %, underscoring the importance of investigating its value upfront for proper site selection and effective operation [30, 254–259].

Residual trapping, or capillary trapping, is defined as the fraction of hydrogen fluid that becomes immobile as disconnected volumes within the brine-saturated porous channels. The trapping is influenced by the pore geometry and the fluid-fluid and solid-fluid interactions [260], and can occur when capillary forces dominate over the other acting mobilizing forces, such as buoyancy, inertia, and viscous forces [261]. The two main capillary trapping mechanisms are bypassing trapping and snap-off [262, 263]. Bypass trapping can be studied using the pore doublet model, i.e., a bifurcating channel splitting geometry [264–266]. This bifurcating geometrical structure consists of two channels with different channel widths splitting from a main flowing stream. It is specially used as a conceptualized model of the pore structure for the interpretation of the bypassing trapping mechanism, when non-wetting phase is displaced by the wetting phase [267, 268]. Although conceptualized, the pore doublet model is used to gain deep understanding of the actual flow paths within complex pore networks, specially when channel splitting with sharp corners occurs. It can also serve as a building block for a larger network of channels, when scaled up into forming a microfluidic-type structured channelized system [186]. Recently, significant analytical and numerical advances have been made in understanding the pore doublet model, including the development of an analytical solution describing immiscible displacement dynamics [269]. In addition, Gu *et al.* [270] established a mathematical model and conducted numerical simulations to characterize the imbibition preference within the pore doublet. The pore doublet model has been extensively used in both experimental and analytical studies to investigate oil entrapment [262, 264–266, 271, 272]. However, it has not yet been applied to the H_2/brine system, which exhibits significantly different fluid properties.

Residual trapping can be studied experimentally using core flood experiments [30, 37, 268, 273, 274, 274] and micromodels [268, 275, 276]. However, these experiments can be challenging, time-consuming, and expensive and can only be carried out at limited

conditions and with a limited number of samples [45, 221, 277]. Alternatively, numerical pore-scale simulations can be used to predict and understand trapping [37–43].

There are two main types of pore-scale simulations: Pore-Network Modelling (PNM) and fully-resolved simulations computational fluid dynamics (CFD) approach. In PNM, simulations are carried out using extensively simplified representations extracted from rock samples [9]. Pore volumes are represented as interconnected pores connected through throats. In fully-resolved CFD simulations, the pore structures are represented more explicitly, from either experimental characterization or numerical reconstruction, using what is referred to as digital rock technology [278]. Commonly employed CFD methods include the lattice Boltzmann method (LBM) [44], Level-Set method [279], and the Volume of Fluid (VoF) method [280].

LBM simulates the movement of an ensemble of particles on a lattice using the Boltzmann equation [45]. More traditional CFD methods are based on Navier-Stokes equations and use methods such as the VoF or the Level-Set method for interface tracking. Due to its good mass conservation properties and sharp interface representation, the VoF approach has been used in the literature [45, 281]. However, LBM presents several notable advantages. One of its key strengths is its suitability for simulating flow in porous media, as it effectively handles complex geometries and boundary conditions with a relatively simple approach. Furthermore, LBM is amenable for parallel processing, enhancing its domain size relevance to what is expected to be a representative elementry volume in porous media systems [282–285].

In the context of UHS, various experimental and numerical studies at the core- and/or pore-scale have investigated residual trapping mechanisms and flow efficiency [9, 30, 253–259, 286–290]. However, a limited number of studies have systematically focused on the underlying processes of residual trapping, specifically examining the physical and geometrical conditions that facilitate residual trapping in UHS scenarios. Similar as more structured micro-channel geometries [186], Lysyy *et al.* [288] and Lysyy *et al.* [257] also used microfluidics to study the displacement and trapping mechanisms of hydrogen in an aquifer storage scenario. Trapping by bypassing was one of the observed trapping mechanisms within their experiments. Wang *et al.* [278] conducted pore-scale simulations through the VoF method, to analyze hydrogen transport within a pore network representative under varying wetting conditions. They reported that, as expected, increasing hydrogen wettability is unfavorable for the extraction process. Similarly, Bagheri *et al.* [291] employed the VoF method in pore-scale simulations, to investigate the effect of flow regime, compressibility, and hysteresis on flow pattern, trapping mechanisms, and efficiency of hydrogen storage and found that lower flow rates favour capillary trapping through snap-off. Lastly, Yu *et al.* [261] reported the only study systematically focussing on the influence of pore geometry on trapping, a study that was also investigated in PNM on more simplified geometries [9]. They conducted pore-scale simulations through the VoF method to investigate the effects of pore geometry and injection rate on trapping via dead-end bypassing. They reported that higher injection rates cause more trapping by this mechanism. However, studies investigating other pore geometries than dead-end pores and their effect on trapping relevant to UHS are currently missing in the literature.

The objective of this study is to systematically investigate how physical and geometrical conditions influence the underlying trapping mechanisms in the context of UHS.

Specifically, for bifurcating geometries, we examine the impact of (a) channel width ratio, (b) pore shape, (c) capillary number and flow velocity, and (d) fluid properties, through a comparison of the trapping behaviour of H_2 with that of CH_4 and CO_2, on residual trapping by bypassing. To achieve this, we perform pore-scale simulations using our in-house developed lattice Boltzmann method, exploring various geometries. These geometries are chosen to conceptualize the splitting of streamlines, with and without sharp corners, into separate channels with various width aspect ratios. This fundamental study allows to identify what mechanism is driving hydrogen trapping in porous media with a wide range of channel widths and sharp corners. Specially we aim to analyze if those trapped hydrogen volumes can be mobilized by changing the flow rate, i.e., capillary number. What comes next indeed reveals the strength of LBM in allowing us to identify the process that leads to entrapment of hydrogen in bifurcating situations, and revealing in what way this can also help for better site selection based on the rock channel width distribution.

The structure of this paper is as follows: Section 4.2 outlines the methodology, including the governing equations and simulation methods. Section 4.3 describes the simulation setup, fluid properties, and pore geometries. In Section 4.4 we present a theoretical analysis, and in Section 4.5, we present the simulation results, and their application to underground hydrogen storage. Finally, the key findings are summarized in Section 5.11.

4.2 Methodology

4.2.1 Lattice Boltzmann Method for Immiscible Two-Phase Flow

In this work, an immiscible two-phase color gradient LBM model [292–294] is developed. Two immiscible fluids are described by two sets of distribution functions f_α^R and f_α^B, where the two fluids are marked as red and blue phases. The total distribution function is defined as $f_\alpha = f_\alpha^R + f_\alpha^B$, which undergoes the collision step of

$$f_\alpha^*(\mathbf{x}, t) = f_\alpha(\mathbf{x}, t) + \Omega_\alpha(\mathbf{x}, t) + \bar{F}_\alpha(\mathbf{x}, t), \tag{4.1}$$

where $f_\alpha(\mathbf{x}, t)$ is the total distribution function along α-direction at time t and position vector $\mathbf{x}$, f_i^* is the post-collision distribution function, Ω_α is the collision operator, and $\bar{F}_\alpha$ is the forcing term. To enhance the numerical stability, the multiple–relaxation–time (MRT) [295–298] scheme is used, and the collision operator reads

$$\Omega_\alpha(\mathbf{x}, t) = -\left(\mathbf{M}^{-1}\mathbf{S}\mathbf{M}\right)_{\alpha\beta}\left(f_\beta(\mathbf{x}, t) - f_\beta^{eq}(\mathbf{x}, t)\right). \tag{4.2}$$

The transformation matrix $\mathbf{M}$ maps the distribution functions and their equilibrium ones onto the moment space, that is, $\mathbf{m} = \mathbf{M}\mathbf{f}$, $\mathbf{m}^{\mathrm{eq}} = \mathbf{M}\mathbf{f}^{\mathrm{eq}}$, where $\mathbf{m}$ (and $\mathbf{m}^{\mathrm{eq}}$) denote the vector of macroscopic moments, specifically defined as:

$$\mathbf{m} = \left(\rho, e, \varepsilon, j_x, q_x, j_y, q_y, p_{xx}, p_{xy}\right)^T, \tag{4.3}$$

where ρ is the density, e is the internal energy, ε is the square of internal energy, j_x and j_y are the momentum components in the x and y directions, respectively, q_x and q_y are the energy fluxes, and p_{xx} and p_{xy} represent the diagonal and off-diagonal components of the

stress tensor. The transformation matrix **M** is explicitly given by

$$\mathbf{M} = \begin{pmatrix} 1 & 1 & 1 & 1 & 1 & 1 & 1 & 1 & 1 \\ -4 & -1 & -1 & -1 & -1 & 2 & 2 & 2 & 2 \\ 4 & -2 & -2 & -2 & -2 & 1 & 1 & 1 & 1 \\ 0 & 1 & 0 & -1 & 0 & 1 & -1 & -1 & 1 \\ 0 & -2 & 0 & 2 & 0 & 1 & -1 & -1 & 1 \\ 0 & 0 & 1 & 0 & -1 & 1 & 1 & -1 & -1 \\ 0 & 0 & -2 & 0 & 2 & 1 & 1 & -1 & -1 \\ 0 & 1 & -1 & 1 & -1 & 0 & 0 & 0 & 0 \\ 0 & 0 & 0 & 0 & 0 & 1 & -1 & 1 & -1 \end{pmatrix}. \tag{4.4}$$

The MRT operator allows each moment to relax at its own rate, with the relaxation rates stored in a diagonal matrix given by

$$S = \mathrm{diag}(s_0, s_1, s_2, s_3, s_4, s_5, s_6, s_7, s_8), \tag{4.5}$$

where the s_α denote the relaxation time for the α^{th} moment in Eq. 4.5, in which s_{0-6} are constants and the values are followed the work of Xu *et al.* [293], specifically, $s_0 = 1$, $s_1 = 1.64$, $s_2 = 1.54$, $s_3 = 1$, $s_4 = s_6 = 1.9$, $s_5 = 1$; the parameter s_7 and s_8 are equal to $\frac{1}{\tau}$, where τ is the relaxation time that related to the kinematic viscosity ν, i.e.,

$$\nu = (\tau - 0.5)c_s^2 \delta t. \tag{4.6}$$

Here, c_s is the lattice sound speed in the D2Q9 model, defined as $c_s = c/\sqrt{3}$ with $c = \delta x/\delta t$. In this study, both δx and δt are set to unity. To account for the viscosity difference of the two phases, a harmonic mean is used to determine the viscosity of the fluid mixture [292], i.e.,

$$\frac{1}{\nu} = \frac{1+\rho^N}{2\nu_R} + \frac{1-\rho^N}{2\nu_B}, \tag{4.7}$$

where ν_R and ν_B are the kinematic viscosity of the fluids, and ρ^N is the phase field and is defined as

$$\rho^N(\mathbf{x}, t) = \frac{\rho_R(\mathbf{x}, t) - \rho_B(\mathbf{x}, t)}{\rho_R(\mathbf{x}, t) + \rho_B(\mathbf{x}, t)}. \tag{4.8}$$

f_α^{eq} is the discrete equilibrium Maxwellian distribution function expressed by

$$f_\alpha^{eq} = \rho\omega_\alpha \left[1 + \frac{\mathbf{e}_\alpha \cdot \mathbf{u}}{c_s^2} + \frac{(\mathbf{e}_\alpha \cdot \mathbf{u})^2}{2c_s^4} - \frac{\mathbf{u}^2}{2c_s^2}\right], \tag{4.9}$$

where $\rho = \rho_R + \rho_B$ is the total density, and ρ_R and ρ_B are the densities of red and blue fluids, respectively, $\mathbf{u}$ is the velocity of the fluid, $\mathbf{e}_\alpha$ is a vector of discrete velocities, c_s is the speed of sound, ω_α is the weighting factor. Here the two-dimensional nine-velocity (D2Q9) model is used, with the discrete velocities given by $\mathbf{e_0} = (0,0)$, $\mathbf{e_1} = -\mathbf{e_3} = (c,0)$, $\mathbf{e_2} = -\mathbf{e_4} = (0,c)$, $\mathbf{e_5} = -\mathbf{e_7} = (c,c)$, and $\mathbf{e_6} = -\mathbf{e_8} = (-c,c)$, where $c = \delta x/\delta t = \sqrt{3c_s^2}$, δx and δt are lattice spacing and time step, which are defined as unity; the weighting factor ω_α is given by $\omega_0 = 4/9$, $\omega_{1-4} = 1/9$, and $\omega_{5-8} = 1/36$.

The forcing term $\bar{F}_\alpha$ generates the interfacial tension between phases. In MRT scheme [299], the forcing term, first proposed by Guo *et al.* [300], is expressed as

$$\bar{\mathbf{F}} = \mathbf{M}^{-1}\left(\mathbf{I} - \frac{1}{2}\mathbf{S}\right)\mathbf{M}\tilde{\mathbf{F}}, \tag{4.10}$$

where $\mathbf{I}$ is a 9×9 unit matrix, $\mathbf{M}$ is the transformation matrix defined by Eq. 4.4 and $\tilde{\mathbf{F}}$ is given by

$$\tilde{F}_\alpha = \omega_\alpha\left[\frac{\mathbf{e}_\alpha - \mathbf{u}}{c_s^2} + \frac{(\mathbf{e}_\alpha\cdot\mathbf{u})\mathbf{e}_\alpha}{c_s^4}\right]\cdot\mathbf{F_s}\delta t, \tag{4.11}$$

where $\mathbf{F_s}$ is the body force that produces the local stress jump across the interface. Based on the continuum surface force (CSF) model of Brackbill *et al.* [301], the body force can be expressed as [302]

$$\mathbf{F_s} = -\frac{1}{2}\sigma\kappa\nabla\rho^N, \tag{4.12}$$

where σ is the interfacial tension, and κ is the local interface curvature, which is calculated by

$$\kappa = -\nabla_s\cdot\mathbf{n} = -(\mathbf{I} - \mathbf{nn})\cdot\nabla\cdot\mathbf{n}. \tag{4.13}$$

Here, $\mathbf{n}$ is the unit normal vector defined as $\mathbf{n} = -\frac{\nabla\rho^N}{|\nabla\rho^N|}$. The local velocity takes the form as in

$$\rho\mathbf{u}(\mathbf{x},t) = \sum_\alpha e_\alpha f_\alpha(\mathbf{x},t) + \frac{\delta t}{2}\mathbf{F_s}(\mathbf{x},t), \tag{4.14}$$

to incorporate the spatially varying body force [300]. In order to minimize the discretization errors, the nine-point compact finite-difference stencil is used in calculating the partial derivatives of the normal vector and the interface curvature.

To promote phase segregation and maintain a reasonable interface, the recoloring algorithm proposed by Latva-Kokko and Rothman [303] is adapted, the recolored distribution function of the fluids, f_α^{R**} and f_α^{B**}, are

$$\begin{aligned} f_\alpha^{R**} &= \frac{\rho_R}{\rho}f_\alpha^*(\mathbf{x},t) + \beta\frac{\rho_R\rho_B}{\rho}\omega_\alpha\cos(\varphi_\alpha)|\mathbf{e}_\alpha|, \\ f_\alpha^{B**} &= \frac{\rho_B}{\rho}f_\alpha^*(\mathbf{x},t) - \beta\frac{\rho_R\rho_B}{\rho}\omega_\alpha\cos(\varphi_\alpha)|\mathbf{e}_\alpha|, \end{aligned} \tag{4.15}$$

where β is the segregation parameter and is free to adjust, in this work, it is set to be 0.7, ϕ_α is the angle between the phase field gradient $\nabla\rho^N$ and the lattice vector $\mathbf{e}_\alpha$, defined by

$$\cos(\varphi_\alpha) = \frac{\mathbf{e}_\alpha\cdot\nabla\rho^N}{|\mathbf{e}_\alpha||\nabla\rho^N|}. \tag{4.16}$$

After the recoloring step, the distribution functions of red and blue phases propagate to the neighboring lattice nodes, known as propagation or streaming step:

$$\begin{aligned} f_\alpha^R(\mathbf{x}+\mathbf{e}_\alpha\delta t, t+\Delta t) &= f_\alpha^{R**}(\mathbf{x},t), \\ f_\alpha^B(\mathbf{x}+\mathbf{e}_\alpha\delta t, t+\Delta t) &= f_\alpha^{B**}(\mathbf{x},t). \end{aligned} \tag{4.17}$$

The post-propagation distribution functions are then used to obtain the local density of both fluids by $\rho_R = \sum_\alpha f_\alpha^R$ and $\rho_B = \sum_\alpha f_\alpha^B$. Equations 4.1-4.17 together define the complete evolution process, consisting of collision (Eqs. 4.1-4.2 and 4.10), recoloring (Eq. 4.15), and propagation/streaming (Eq. 4.17).

4.2.2 Wetting Boundary Condition

In this work, the wetting boundary condition is imposed to achieve the prescribed contact angle θ at the solid surface, following the approach of Xu *et al.* [293]. The main steps are as follows: (1) estimate the ρ^N at the boundary solid nodes, (2) evaluate the color gradient $\Delta\rho^{N*}$ in boundary fluid nodes using the estimated ρ^N, and (3) correct the color gradient so that the local contact angle matches the desired value.

First, for each boundary solid node $x \in C_{S_B}$, the ρ^N is estimated by a weighted average of the neighboring fluid nodes, i.e.,

$$\rho^N(x) = \frac{\sum\limits_{\alpha,\, x+\mathbf{e}_\alpha \delta t \in C_{F_B}} \omega_\alpha \, \rho^N(x+\mathbf{e}_\alpha)}{\sum\limits_{\alpha,\, x+\mathbf{e}_\alpha \in C_{F_B}} \omega_\alpha}, \qquad x \in C_{S_B} \tag{4.18}$$

where C_{F_B} is the set of fluid nodes at the solid-fluid interface, C_{S_B} is the set of boundary solid nodes, ω_α are the weight coefficients, and $\mathbf{e}_\alpha$ are the discrete lattice velocities. The color gradient $\Delta\rho^{N*}$ at each fluid node near the boundary is then computed through nine-point compact finite-difference stencil, which needs to be modified to achieve the desired contact angle.

Next, the orientation of $\Delta\rho^{N*}$ in C_{F_B} is calculated as

$$\mathbf{n}^* = \frac{\Delta\rho^{N*}}{|\Delta\rho^{N*}|}. \tag{4.19}$$

In two dimensions, there are two possible candidate interface normal vectors at the contact line, $\mathbf{n}_1$ and $\mathbf{n}_2$ corresponding to the prescribed contact angle θ, which can be obtained by rotating the unit normal vector of the solid surface $\mathbf{n}_s = (n_{s,x}, n_{s,y})$ by θ in the positive and negative senses, i.e.,

$$\begin{aligned} \mathbf{n}_1 &= (n_{s,x}\cos\theta - n_{s,y}\sin\theta, \;\; n_{s,y}\cos\theta + n_{s,x}\sin\theta), \\ \mathbf{n}_2 &= (n_{s,x}\cos\theta + n_{s,y}\sin\theta, \;\; n_{s,y}\cos\theta - n_{s,x}\sin\theta). \end{aligned} \tag{4.20}$$

The correct unit normal vectors for the color gradient in C_{F_B} are selected by comparing the Euclidean distances to $\mathbf{n}^*$, i.e.,

$$\begin{aligned} D_1 &= |\mathbf{n}^* - \mathbf{n}_1| \\ D_2 &= |\mathbf{n}^* - \mathbf{n}_2|, \end{aligned} \tag{4.21}$$

The unit normal vector is then selected as

$$\mathbf{n} = \begin{cases} \mathbf{n}_1, & D_1 < D_2 \\ \mathbf{n}_2, & D_1 > D_2 \\ \mathbf{n}_s, & D_1 = D_2 \end{cases} \tag{4.22}$$

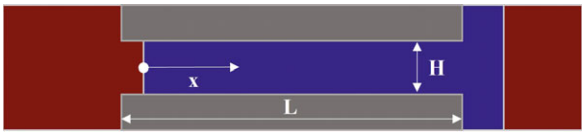

Figure 4.1: Schematic of capillary intrusion.

Finally, the color gradient vector at the boundary is modified as

$$\Delta\rho^N = |\Delta\rho^{N*}|\,\mathbf{n}, \tag{4.23}$$

ensuring that the local interface orientation matches the desired contact angle. This algorithm provides robust and accurate wetting boundary conditions for arbitrary contact angles and complex geometries, and is effective for two-phase lattice Boltzmann simulations in porous media.

The above color-gradient LBM was programmed in MATLAB, with the computational efficiency enhanced through parallel computing on the graphics processing unit (GPU), utilizing MATLAB's built-in functions (i.e. $conv2$ for calculating the partial derivatives and $pagefun$ for three-dimensional matrix operations). The simulations in this work were performed using the RTX 4090 GPU on workstations.

4.2.3 Capillary Intrusion Validation

To verify the developed model, the capillary intrusion test is performed. As sketched in Figure 4.1, the simulation domain is a 2D capillary tube placed horizontally: The wetting phase penetrates the tube that initially filled by the non-wetting phase. This imbibition process is determined by the balance between capillary and viscous forces of the fluids, which can be expressed as

$$\sigma\cos(\theta) = \frac{6}{H}\left[\mu_L x + \mu_V (L-x)\right]\frac{dx}{dt}, \tag{4.24}$$

where θ is the contact angle, L and H are the length and width of the capillary tube, respectively; x is the location of the interface, μ_L and μ_V are dynamic viscosities of liquid and vapor phases [292]. The domain is discretized into 600×15 lattice points with $L = 300$ and $H = 5$ for the capillary tube with periodic boundary conditions in the x direction. Here we take brine displacing H_2 as example, and the parameters used in the simulation are listed in Table 4.2. Periodic boundary conditions are imposed on the region occupied by fluid.

We consider two cases with the contact angle given by $\theta = 35^\circ$ and $\theta = 70^\circ$. Figure 4.2 presents the comparisons between numerical simulations from LBM and the analytical predictions of Eq. 4.24. Good agreement was observed with capillary width H being 5, which was smaller than the smallest pore width in the following cases, ensuring that grid resolution is sufficient to capture the underlying dynamic processes.

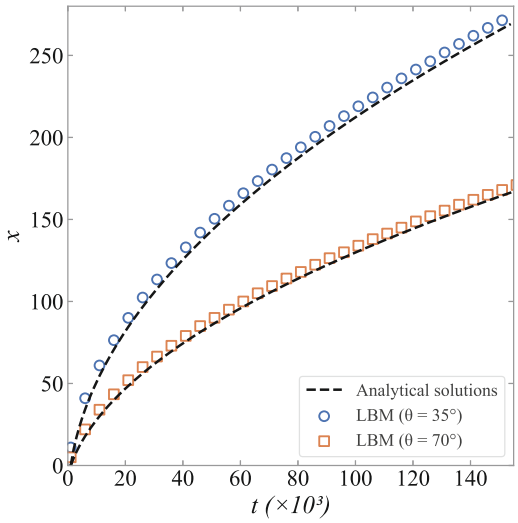

Figure 4.2: Capillary intrusion tests: comparison between LBM simulations and theoretical predictions.

4.3 Simulation setup and pore-scale characterization

4.3.1 Fluid properties

The physical properties of H_2, CH_4, and CO_2 are listed in Table 4.1. These properties represent the conditions of a temperature of 40 °C and a pressure of 11 MPa, corresponding to a reservoir at a depth of 1100 meters, which is identified as the optimal depth for hydrogen storage [304]. For the brine, a molality of 2.0 mol NaCl/L was selected, and the corresponding properties were applied. The contact angles, which are similar for the three gases, were derived from experimental measurements [189, 223, 305]. All measurements were conducted in the same laboratory using the Captive Bubble method on sandstone samples, providing a consistent basis for comparison. To convert the physical properties into lattice units, fixed scaling parameters for length, mass, and time were applied, resulting in the values presented in Table 4.2.

The densities of both the gas and the brine were set to one, assuming negligible inertial forces in the system, consistent with low Reynolds numbers and laminar flow conditions [306]. This simplification excludes gravitational (buoyancy-driven) effects, which may become relevant in larger-scale systems, but were not the focus of this capillarity-driven trapping study [306, 307]. The mass scaling factor was calculated based on the liquid density. In these simulations, dynamic viscosity ratios were used. Using dynamic viscosities ensures a realistic representation of the mobility of both the gas and the liquid phase.

4.3.2 Pore geometry

The primary pore geometry used in this study is the pore doublet model, shown in Figure 4.3 (left). Although highly idealized compared to real pore networks, this geometry captures key aspects of preferential flow and multiphase displacement behaviour in porous media [269, 311]. Its simplicity allows for isolating the fundamental physical mechanisms governing

Property	Unit	H_2	CH_4	CO_2
Density gas, ρ_{gas}	kg/m^3	8.00	77.6	683
Density liquid, ρ_{brine}	kg/m^3	1066	1066	1066
Dynamic Viscosity gas, μ_{gas} ($\nu_{gas} \cdot \rho_{gas}$)	µPa·s	9.47	14.3	54.1
Dynamic Viscosity liquid, μ_{brine} ($\nu_{brine} \cdot \rho_{brine}$)	µPa·s	790	790	790
Viscosity ratio gas/brine M	-	0.012	0.018	0.068
Surface tension, σ	mN/m	66	58	39
Contact angle, θ	°	35	35	30

Table 4.1: Physical units of H_2, CH_4, CO_2, and brine (2.0 mol NaCl/L) at T = 40 °C and P = 11 MPa. Values are taken based on the literature [47, 173, 174, 189, 223, 305, 308–310].

Property	Unit	H_2	CH_4	CO_2
Density gas, ρ_{gas}	M/L^3	1	1	1
Density liquid, ρ_{brine}	M/L^3	1	1	1
Dynamic Viscosity gas, μ_{gas} ($\nu_{gas} \cdot \rho_{gas}$)	M/L·T	0.0060	0.0091	0.034
Dynamic Viscosity liquid, μ_{brine} ($\nu_{brine} \cdot \rho_{brine}$)	M/L·T	0.50	0.50	0.50
Viscosity ratio gas/brine M	-	0.012	0.018	0.068
Surface tension, σ	M/T^2	0.19	0.16	0.11
Contact angle, θ	°	35	35	30

Table 4.2: Lattice units of H_2, CH_4, CO_2, and brine, used in the numerical simulations, expressed in units of mass (M), length (T) and time (T).

trapping due to bypassing, which are relevant to more complex geological systems. The pore doublet model comprises an inlet channel that bifurcates into two parallel channels with different widths, d_1 and d_2, before merging into a single outlet channel. To investigate the effect of pore shape, a rounded version of the pore doublet model is also employed (Figure 4.3 (right)). The rounded model has the same inlet width, d_1, as the rectangular pore doublet model, to maintain consistency. In all geometries d_1 is set as 15, and the corresponding d_2 is set based on the channel width ratio.

4.3.3 Simulation setup

The Zou–He type boundary conditions are adopted in this study [312, 313], with a constant pressure prescribed at the inlet and a zero-pressure condition at the outlet. To achieve no-slip condition, the halfway bounce-back scheme [314, 315] is applied at the solid walls. The inlet velocity caused by the set pressure gradient, is used to define the capillary number, which is defined as

$$Ca \equiv \frac{\mu_{gas} \cdot |V_{inlet}|}{\sigma}. \tag{4.25}$$

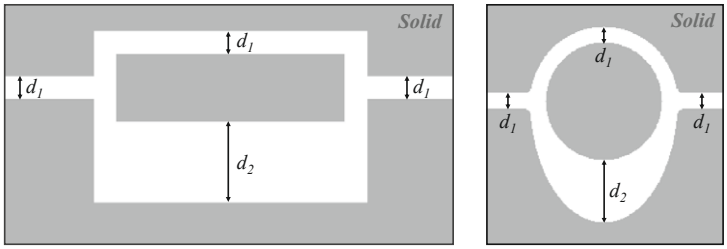

Figure 4.3: Pore geometries used in this study: (left) Rectangular pore doublet model, (right) Rounded pore doublet model.

The investigated capillary numbers are in the range of 10^{-4}, which is relevant for the UHS systems [316]. At the start of the simulation, the system is fully saturated with brine, and a volume fraction of 100% gas is set at the left boundary. As the pressure gradient is applied, gas flows into the system from the left boundary, simulating the drainage process. During the drainage phase, no gas trapping is expected. However, this phase is included to establish a realistic initial phase distribution for the subsequent imbibition phase. Once the gas reaches the right boundary of the simulation box, the imposed pressure gradient is reversed and adjusted, resulting in the specific capillary number of the test (which are in the range of 10^{-4}). The volume fraction at the right boundary is then set to 100% brine, simulating brine injection from this boundary (imbibition). The simulation ends when no further changes in phase distribution occur.

4.3.4 Test cases

The goal of the simulations is to understand trapping due to bypassing in H_2/brine systems. More specifically, we aim to understand the impact of (a) channel width ratio, (b) pore shape, (c) capillary number and flow velocities, and (d) fluid properties, through a comparison of the trapping behaviour of H_2 with that of CH_4 and CO_2.

A series of simulations have been carried out in which the channel width ratio (d_2/d_1) was varied in the rectangular pore doublet from 2.5 to 5.0. To investigate the influence of pore/grain shape, similar simulations were carried out using the rounded pore doublet with a channel width ratio from 4.0 to 6.0. To assess the role of fluid properties in trapping behaviour, simulations are carried out for H_2 as well as for CH_4 and CO_2.

4.4 Theoretical Analysis of the pore doublet model

To understand the outcome of our numerical simulations, we conduct a theoretical analysis of bypassing in the pore doublet model. The pore doublet model is a parallel arrangement of a small and large-diameter channel, and is used as an idealized model of a pore structure for the interpretation of trapping of the non-wetting phase by the displacing wetting fluid during immiscible displacement in permeable porous media [267, 268]. A schematic pore doublet model is presented in Figure 4.4.

The entrapment of oil, as a non-wetting fluid, has been studied extensively by various researchers [264, 265, 272, 317]. Their analyses indicate that, under specific conditions, the fluid interface in the small capillary at point A will progress towards point B, while

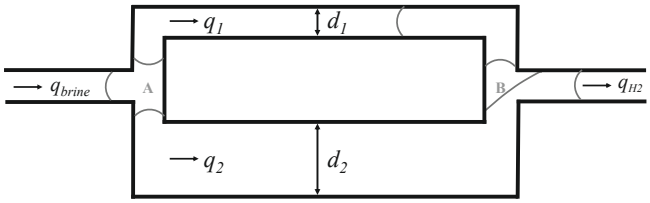

Figure 4.4: Pore doublet model representation of imbibition (inspired by Chatzis and Dullien [268]).

the interface in the larger capillary remains stationary. This behaviour is attributed to the higher capillary pressure in the narrow channel, which makes it the preferential flow path. However, once the interface in the smaller capillary reaches point B, it may also become stationary. This occurs because further advancement requires the expansion of the interface area, which affects the capillary pressure.

In some cases, the interface expands until it contacts the opposite wall of the channel, leading to a snap-off event. When this happens, the non-wetting fluid becomes trapped in the larger capillary. Conversely, under different conditions, the interface in the larger capillary may also advance towards point B, preventing fluid trapping in the system.

To further understand the simulation results, a complete set of dimensionless parameters governing the behaviour of this system is derrived in Appendix B.1

4.4.1 Pressure Balance and trapping conditions

The pressure drop across each channel is the sum of the capillary pressure and the viscous pressure drop [264]. Because the two channels are interconnected at both ends, the overall pressure difference in the two channels is identical [266, 268]. During imbibition, as the wetting fluid enters the system, capillary pressure enhances the flow velocity, while the viscous forces act to resist the flow. Consequently, capillary forces and viscous forces operate in opposing directions. When the pressure gradients in the inlet and outlet channels are negligible, this equivalence approximates the overall pressure difference between the inlet and outlet:

$$P_{inlet} - P_{outlet} \approx P_{c_1} - \Delta P_1 = P_{c_2} - \Delta P_2, \tag{4.26}$$

where P_{inlet} and P_{outlet} denote the set pressures at the inlet and outlet, respectively. The terms P_{c_1} and P_{c_2} represent the capillary pressures in channels 1 and 2, and ΔP_1 and ΔP_2 correspond to the viscous pressure drops in channels 1 and 2, respectively.

The viscous pressure drop in each channel can be estimated by the Hagen-Poiseuille equation [272, 317], i.e.,

$$\Delta P_j = \frac{128 q_j \mu l}{\pi d_j^4} \quad (j = 1, 2), \tag{4.27}$$

where d_1 and d_2 are the diameters of the large and small capillaries, respectively, l is the length of the flow path in the doublet, and μ is the dynamic viscosity. Equation 4.27 assumes cylindrical capillaries and laminar flow.

The magnitude of capillary pressure P_c can be estimated by the Young-Laplace equation:

$$P_{cj} \equiv (P_{nw} - P_w)_j = \frac{4\sigma \cos\theta}{d_j} \quad (j = 1, 2), \tag{4.28}$$

where σ is the interfacial tension, θ is contact angle, and the subscripts nw and w indicate the non-wetting and wetting phases, respectively.

Trapping of the non-wetting phase in the pore doublet model will occur during the imbibition phase when capillary forces dominate over viscous forces [268]. Various attempts have been made to predict the exact conditions at which snap-off occurs [267, 268]. The entrapment of the non-wetting phase is despite the fluid properties, largely dependent on the exact pore geometry [268], and therefore general trapping criteria are challenging to find and there is no consensus reached in the literature. However, the impact of various factors can be predicted by comparing the relative importance of capillary forces to viscous forces. Although the simulations are conducted in 2D, Equations 4.27 and 4.28 are based on 3D theory. These 3D expressions are more commonly used in the literature and provide a better representation of realistic porous media behaviour. Since our analysis focuses on relative trends rather than absolute magnitudes, applying the 3D form allows for more general and transferable insights. In addition, it serves as a check on whether the 2D simulations reproduce the qualitative behaviour expected from 3D systems.

4.4.2 Impact of flow velocities, channel width ratio, channel geometry, and fluid properties

Equations 4.27 and 4.28 indicate that the capillary pressure within each channel is independent of the flow rate (q). In contrast, the viscous pressure drop increases with flow rate. Consequently, at higher flow rates, viscous forces become more dominant relative to capillary forces. Since higher flow rates require a greater overall pressure gradient, this corresponds to higher capillary numbers. Trapping is most likely to occur when capillary forces dominate over viscous forces. This condition is met at low flow rates, which correspond to lower pressure gradients and capillary numbers. Therefore, as the capillary number decreases, the probability of trapping increases.

Equation 4.28 shows that capillary pressure increases as channel width decreases. As a result, very narrow channels exhibit significantly higher capillary pressures. When the width ratio between the larger and smaller channels is greater, the capillary pressure within the narrow channel becomes more dominant within the system, promoting flow through the narrow channel and causing bypassing of the larger channel. Consequently, a higher channel width ratio increases the likelihood of trapping at certain capillary numbers.

As illustrated in Figure 4.4, trapping is highly influenced by local forces that determine whether a snap-off event occurs. At the junction where the two channels reconnect, there is always a localized resistance due to the expansion of the interfacial area. The exact geometry of this junction plays a critical role in determining whether trapping occurs. In wider and more rounded geometries, the interfacial area at the potential snap-off location is larger, which reduces the likelihood of snap-off. Conversely, in sharper or more constricted geometries, the interfacial area is smaller, increasing the probability of trapping.

Equations 4.27 and 4.28 show that fluid properties such as viscosity, interfacial tension, and contact angle influence the balance between viscous and capillary forces. Higher viscosity increases viscous forces, while higher interfacial tension and lower contact angle

increase capillary forces. Based on the fluid properties in Table 4.1, CO_2 shows the strongest dominance of viscous forces over capillary forces due to its high viscosity and low interfacial tension and contact angle, followed by CH_4 and then H_2. As a result, at the imposed same pressure gradients or velocities, CO_2 is most likely to bypass and become trapped, followed by CH_4 and finally H_2. Increasing brine salinity affects both viscosity and interfacial tension. It leads to higher viscosity [173] and also higher interfacial tension [47], which suggests that both viscous and capillary forces may increase. Therefore, the impact is expected to be minimal.

The fluid properties used in this study correspond to conditions at 11 MPa and 40°C. While fluid properties vary with pressure and temperature, particularly for gases, these variations are less pronounced for the liquid-phase brine. At greater depths, the viscosity and density of H_2 would increase slightly, reducing the viscosity and density contrast with brine. However, given the inherently low viscosity and density of H_2 compared to brine, these changes are expected to have a minimal impact on the trapping behaviour in this study. The H_2-brine surface tension is not significantly dependent on pressure, and is expected to decrease with temperature [47], suggesting less pronounced capillary forces in deeper reservoirs. The contact angle is expected to be independent of pressure and temperature [189].

4.5 Results and Discussion

Our results reveal the conditions under which trapping due to bypassing occurs within a pore doublet model. Specifically, we quantify the trapping percentage observed after a drainage-imbibition cycle in cases where trapping occurs, which is summarized in Figure 4.6. The following sections provide a detailed discussion of our simulation results, offering a systematic understanding of the factors influencing trapping within the pore doublet model.

In Section 4.5.1, we examine the impact of capillary numbers, which correlate with flow velocities representing specific injection and production rates. Section 4.5.2 explores the impact of the channel width ratios and pore size distributions in various geometries. In addition, the influence of pore shape is also investigated and discussed in this section. In Section 4.5.3, we discuss the influence of fluid properties on trapping by comparing the behavior of H_2, CH_4, and CO_2.

4.5.1 Impact of Capillary number

Theoretical analysis predicts that larger capillary numbers, corresponding to higher flow velocities, result in a lower probability of trapping. Our results confirm this relationship. Figure 4.5(a) illustrates the initial drainage phase for all tests, where the system is fully saturated with brine, and H_2 is injected from the left. As anticipated, H_2 preferentially flows through the larger channel due to both lower capillary and viscous resistance. During this phase, trapping of H_2 is not expected, so in the remainder of this section, the focus will be on the imbibition phase.

Once H_2 reaches the outlet, the flow is reversed to initiate the imbibition phase, during which brine is injected from the right with varying capillary numbers. Figure 4.5(b) shows the imbibition phase of a test with a capillary number of 4.0×10^{-4}, showing brine flow

through both channels initially. However, the smaller channel exhibits favorable conditions for flow due to the relatively large capillary pressure pulling the brine inward, eventually leading to snap-off in the third frame. Subsequently, brine flows exclusively through the smaller channel, leaving H_2 trapped in the larger channel (fourth frame).

Figure 4.5(c) shows results for a higher capillary number (5.0×10^{-4}), where increased viscous forces decrease the influence of capillary forces. In this case, snap-off is observed in the second frame, but the detached bubble is mobilized again, and eventually, all H_2 is swept from the system.

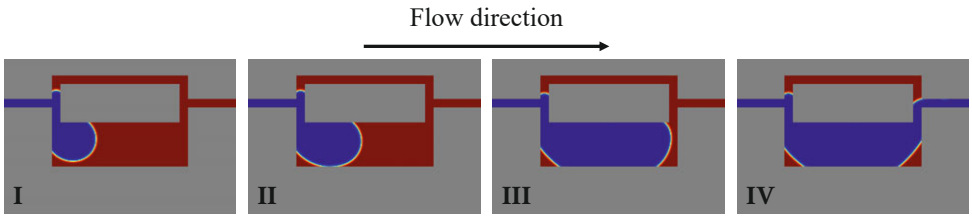

(a) Drainage test with flow from left to right.

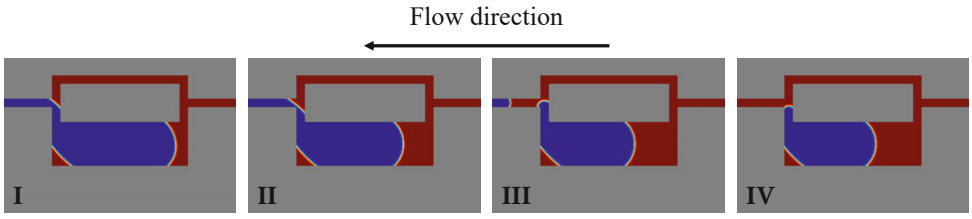

(b) Imbibition test with capillary number of 4.0×10^{-4} with flow from right to left.

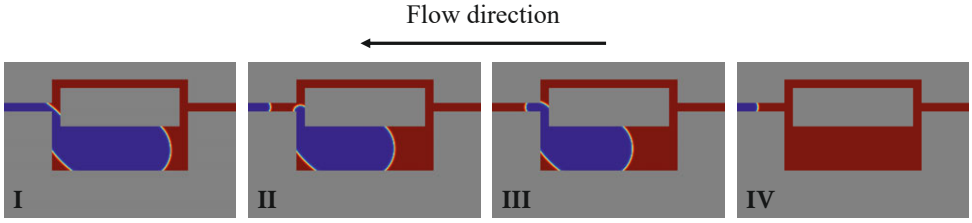

(c) Imbibition test with capillary number of 5.0×10^{-4} with flow from right to left.

Figure 4.5: Frames from drainage (a) and imbibition (b and c) tests. Red represents brine and blue represents H_2. Trapping occurred during imbibition with capillary number 4.0×10^{-4} (b), while it did not occur for a higher capillary number of 5.0×10^{-4} (c).

Figure 4.6 shows the trapping percentages for various tests using a range of capillary numbers for the imbibition phase. As anticipated, there is a certain threshold in capillary numbers for trapping to occur. This "threshold" or "critical capillary number" represents a sharp decrease in trapping percentage with increasing capillary numbers, due to the transition from dominating viscous forces to capillary forces. This sharp decrease in trapping has also been observed on the larger scale in both experiments and numerical

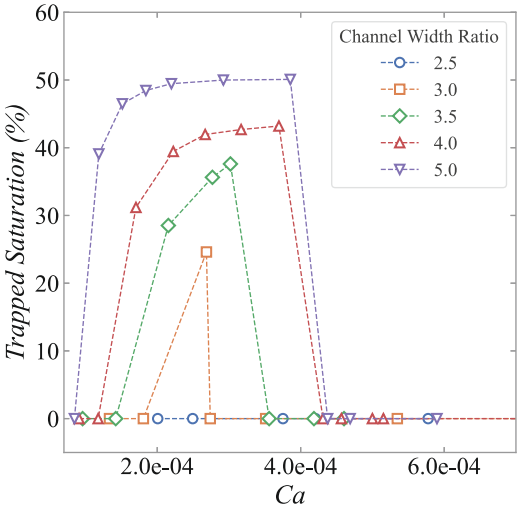

Figure 4.6: Comparison of H_2 trapping percentages after imbibition for various channel width ratio's across capillary numbers in the rectangular pore doublet model.

simulations [271, 318–321]. The exact threshold depends on the geometry of the system, which will be further discussed in the next section. In some of the cases we can also observe a decrease in trapping percentage as capillary numbers decrease. This will also be further discussed in the next section.

4.5.2 Impact of channel width ratio and pore size distributions in various geometries

Figure 4.7 illustrates four frames from three different test cases with channel width ratios of 3, 4, and 5, shown in panels (a), (b), and (c), respectively. All test cases shown in this figure were conducted at a similar capillary number of 4×10^{-4}. It can be observed that trapping did not occur in the test case where the channel width ratio was 3, whereas trapping was observed in the test cases with larger channel width ratios of 4 and 5.

These results align with theoretical predictions, which suggest that a larger difference in channel width enhances the dominance of capillary forces over viscous forces. This increased influence of capillary forces leads to the trapping phenomenon observed in cases with higher channel width ratios. Consistent with this observation, Figure 4.6 demonstrates that larger channel width ratios correspond to a higher threshold for trapping.

Furthermore, larger width ratios result in higher trapping percentages. This can be attributed to the increased dominance of capillary forces in systems with greater channel width disparities. While trapping can still occur in cases with smaller channel width ratios, the flow of brine through the upper channel is slower relative to the flow in the larger channel compared to cases with larger ratios. In these instances with larger ratio, snap-off occurs more quickly and as a result, the brine does not advance as far in the lower channel, resulting in a higher trapping percentage.

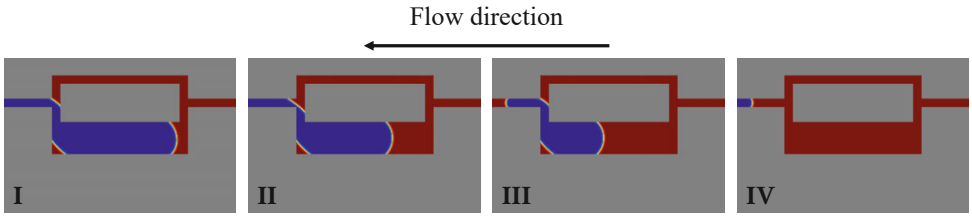

(a) Channel width ratio = 3

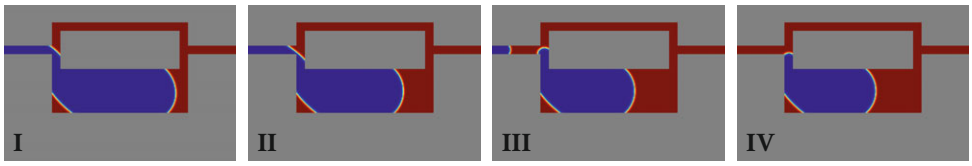

(b) Channel width ratio = 4

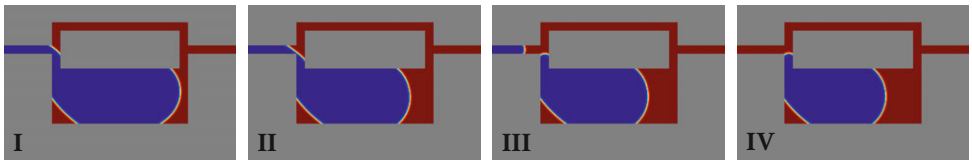

(c) Channel width ratio = 5

Figure 4.7: Frames from imbibition tests with channel width ratios of 3 (a), 4 (b), and 5 (c) with capillary number of 4×10^{-4}. Red represents brine and blue represents H_2. The frames taken at the moment when (I) the wetting phase enters the large channel (II) snap-off is about to happen (III) snap-off just happened (IV) steady-state is reached.

Figure 4.6 indicates that for smaller channel width ratios, trapping percentages decrease as capillary numbers drop below the trapping threshold. Interestingly, no trapping is observed for the lowest capillary numbers, which appears counterintuitive. To understand this behaviour, it is essential to examine the geometry and the moment when snap-off nearly occurs, as illustrated in Figure 4.8, this point in the simulation corresponds to point B in Figure 4.4.

At low capillary numbers, capillary forces dominate, resulting in preferential flow through the upper channel. However, when the fluid interface reaches the junction where the two channels merge into the outlet channel (point B in Figure 4.4), the interface temporarily widens as though the channel abruptly expands. This widening reduces the local capillary pressure, while the narrower channel still experiences relatively high viscous forces. Consequently, despite the general advantage of the upper channel, this temporary reduction in capillary pressure creates a local disadvantage, as also explained in the theoretical analysis (Section 4.4). When flow velocities are higher, the increased kinetic energy helps to overcome this local disadvantage, allowing snap-off to occur. Conversely, at very low velocities (low capillary numbers), this disadvantage significantly delays snap-off. In some cases, the delay is so pronounced that the flow through the lower, wider channel

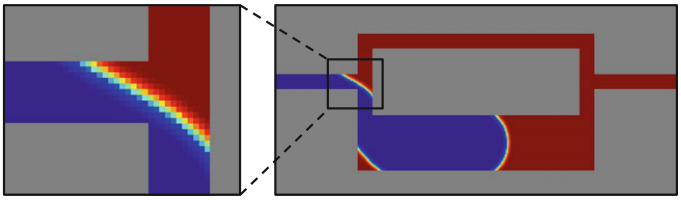

Figure 4.8: Frame of the moment where snap-off nearly occurs, leading to trapping

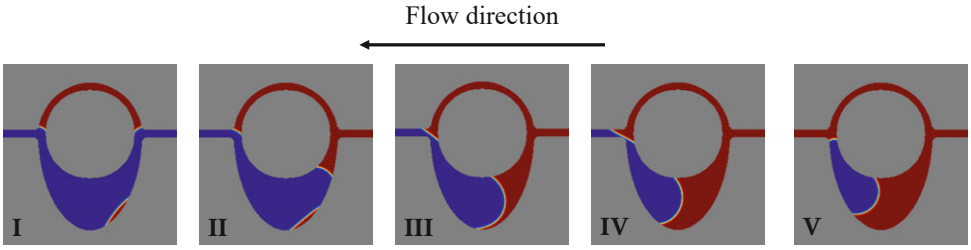

Figure 4.9: Frames from imbibition test with the rounded pore doublet with a channel width ratio (d_2/d_1) of 5 and capillary number of 3.5×10^{-4}. Red represents brine and blue represents H_2.

becomes dominant, and snap-off does not occur at all.

This analysis highlights the critical role of exact geometry in determining the trapping threshold. To further investigate, similar simulations were conducted using a rounded pore doublet model, as described in Figure 4.3 (left), with varying channel width ratios. Trapping was also observed in this geometry under specific conditions, an example of which is presented in Figure 4.9.

The results are summarized in Figure 4.10. In this geometry, trapping occurs only for channel width ratios of 5 and higher, with trapping percentages ranging from 0 % to 35 %. When compared to the results obtained from the rectangular pore doublet model (Figure 4.6), a similar trend can be observed. As the channel width ratio increases, both the trapping percentages and the capillary number thresholds for trapping increase. However, the absolute trapping percentages and thresholds are lower for the rounded pore doublet model at specific channel width ratios.

These findings suggest that the rectangular structure enhances trapping compared to the rounded structure, while maintaining the same general relationships between channel width ratio, trapping percentage, and capillary number thresholds. This difference can also be understood in terms of the pore throat aspect ratio, defined as the ratio between the wider junction area (acting as a pore) and the narrower connecting channels (throats), as illustrated in Figure 4.11. In the rounded geometry, the pore radius is larger than in the rectangular geometry ($r'_{\text{pore}} > r_{\text{pore}}$), effectively increasing the aspect ratio. Consequently, the interface must extend further before reaching the opposite side of the channel ($L' > L$), which lowers the local capillary pressure. As a result, snap-off and the resulting trapping are delayed or less likely to occur. Overall, the smoother and more open junction in the rounded geometry contributes to reduced trapping under comparable conditions.

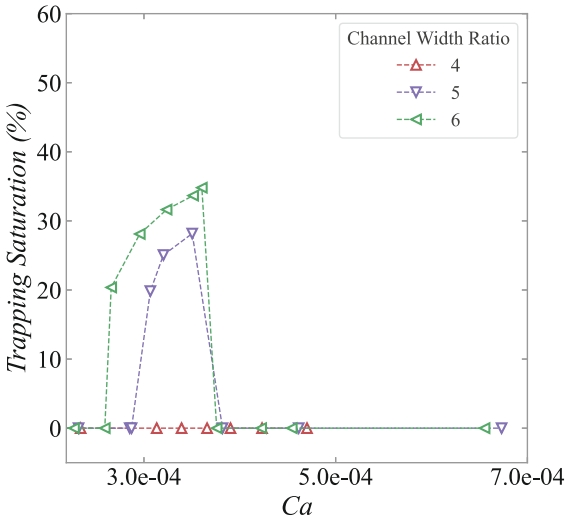

Figure 4.10: Comparison of H_2 trapping percentages within the rounded pore doublet model for various channel width ratio's across capillary numbers.

Our observations are consistent with the recent analytical work of Shan *et al.* [269], who derived an analytical solution for immiscible displacement in a pore doublet. They demonstrated that the displacement process is governed by a critical capillary number, which depends on both the viscosity ratio and the channel radius ratio. When the system operates below this critical number, preferential imbibition occurs in the narrow channel, leading to trapping in the wider channel. At higher capillary numbers, viscous forces dominate and trapping is reduced. These theoretical predictions align well with our LBM results, which show that increasing the channel width ratio promotes bypassing and enhances trapping at low capillary numbers.

4.5.3 Impact of gas type

Figure 4.12 presents frames from an imbibition test conducted at a capillary number of 4×10^{-4} and a channel width ratio of 4. The top row (a) shows frames from a test using H_2 properties for the non-wetting phase, with corresponding tests for CH_4 and CO_2 properties shown in panels (b) and (c), respectively. For this capillary number, trapping is observed for both H_2 and CH_4, while for CO_2 no trapping is observed. It can be observed that the behaviour of H_2 and CH_4 is quite similar, and similar gas saturations remain trapped, which is already expected due to their similar thermophysical properties.

Figure 4.13 shows the trapped saturations of H_2, CH_4, and CO_2 as a function of the capillary number. Among the three gases, H_2 exhibits the lowest capillary trapping threshold at 3.8×10^{-4}, followed by CH_4 at 4.1×10^{-4}, and CO_2 with a significantly higher threshold of 1.1×10^{-3}. The capillary number represents the ratio of viscous to capillary forces, which governs trapping through bypassing. However, it does not include the viscosity ratio between the gas and liquid phases. Our results show a clear influence of viscosity ratio

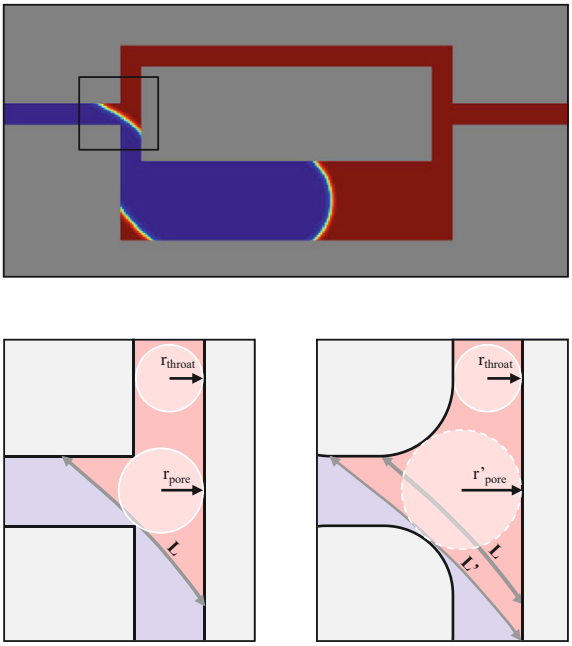

Figure 4.11: Illustration of the influence of pore throat aspect ratio on capillary trapping. In the rectangular geometry (left), sharp transitions between throat and pore result in lower aspect ratios ($r_{\text{pore}}/r_{\text{throat}}$) and less reduced local capillary pressure, promoting trapping. In contrast, the rounded geometry (right) features smoother transitions and a higher aspect ratio ($r'_{\text{pore}}/r_{\text{throat}}$), as well as a lower capillary pressure due to the longer interface L', reducing the likelihood of trapping under comparable conditions.

on the trapping behaviour. H_2 has the lowest gas-to-liquid viscosity ratio (0.012), CH_4 is slightly higher (0.018), and CO_2 is much higher (0.067), which aligns with the observed trapping thresholds. Since only the gas viscosity is used in our capillary number definition, and not the liquid viscosity, the effect of gas viscosity is overestimated in systems that are not fully gas-saturated. This results in lower apparent capillary thresholds for gases with lower viscosities.

Based on our results, H_2 and CH_4 exhibit similar trapping behaviour. The capillary number alone does not fully capture the dynamics of two-phase flow, particularly when it includes only the viscosity of the gas phase. However, examining the inlet velocities V_{inlet} at which capillary trapping begins reveals that H_2 and CH_4 reach their trapping thresholds at higher velocities than CO_2. This suggests that, at comparable production rates, H_2 and CH_4 are more likely to be trapped due to bypassing, while CO_2 may remain more mobile under the same conditions due to its higher viscosity and therefore stronger viscous forces.

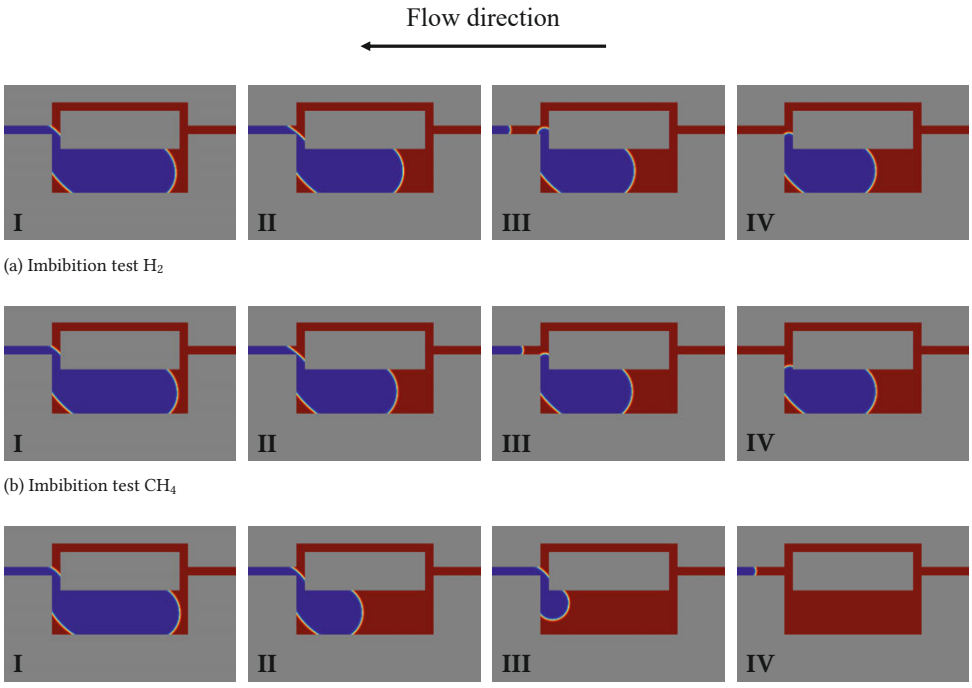

(a) Imbibition test H_2

(b) Imbibition test CH_4

(c) Imbibition test CO_2

Figure 4.12: Frames from imbibition tests with H_2 (a), CH_4 (b), and CO_2 (c) with capillary number of 4×10^{-4}. Red represents brine and blue represents the gas phase. Frames are taken at the moment when (I) the wetting phase enters the large channel (II) snap-off is about to happen (III) snap-off just happened (IV) steady-state is reached.

4.5.4 Application to UHS systems

The findings of this study are relevant to underground hydrogen storage (UHS), where understanding and predicting trapping mechanisms is critical for optimizing storage effi-

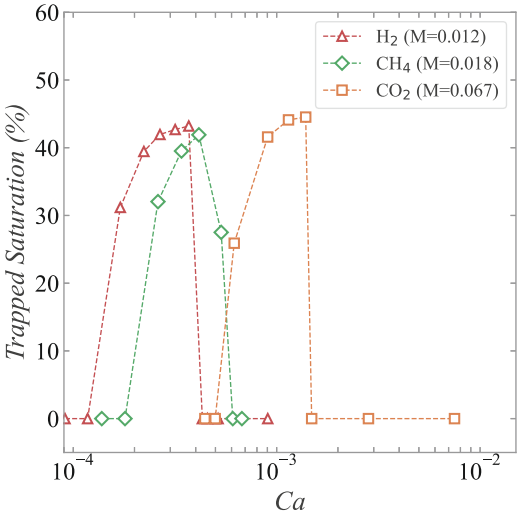

Figure 4.13: Comparison of trapping percentages for H_2, CO_2, and CH_4 across capillary numbers. A channel width ratio of 4, and the rectangular pore doublet were used in the numerical simulations.

ciency and minimizing losses. While the geometries used in this study do not replicate real pore structures, simplified geometries were intentionally chosen to develop a fundamental understanding of capillary trapping caused by bypassing and to identify trends applicable to UHS.

Our results show that trapping efficiency is strongly influenced by the distribution of pore sizes. A higher channel width ratio, representing a broader pore size distribution in rock formations, significantly enhances trapping due to bypassing. This indicates that reservoirs with wider pore size distributions are likely to immobilize greater amounts of hydrogen through capillary trapping. This will reduce overall efficiency, particularly during initial storage cycles, as some of the injected hydrogen may remain trapped and unrecoverable.

Additionally, pore geometry was found to have a significant influence on the extent of trapping. Trapping due to bypassing is less likely to occur in rounded pores compared to rectangular shapes with sharp corners, and the trapping percentages are correspondingly lower in geometries with rounded corners. This suggests that selecting a rock type with well-rounded grains, rather than angular grains with sharp edges and corners, could reduce trapping and improve storage efficiency.

The observed dependence of trapping on the capillary number highlights the critical role of flow conditions during withdrawal phases. Lower capillary numbers, associated with slower flow rates, were found to increase trapping within our pore geometry. Extrapolating this to larger UHS systems suggests that producing H_2 from the reservoir at higher flow rates would enhance efficiency by reducing the amount of residually trapped H_2.

Interestingly, the findings of Yu *et al.* [261] suggest that higher flow rates can promote trapping due to dead-end bypassing. However, the broader consensus at the core scale

indicates that the total amount of capillary-trapped non-wetting phase after imbibition generally increases with decreasing capillary number [320]. This conclusion is supported by both numerical and experimental studies [271, 318, 319, 321]. In the context of H_2, it is also observed in core flood experiments that injection of brine at higher flow rates reduced capillary trapping and increased H_2 recovery [290]. These results reinforce our conclusion that higher production rates for H_2 extraction are likely to reduce residual trapping percentages.

The geometries used in our study were intentionally simplified to investigate the fundamental processes of capillary trapping due to bypassing. This phenomenon is inherently complex and highly sensitive to specific pore geometries and flow regimes. While these simplified geometries are essential for understanding the mechanisms driving certain processes observed at larger scales, they are not directly representative of real-world UHS scenarios.

To address these limitations, future research should focus on integrating these pore-scale insights into larger-scale reservoir models or conducting more realistic pore-scale simulations. Such efforts will facilitate more accurate predictions of trapping behaviour and storage efficiency under conditions that better reflect practical applications. Moreover, trapping due to bypassing represents only one of the two primary capillary trapping mechanisms. To develop a more comprehensive understanding of the total amount of capillary trapping, future studies should also investigate the dynamics of trapping caused by snap-off. This dual focus will provide a more complete perspective on the factors influencing trapping efficiency in subsurface systems.

In addition to UHS systems, the trapping behaviour analyzed in this study may also have implications for natural hydrogen extraction and in situ hydrogen generation [322, 323]. These promising technologies involve subsurface environments in which hydrogen may occupy different pore structures and regions compared to UHS, potentially making recovery more challenging. Understanding the mechanisms of bypassing and trapping can therefore provide valuable insight into efficiency and recoverability in such settings.

4.6 Conclusions

This study aimed to provide a deeper understanding of how pore geometry and flow rate influence the residual trapping of H_2 by bypassing and to connect these mechanisms to the pore size distributions of rocks. Pore-scale simulations were conducted using the lattice Boltzmann method (LBM) across a variety of geometries, including the pore doublet model, to investigate the impact of (a) channel width ratio, (b) pore shape, (c) capillary number and flow velocities, and (d) fluid properties, through a comparison of the trapping behaviour of H_2 with that of CH_4 and CO_2, on residual trapping by bypassing, which is a key trapping mechanism. Simulation results were supported by a theoretical analysis. The following key conclusions were drawn:

- Residual trapping due to bypassing predominantly occurs at low capillary numbers, emphasizing the role of capillary forces in controlling trapping mechanisms. These results suggest that producing H_2 at higher flow rates will result in less residual trapping, which is in line with experimental findings [290].

- Two types of geometries were studied: rectangular pore doublets and rounded pore doublets. A clear relationship between channel width ratio and trapping percentage was observed, with higher channel width ratios leading to increased trapping. This finding indicates that rocks with a relatively narrow distribution of channel widths are more favorable for UHS, as less H_2 will get trapped due to bypassing. While the use of simplified geometries enabled us to isolate and understand key physical mechanisms, future studies involving more realistic pore structures are needed to confirm and extend these findings.
- The likelihood of trapping is primarily governed by the balance between capillary and viscous forces, making it a useful predictor of the relative extent of trapping in a given system. However, local pore geometry plays a crucial role in determining whether snap-off occurs. Rounded pore geometries reduce trapping, while angular geometries enhance snap-off, leading to increased trapping due to bypassing. Consequently, rocks composed of well-rounded grains are more effective for UHS, whereas angular-grained rocks are less favorable for UHS when considering this trapping mechanism.
- In addition to the capillary number, the mobility ratio plays a key role in predicting residual trapping. H_2 and CH_4 exhibit similar trapping thresholds in terms of capillary number due to their comparable mobility ratios, while CO_2 behaves differently. At similar production rates, H_2 and CH_4 are more prone to trapping by bypassing, whereas CO_2, with its higher viscosity and stronger viscous forces, tends to remain more mobile under the same conditions.

These findings provide valuable insights into the conditions and rock properties that enhance H_2 trapping in subsurface reservoirs, with implications for optimizing underground hydrogen storage strategies.

III

Site selection

5

A framework for efficient Field Elimination and Ranking

Underground hydrogen storage in porous media is promising for large-scale energy storage. However, its technical and financial effectiveness heavily depends on a reliable site selection strategy. In this chapter, we critically assess the available literature across disciplines to identify the most influential criteria for reliable site selection. Drawing from this evaluation, we propose a systematic, multidisciplinary framework for early-stage reservoir screening, integrating key criteria from reservoir performance, geomechanics and containment, location and techno-economics, and bio-geochemistry. Our framework allows for rapid identification and ranking of the most suitable reservoirs by proposing 11 elimination and 15 screening criteria. The presented framework consists of practically applicable and scientifically grounded criteria to support consistent, early-stage decision based on readily available data, while allowing for detailed site-specific analysis in later project development phases. By unifying diverse disciplinary insights into a structured methodology, this study contributes to more informed, inclusive and effective site selection.

This chapter was published in Energy & Fuels **Vol. 39(41)**, (2025) [324].

5.1 Introduction

As the global energy transition accelerates, hydrogen is considered as an important energy carrier, in particular for long-term energy storage, due to its high gravimetric energy density and clean combustion products [4, 6–8]. Underground Hydrogen Storage (UHS) in geological formations, such as salt caverns, depleted reservoirs, and aquifers, is promising for large-scale, long-term energy storage to balance supply and demand fluctuations [9–12]. Depleted gas reservoirs offer significant potential due to their high capacity [16–18]. However, selecting a suitable reservoir is a crucial step in enabling a safe and efficient storage implementation project [46]. This selection process must account for a range of factors, which are multidisciplinary by nature, including reservoir performance (e.g., injectivity and deliverability), geomechanical stability, containment integrity, bio-geochemical interactions, and techno-economic viability. A comprehensive site ranking and selection framework, which is developed based on a critical and inclusive assessment of these dimensions, is essential to mitigate risks and maximize the operational efficiency.

While Underground Gas Storage (UGS) has been widely utilized for several decades, underground hydrogen storage remains a relatively new technology. Despite the long history of gas storage, publicly available research on the site selection criteria for underground gas storage fields remains limited [325–327]. In contrast, site selection for CO_2 storage has been quite extensively investigated, with numerous studies providing comprehensive screening criteria and assessment methodologies [327–336]. Site selection of Underground Hydrogen Storage has been gaining more attention in the recent years. Numerous studies describe workflows for selecting suitable UHS fields [46, 337–347].

Many of these studies employ Multi-Criteria Decision-Making (MCDM) techniques, such as the Analytic Hierarchy Process, to evaluate a range of site selection criteria and their relative importance. Expert judgment plays a crucial role in this context, especially given the diverse and often non-comparable nature of the factors involved. However, to ensure that site selection decisions are grounded in robust evidence, it is important to complement expert-based methods with quantitative techniques such as sensitivity analysis through reservoir modeling. Sensitivity analysis systematically evaluates how variations in key geological and operational parameters impact storage performance, leading to more reliable and evidence-based site selection. Despite its value, only a few studies have applied this approach for site selection [338, 343, 348]. Okoroafor et al. [338] identified critical parameters for hydrogen storage in depleted gas fields, while Sekar et al. [343] extended this to saline aquifers, proposing elimination and ranking criteria. Chen et al. [348] developed a machine learning–based reduced-order model trained on high-fidelity simulations to perform sensitivity analysis and identify optimal saline aquifers in the U.S. Similarly, Malki et al. [344] introduced OPERATE–H2, a tool that integrates reduced-order models and sensitivity analyses to assess hydrogen storage performance and support site selection based on geologic and operational factors. Although Wang et al. [18] and Mwakipunda et al. [349] addressed site selection as part of a broader review, their treatment of this topic is limited in detail due to the wider scope of their studies.

In addition to the studies explicitly addressing site selection, numerous other investigations offer valuable insights by focusing on specific aspects of UHS. These studies often employ sensitivity analyses or explore individual parameters or aspects such as geological heterogeneity [350], microbiological activity [27, 28] or residual trapping. By

concentrating on isolated factors, they provide a more detailed understanding of the underlying physical and operational processes, thereby contributing critical knowledge that complements broader site selection frameworks. Such focused analyses enhance the overall understanding of the UHS system behavior and can inform the development of more robust, science-based selection criteria.

Indeed, as more pilot projects for UHS are initiated worldwide, a comprehensive and scientifically grounded approach to site selection is becoming increasingly important. However, no comprehensive review currently exists that specifically focuses on the UHS site selection, the very first crucial step in making any project successful. And, to the best of the authors' knowledge, a scientifically grounded framework that integrates insights from all relevant disciplines into quantifiable and practically applicable criteria for site selection is also missing in the literature. This review and outlook study addresses such a significant knowledge gap by presenting a systematic, multidisciplinary approach for reliable site selection for UHS in porous media. Here, we focus on the most influential and practically applicable criteria to enable rapid and effective field elimination and ranking among many available options. The framework draws directly from established findings in the literature, including results from sensitivity analyses and domain-specific studies, to ensure both scientific rigor as well as practical applicability.

We begin by reviewing and evaluating existing studies on site selection for UHS, identifying current practices and their limitations (Section 5.2). To provide context, we then compare site selection approaches across UHS, underground gas storage (UGS), and carbon capture and storage (CCS), highlighting differences in site selection methodologies across these applications (Section 5.3). Building on these insights, we introduce a framework setup specifically developed for UHS (Section 5.4). Its structure is organized around four main categories: Reservoir Performance, Bio-Geochemistry, Geomechanical Risks and Containment, and Location and Techno-Economics. Each category is analyzed to identify the most critical factors influencing site suitability (Sections 5.5 - 5.8). These elements are then integrated into a comprehensive framework (Section 5.9), followed by a discussion of key challenges and perspectives (Section 5.10), and a conclusion (Section 5.11).

5.2 Site Selection Strategies: Overview and Assessment

Site selection for Underground Hydrogen Storage has received increasing attention in recent literature [46, 337–343, 345–348, 351–355]. Numerous studies have applied site selection methods to specific regions, including Japan, Germany, the UK, USA, and Poland [46, 340, 342, 343, 345, 348, 354, 355].

Site selection is typically based on predefined criteria, which play a crucial role in determining suitable locations. Some studies propose new, UHS application specific, site selection criteria [338, 343, 351, 354], while others derive their criteria from the existing literature [337, 340, 342, 347, 352, 354, 355], sensitivity analyses via reservoir model simulations [338, 343, 348], or even expert judgments. However, in some cases, the rationale behind the employed criteria is not explicitly stated, nor justified [341, 351, 353]. Notably, very few studies provide a solid scientific basis for their proposed site selection criteria.

Table 5.1 provides an overview of the site selection criteria identified in UHS site selection studies. We have grouped the criteria into four categories; however, it is important

to note that some criteria influence multiple categories. Most existing studies place a strong emphasis on reservoir performance, while bio-geochemistry and geomechanical aspects receive comparatively less attention, and techno-economic factors, despite being very important in realization of the projects, are the least frequently addressed topics. Striking a balance between these areas remains a key challenge, as many studies consider only a subset of the criteria, resulting in an incomplete perspective on site suitability. Table 5.1 shows a wide range of criteria, and while some of the criteria, such as depth, permeability, and porosity, are relatively intuitive to evaluate, many others, e.g., cushion gas requirement, initial capital investment, and local culture embedding, most likely require additional analysis, which can become very time-consuming and challenging specially as they can be beyond the technical aspects (including social sciences).

Table 5.1: Overview of all criteria used in literature site selection studies

Reservoir Performance	Location and Techno-Economics
• Pore volume/Storage capacity[46, 337–340, 346, 347, 351] • Depth [46, 337–341, 343, 347, 351, 352, 354] • Pressure [338, 339, 343, 347, 351, 352] • Permeability [337–341, 343, 347, 351, 352, 354] • Porosity [337–341, 343, 347, 351, 352, 354] • Permeability anisotropy [338, 339] • Permeability heterogeneity [338, 339] • Closure/spill point [341, 351] • Reservoir dip [338, 339, 343] • Reservoir structure [337, 340, 343, 351, 352] • Geothermal gradient [338, 343] • Stage of exploration [46] • Reservoir type (gas/oil/aquifer) [46, 338, 346, 351] • Area [337, 341, 351] • Thickness [337, 338, 341, 343, 347, 351, 352, 354] • Vertical closure [352] • Flow capacity [340, 346, 354] • Pressure buildup [354] • Column height [354] • (Vertical) Net gross [340, 341] • Max. H_2 well deliverability rate [340]	• Labour [337] • Proximity to suppliers and infrastructure [337, 340, 346, 347] • Infrastructure availability [337, 346] • Storage cost [337, 347] • Initial investment [337, 347] • Regional risks [337, 347] • Legal restrictions [337, 346, 351] • Social acceptance [337, 346, 351] • Job creation [337] • Local culture [337] • Cushion gas requirement [339, 340] • Facilities, pipelines, ports [339] • Sensitive areas, environment [339] • Offshore/onshore [340, 346] • Spatial planning [341]
Geomechanical Risks and Containment	**Bio-Geochemistry**
• Overburden rock lithology [46, 339, 352] • Faults in proximity, compartmentalisation [338, 339, 341, 343, 346, 351] • Earthquakes / Seismicity / tectonic activity [46, 337–339, 341, 343, 346, 351] • Caprock permeability [337, 346] • Cap rock thickness [338, 339, 341, 343, 352] • Secondary confining units [338, 343] • Overlying aquifers [346, 351] • Faults in overburden [341, 346] • Seal lithology [341] • Subsidence [351] • Proven seal [346, 351] • Well density [346]	• Rock types and mineralogy [339, 343, 346, 351, 352, 354] • Knowledge of depositional environment [351] • Temperature [343, 346, 351, 354] • Pressure [338, 339, 343, 351] • Fluid characteristics, salinity, pH [339, 343, 346, 351, 354] • Presence of microorganisms [339]

Moreover, the way these criteria are applied in the site selection process in the literature varies significantly. In our view, both screening and ranking are essential steps in the site selection process. However, screening, the elimination of fields that do not meet essential criteria, is not always conducted in the literature, which may lead to the selection of fields that lack essential characteristics. A structured and systematic approach that incorporates both phases of screening and ranking is necessary for reliable site selection.

An effective way to prioritize and weigh the various criteria is by using Multi-Criteria Decision-Making (MCDM) tools [46, 337, 340–342, 347, 353]. These tools help to reduce subjectivity in site selection by ensuring a structured decision-making process and allowing for the comparison of criteria of different natures. Commonly used MCDM methods include the Analytic Hierarchy Process (AHP), the fuzzy Delphi method, and the Preference Ranking Organization Method for Enrichment Evaluations (PROMETHEE). While MCDM methods provide valuable insights, expert judgment remains integral to the process. This is particularly important given the wide range of factors involved, which are often difficult to directly compare. However, expert assessments can be inherently subjective, and the complexity of some MCDM methods can make the process of selecting a field more time-demanding.

Existing methods offer valuable insights, but a more systematic approach that integrates all important aspects is necessary for optimal UHS site selection. Additionally, scientific validation and quantification of site selection criteria are imperative. Lastly, we focus on providing only the most influential site selection criteria, to keep the method fast, efficient, and understandable for a wider public.

In our view, the following conditions are crucial for a robust site selection method: (a) Quantified site selection criteria based on scientific research focusing only on the most influential criteria, (b) A structured approach incorporating both screening and ranking phases, (c) Consideration of all important aspects including: Reservoir performance, Biogeochemistry, Geomechanical risks and containment, and Location and techno-economics.

5.3 Site selection of UHS vs UGS and CCS

Although large-scale Underground Hydrogen Storage (UHS) is not yet widely implemented, the established practices of Underground Gas Storage (UGS) and Carbon Capture and Storage (CCS) offer relevant insights [4]. For example, decades of storing methane in the subsurface have equipped us with a good understanding of risks associated with cyclic loading. However, key differences in gas properties must be considered when selecting suitable UHS sites.

Hydrogen differs significantly from methane (CH_4) and carbon dioxide (CO_2) in density and viscosity. Under the conditions of 40 °C and 110 bar, as shown in Table 5.2, H_2 is approximately 10 times lighter than CH_4 and 45 times lighter than CO_2, with viscosity also lower by factors of 1.5 and 6, respectively. These differences strongly affect the dimensionless gravity number (Γ), which characterizes the balance between buoyancy and viscous forces [356, 357], i.e.,

$$\Gamma = \frac{2\pi\Delta\rho g k H^2}{Q\mu_{brine}}. \tag{5.1}$$

Here, $\Delta\rho$ is the density difference between the gas and the brine, g is the gravitational

acceleration, k is the permeability, H is the reservoir thickness, Q is the injection rate, and μ_{brine} is the dynamic viscosity of the injected brine. As indicated in Table 5.2, Γ is about 7 % higher for UHS compared to UGS, and roughly 3 times higher than for CCS, signifying stronger buoyancy-driven flow in UHS, especially in comparison to CCS[25]. This effect can be used to keep H_2 segregated from other gases, but it also causes a risk for gravity overriding which should be taken into account [358–360]. While hydrogen's low viscosity and therefore high mobility enhance injectivity, it also increases the risk of unstable (fingering) displacement during injection, which can be assessed using the mobility ratio (M) [361], defined as

$$M = \frac{k_{r\text{gas}}/\mu_{\text{gas}}}{k_{r\text{brine}}/\mu_{\text{brine}}}, \tag{5.2}$$

where $k_{r\text{gas}}$ and $k_{r\text{brine}}$ are the relative permeabilities of the gas and the brine, and μ_{gas} and μ_{brine} are the dynamic viscosities of the gas and the brine. A higher mobility ratio implies unfavorable displacement of brine by the mobile gas. As shown in Table 5.2, UHS exhibits a higher mobility ratio compared to UGS and CCS (assuming equal relative permeability values for the three gases), which indeed increases the likelihood of viscous fingering [358–360].

Potential leakage through caprock is often raised due to hydrogen's low density, which creates upward buoyant force against the sealing layer. However, despite the lower density, H_2 exhibits higher interfacial tension with brine compared to CH_4 and CO_2, resulting in a higher capillary entry pressure for H_2, which improves the sealing effectiveness of the caprock [360]. This can be assessed using the Bond number (N_B), representing the ratio of buoyancy to capillary forces [362–364], i.e.,

$$N_B = \frac{\Delta\rho g d^2}{\sigma}, \tag{5.3}$$

where $\Delta\rho$ is the density difference between brine and gas, g is the gravitational acceleration, d is the representative length scale, and σ is the interfacial tension. The Bond number is very similar for hydrogen and methane (UHS and UGS) [365], suggesting a similar risk of leakage through the caprock. However, besides interfacial tension, the contact angle also influences capillary entry pressure, with lower contact angles leading to higher entry pressures. Unlike interfacial tension, it depends on fluid–fluid and fluid–solid interactions, including rock type and composition. This makes general comparisons complex, as caprock properties differ between systems and are therefore not included in this section. However, contact angles on shale, a common sealing rock type, are generally lowest for H_2/brine, higher for CH_4/brine, and highest for CO_2/brine [366]. Lower contact angles increase capillary entry pressure, indicating that the contact angle in UHS may slightly enhance sealing potential compared to UGS and CCS.

As shown in Table 5.2, Bond numbers vary by less than 10% across UHS, UGS, and CCS, indicating similar capillary sealing effectiveness. A similar conclusion was reached by Hashemi et al. [365] for comparing H_2 and CH_4 contact angles.

In contrast to UGS and CCS, gas purity is a critical consideration in underground hydrogen storage. As a result, mixing between hydrogen and in-situ or cushion gases

Table 5.2: Comparison of fluid properties and dimensionless numbers for underground storage systems. Thermophysical properties are specific to the gas under reservoir conditions (40°C, 110 bar). Dimensionless numbers are system-scaled and are normalized relative to underground hydrogen storage. A brine density of 1066 kg/m^3[174] and viscosity of 788 μPa s [173] were assumed to calculate the dimensionless numbers.[47, 308–310]

Parameter	**H_2/UHS**	**CH_4/UGS**	**CO_2/CCS**
Thermophysical properties of the gas			
Density [kg/m^3]	8.0	78	6.8×10^2
Viscosity [µPa s]	9.3	14	54
Interfacial tension with brine [mN/m]	66	58	39
Dimensionless numbers (normalized to UHS)			
Mobility ratio	1.0	0.67	0.18
Gravity number (Γ)	1.0	0.93	0.36
Bond number (N_B)	1.0	0.95	0.90

becomes a major concern, as it can significantly compromise hydrogen quality. Site-specific factors that influence gas mixing, such as reservoir heterogeneity and permeability contrasts, should therefore be carefully evaluated during the site selection process.

Furthermore, unlike natural gas in UGS, hydrogen will change the chemical equilibrium of the subsurface (reactive) environment. This reactivity can lead to geochemical interactions with minerals and formation fluids, potentially impacting both purity and storage efficiency [11]. In addition, hydrogen is a universal energy carrier and acts as an electron donor for subsurface microbial communities, which may further affect gas composition and system performance through microbial consumption or transformation of hydrogen, as explained by Dopffel et al. [27].

5.4 Framework setup

In this study, a framework is developed for the rapid site selection of Underground Hydrogen Storage in porous reservoirs. Building upon the work of Callas et al. [328], the framework consists of three stages. A summary of these stages is presented in Figure 5.1.

In *Stage 1: Site Elimination*, sites are removed from consideration based on essential site selection criteria. These criteria consist of disqualifying thresholds, meaning any site that fails to meet any of these thresholds is eliminated. This stage relies on readily available data.

In *Stage 2: Site Ranking*, the remaining sites are evaluated further. Sites are ranked according to a set of site selection criteria, some of which overlap with those from Stage 1. However, in this stage, each site is assigned a score based on these criteria, and a weight is applied to each factor.

Finally, in *Stage 3: Site Selection*, the top-ranked sites from Stage 2 are subjected to a detailed assessment based on dynamic simulations to determine their performance efficiency. However, in this study, we focus on Stages 1 and 2, as Stage 3 can vary significantly depending on the country and specific storage demands.

As explained previously, site selection criteria are used in both Stage 1 and Stage 2. Underground hydrogen storage is a multidisciplinary field, involving factors from various areas of expertise. Inspired by Callas et al. [328], we adapted the categorization of site

selection criteria into four main groups: Bio-Geochemistry, Geomechanics & containment, Location & Techno-economics, and Reservoir Performance.

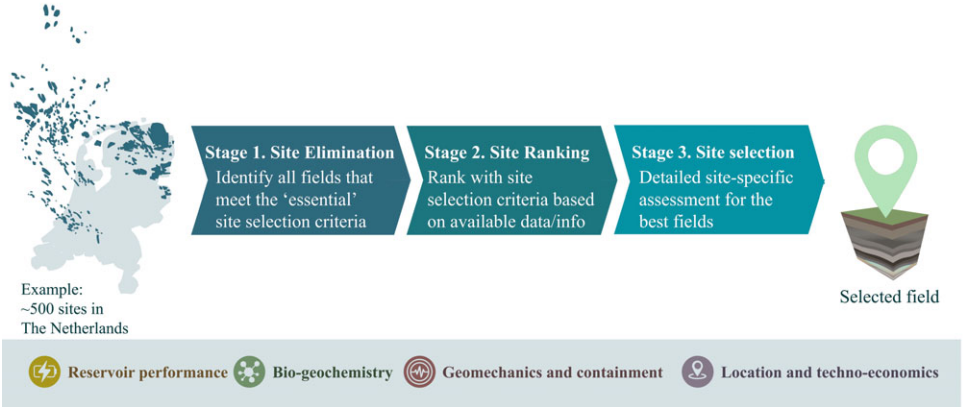

Figure 5.1: Overview of the multiscale framework for selecting optimal porous reservoirs for Underground Hydrogen Storage, inspired by Callas et al. [328]. The framework consists of three sequential stages: Site elimination, site ranking, and site selection. At each stage, site selection is guided by criteria which are subdivided into four categories: Bio-geochemistry, reservoir performance, Geomechanics and containment, and location and techno-economics. For illustration, the figure includes a map of the Netherlands showing its hydrocarbon fields (data with permission from NLOG.nl [32]), representing a typical group of reservoirs used for site selection.

5.5 Reservoir performance

Reservoir performance is a central consideration in site selection for underground hydrogen storage. In this study, we define reservoir performance as the combination of geological characteristics, reservoir architecture, and operational conditions that influence the efficiency and feasibility of hydrogen storage. First, we will introduce the key considerations and risks, followed by an assessment of how specific site selection criteria influence these factors.

5.5.1 Key considerations and risks

As in other subsurface gas storage applications, injectivity and storage capacity are primary parameters. Injectivity, defined as the rate at which hydrogen can be injected per unit pressure drop [333], must be sufficient to meet operational demands without exceeding pressure constraints. Since UHS is a cyclic process, both injectivity and productivity should be considered. However, as the two terms describe similar concepts, they are used interchangeably in this paper.

Due to hydrogen's unique thermophysical properties, specific risks such as gravity override, viscous fingering, segregation, and upconing in saline aquifers must be considered. These processes, along with gas mixing and residual trapping, can significantly affect storage performance. Although solubility [11, 48, 367] and diffusion [48, 358, 368, 369] effects are minor (typically below 1%) and thus excluded from this study, other transport-related phenomena remain central to the operational performance.

The objective of identifying optimal site selection parameters is to find reservoir characteristics that maximize injectivity while minimizing negative impacts from mixing, trapping, and flow instabilities, ultimately achieving the highest possible storage efficiency.

5.5.2 Reservoir shape

Storage capacity or total pore volume is often named as a site selection criterion in literature [46, 337–340, 351], and even though it must align with project needs, large reservoirs might not be more efficient than smaller ones. In some cases, multiple smaller reservoirs may offer greater flexibility and efficiency than a single large one. Therefore, reservoir efficiency is often more important than absolute volume, and therefore we do not classify this among the most influential parameters. However, storage capacity might be of influence for economic and infrastructure reasons, such as the working gas volume relative to the needed cushion gas volume and the availability of the infrastructure in the vicinity of the fields. This will be discussed further in section 5.8.

Several simulation studies that performed a sensitivity analysis showed that formation thickness plays a significant but context-dependent role in underground hydrogen storage. Thicker reservoirs generally provide greater pore volume, enabling higher hydrogen injection capacity and increased water displacement [344]. However, thinner formations can offer advantages in terms of withdrawal efficiency and hydrogen purity due to shorter diffusion paths and steeper pressure gradients, particularly during early storage cycles. While thickness positively influences injectivity, its impact on recovery efficiency is more complex and depends on reservoir permeability, as shown in the sensitivity analysis of several studies [338, 343, 348]. Therefore, there is often an optimal reservoir thickness, rather than a general trend where increasing thickness consistently improves UHS. The optimal thickness depends on the reservoir characteristics and can be defined after further analysis, such as reservoir simulation. Therefore, thickness will not be taken into account as a site selection criterion, since it requires further analysis, which is more suitable for stage 3.

Steeply dipping structures are widely regarded as favorable for underground hydrogen storage in both saline aquifers and depleted gas reservoirs, as demonstrated by various reservoir simulation studies [338, 343, 350, 370, 371]. These structures consistently rank among the top site selection criteria due to their ability to reduce gas mixing, limit lateral hydrogen spreading, and enhance gravitational segregation. In saline aquifers, steep dips also help to mitigate water upconing during withdrawal, thereby improving recovery efficiency and containment [25, 370]. Overall, a positive correlation between dip angle and storage performance has been observed. Even though a minimum dip angle is not included in the screening stage of other studies [338, 343], we recommend avoiding flat reservoirs with dips less than 5 degrees, as the very low density of H_2 will cause the plume to spread laterally over a large distance, making it hard to recover back. Structures with higher dip angles provide greater benefits compared to those with lower dips, which is reflected in the ranking phase.

5.5.3 Operational conditions

Depth, pressure, and temperature are widely recognized as key criteria for underground hydrogen storage site selection (see Table 5.1). While these parameters are interrelated, pres-

sure becomes a more reliable indicator in depleted gas reservoirs, where prior production decouples it from depth.

Identifying optimal conditions is a complex task, as these properties affect the thermophysical properties, injectivity, recovery efficiency, microbiological activity, compression costs, and the risk of caprock leakage. This section focuses specifically on their influence on reservoir performance, defined here as injectivity and recovery efficiency. Among these, sensitivity analyses show that pressure consistently emerges as the most critical factor, while temperature plays a relatively minor role [338, 343, 372]. Therefore, temperature is excluded from the most influential site selection criteria for Reservoir Performance proposed in this study.

The thermophysical properties of hydrogen vary with depth due to increasing pressure and temperature. Assuming a linear geothermal gradient of 33 °C/km and a hydrostatic pressure gradient of 10 bar/100 m, the density of H_2 nearly doubles between depths of 1000 and 2000 m, while viscosity increases by only about 10%. As a result, the volumetric energy density increases significantly more than the viscosity, leading to a theoretical improvement in productivity with increasing depth.

Therefore, some studies advocate for deeper reservoirs with higher pressures to achieve improved volumetric energy density [351, 360]. For example, Chen et al. [348] found in their sensitivity analysis, that greater depth and pressure positively influence hydrogen recovery efficiency and injectivity, though their model does not account for the effect on roundtrip efficiency due to an increase in compression energy needed. Similarly, Buscheck et al.[373] suggested deeper reservoirs with greater pressure because it maximizes the volumetric energy storage density. Besides that, they found that the effect viscous fingering and gravity override will be decreased at higher pressures.

It is worth to be highlighted that in contrast to CO_2, hydrogen density increases smoothly with increasing depth. As such, the gain in the amount of energy storage at deeper reservoirs is much less relevant for UHS than for CO_2 storage. Indeed, CO_2 turns to supercritical at depths higher than ~800 m, as a result, its density jumps significantly to higher values. This is not the case for hydrogen [374]. Indeed, Okoroafor et al. [338] and Sekar et al. [343] show with a simulation study that productivity decreases with increasing reservoir pressure (and higher depths) due to higher compression energy demands. Consequently, lower pressures, typically found in shallower reservoirs, are considered more favorable, and these studies recommend assigning higher scores to low-pressure sites.

Other studies focus on balancing depth with caprock sealing effectiveness by performing a more theoretical analytical modelling study to identify the optimal storage depth. They propose optimal depths of 1100–1600 m to maximize hydrogen capacity while minimizing leakage risk [304, 375].

Regarding depth limits, Okoroafor et al. [338] recommends excluding fields deeper than 3000 m, citing declining productivity. This is consistent with other studies, which also support depth limits in this range for decreased storage volume while avoiding exceeding the capillary breakthrough [304, 375]. Finally, to ensure withdrawal without artificial lift, it is proposed that reservoir pressure must exceed wellhead pressure by at least 1 bar per 100 m of depth, accounting for gravity and friction losses in the wellbore [338].

Effects of depth, pressure and temperature on other aspects of site selection such as bio-geochemistry, economics and geomechanics will be discussed in the next sections.

5.5.4 Rock properties

Although high porosity enhances storage capacity, it is not considered a key factor influencing injectivity or hydrogen recovery efficiency based on sensitivity analysis of reservoir simulation studies [338, 343, 348]. In contrast, permeability is consistently identified as one of the most influential reservoir properties for UHS performance [338, 344, 348]. Generally, higher permeability improves hydrogen recovery and injectivity [338, 343]; however, in saline aquifers, very high permeability can slightly reduce recovery efficiency due to increased water production from upconing [348]. To ensure adequate performance, permeability and porosity are indeed required to be higher than some minimum values. The literature suggests the minimum values of 50 mD and 10% for permeability and porosity, respectively [338].

Reservoir heterogeneity is another key factor influencing UHS performance. Homogeneous systems enhance both productivity and storage efficiency by supporting more uniform gas flow and reducing phase interference [338, 350, 376, 377]. In contrast, high-permeability layers may lead to excessive lateral hydrogen migration, while low-permeability barriers can hinder upward gas flow during withdrawal, promoting increased water production [25, 338]. In scenarios involving cushion gases or residual hydrocarbons, reservoir homogeneity becomes even more important: it helps to minimize mechanical dispersion and gas mixing, improving hydrogen purity in the production stream [350, 376]. This can potentially mean the expected performance in fairly homogeneous sandstones is higher than heterogeneous fractured carbonates.

In contrast to the oversimplified definitions of heterogeneity in the UHS literature either by assuming layered-permeability distributions [338] or using hard-to-quantify depositional environment [350], we propose to use the Dykstra-Parsons coefficient[378] to describe the degree of heterogeneity, i.e.,

$$V = \frac{K_{50} - K_{84.1}}{K_{50}}. \tag{5.4}$$

Here, V is the Dykstra-Parsons coefficient, K_{50} is the median permeability, and $K_{84.1}$ is the permeability at the 84.1^{th} percentile. The coefficient quantifies the degree of permeability variation; values close to 0 indicate a homogeneous reservoir, while values approaching 1 signify high heterogeneity.

Finally, while a low anisotropy ratio (k_v/k_h) is generally preferred to support vertical hydrogen migration, so far, it has not yet been found to be a highly sensitive parameter [338].

5.6 Bio-Geochemistry

The injection of hydrogen into porous geological reservoirs can alter the chemical equilibrium between formation water, dissolved gases, and the rock matrix. This disturbance may initiate a variety of geochemical reactions [11]. Additionally, hydrogen serves as an electron donor for a wide range of microbial processes in the subsurface [27, 28]. These bio-geochemical processes can pose several risks, such as hydrogen consumption and contamination, biofilm formation, clogging of flow pathways, mineral dissolution or precipitation impacting injectivity, the formation of leakage pathways, and the degradation of caprock integrity [11, 27, 29].

Bio-geochemical reactions are typically classified into biotic (microbial) and abiotic (geochemical) processes. While recent studies suggest that geochemical processes alone may not pose a significant risk to the feasibility of underground hydrogen storage in porous reservoirs [316, 343, 367], a strong interaction between biotic and abiotic reactions has been observed [379, 380].

The diversity of microbial species, combined with the wide variety of possible reaction pathways and the varying environmental conditions that favor different microbial groups, makes it extremely difficult to predict the extent and impact of subsurface hydrogen reactions. Nonetheless, it is evident that bio-geochemical processes can substantially affect the efficiency and safety of UHS operations [27, 29] and must therefore be carefully evaluated during site selection and project design.

Multiple factors influence the likelihood and severity of bio-geochemical risks. Based on the literature [11, 27–29, 343, 369, 381], the most critical parameters for microbial activity are temperature, pH, and salinity. Microbial growth is likely within temperature ranges of 20–80 °C, pH values between 3 and 8, and salinities below 100 g/L, as explained by Dopffel et al. [27]. Therefore, within this range, microbial risks should be assessed site-specifically. However, microbial activity cannot be ruled out even outside these ranges. Additional important parameters include brine composition and rock mineralogy, which will be further discussed in the following subsections.

5.6.1 Temperature

Temperature plays a crucial role in determining microbial viability and activity [11, 27–29]. According to the microbial risk classification proposed by Thaysen et al. [29], the upper temperature limit for microbial life is approximately 122 °C [382, 383], beyond which microbial processes are not expected. A low microbial risk is associated with temperatures above 90 °C. A medium risk is identified for the range between 55–80 °C, depending on reservoir salinity. Below 55 °C, microbial activity is considered high-risk due to optimal growth conditions for many hydrogen-consuming microbial species, including species with high salinity tolerance.

5.6.2 Brine Composition

Together with temperature, the pH and salinity of the formation water are key controls on microbial activity. Microorganisms commonly found in subsurface environments, such as methanogens, sulfate-reducers, homoacetogens, and iron(III) reducing bacteria—typically exhibit optimal growth at pH values between 6.0 and 7.5 [11, 28]. However, active microbial processes have also been reported in a broader pH range of 3 to 8 [27], with reduced activity expected outside this range.

Higher salinities are generally beneficial for minimizing microbial risks. Above 100 g/L, microbial diversity and activity are significantly reduced [27]. In reservoirs with salinities above 100 g/L and temperatures exceeding 55 °C, no cultivated hydrogen-consuming microbes have been identified [29]. However, at lower temperatures, certain microbial species may tolerate extreme salinity conditions.

For site-specific assessments, other key factors include the presence of electron acceptors (e.g., sulfate, nitrate, ferric iron), carbon sources (e.g., carbonate/CO_2, organic compounds), and the brine activity coefficient. Measurements of total or metabolically

active microbial cell counts, as well as microbial community analyses, are valuable tools for evaluating microbial risks [27–29].

5.6.3 Rock Composition

The composition and mineralogy of the reservoir rock significantly influence both biotic and abiotic reactions. Sandstone reservoirs with high quartz content and low concentrations of reactive minerals such as calcite, carbonates, sulfates (e.g., anhydrite), and clays are generally preferred to minimize reaction potential [11, 27, 343, 355, 380, 381, 384]. In such lithologies, hydrogen losses due to abiotic reactions have been reported to be negligible [385]. In contrast, formations containing higher amounts of reactive minerals, particularly carbonate rocks such as limestone and dolomite, have been associated with more significant geochemical reactions, resulting into significant H_2 loss of up to 9.5% and porosity reduction of up to 47 % [381, 386, 387]. It is worthwhile to highlight that the extent of these reactions varies widely depending on the experimental conditions and rock chemical compositions; notably, some studies have reported only minor exposure effects for carbonate rocks [388, 389].

5.7 Geomechanical Risks & Containment

The cyclic injection and withdrawal of hydrogen in underground reservoirs causes repeated pressure fluctuations, directly impacting the subsurface stress regime. These variations can induce rock deformation, alter porosity and permeability, reduce caprock sealing efficiency, and lead to induced seismicity via fault reactivation, subsidence or uplift, and wellbore instability [11, 19, 26]. As such, geomechanical integrity is critical to ensuring both containment and operational safety in underground hydrogen storage.

Depleted gas reservoirs are advantageous over aquifers due to their proven containment performance and better-characterized mechanical behavior. However, their suitability still depends on local stress conditions, fault activity, and caprock integrity. For a comprehensive review on geomechanical considerations and site selection guidance, see Kumar et al. [19].

Bio-geochemical processes can further influence geomechanical stability by altering pore pressure, reducing mineral cohesion, and changing rock permeability, thereby contributing to stress redistribution, fault weakening, and increased risk of deformation or leakage [19]. Wellbore instability should be considered during the implementation of UHS, e.g. by selecting the right materials and implementation of suitable monitoring methods to detect leakage of H_2 along the wellbore [19]. In addition to the operational wells, abandoned wells can also pose a risk for hydrogen leakage, so the presence, condition, and age of pre-existing wells should be carefully evaluated as part of the site-specific selection process (stage 3) [346].

One of the most effective ways to mitigate geomechanical hazards, such as seismicity, subsidence and leakage through the caprock, is to select a site with a well-characterized geomechanical profile, providing insight into rock properties, in-situ stress, and failure mechanisms [19]. However, full geomechanical characterization is time-consuming and may not be feasible during the early screening phases. Therefore, it is recommended that detailed geomechanical analyses be reserved for the final selection stage, applied only to the most promising sites.

Geomechanical risks can be broadly categorized into two main groups: leakage through the caprock and seismicity due to fault reactivation. These are discussed along with potential site selection criteria in the following sections, with a focus on efficient site screening using readily available data.

5.7.1 Caprock

Kumar et al. [19] emphasize the importance of thick, low-permeability caprocks, consistent with other proposed site selection frameworks [338, 351, 352, 390]. In stage 1 of site screening, depleted gas fields can be assumed to have adequate sealing capacity due to their containment history (see section 5.3 for comparison between methane and hydrogen). For aquifers, minimum caprock thicknesses of 10 - 50 m, and a minimum permeability of 0.01 mD are suggested in literature [338, 342, 351, 352, 390]. However, these numbers are generally not based on numerical simulations or experimental measurements. In our study, we propose a minimum caprock thickness of 30 meters, based on the pore network study of Wang et al. [391]. They concluded that with lower thicknesses, leakage becomes significant. Their study included multiple shale samples, of which the maximum permeability is 0.02 mD, which we base our minimum permeability value on. In stage 2, sites with thicker and less permeable caprocks are preferred, with depleted fields scoring higher than aquifers.

As discussed in section 5.5, the column height of safely stored hydrogen depends on pressure, temperature, and depth, which in turn affects the risk of capillary breakthrough into the caprock. Optimal storage depths between 1100–1600 m and a maximum around 3000 m are recommended [304, 375].

Excessive injection pressure can fracture the caprock, creating potential leakage pathways. Sekar et al. [392] propose evaluating sites based on the ratio of injection pressure to fracture pressure, the latter being calculable from in-situ stresses, Biot's coefficient, Poisson's ratio, pore pressure, and tensile strength. While this is a valuable analysis, we recommend it as part of the detailed site evaluation in stage 3.

Caprock type and composition are critical to seal integrity. As discussed earlier, wettability and pore size control capillary entry pressure, with small-pore, water-wet systems being most favorable [393]. Shales, salt rocks, and anhydrites are commonly considered caprocks due to their low permeability and small pore sizes. Salt typically has the lowest permeability and pore size, resulting in very high capillary entry pressures [394]. Shale is the most frequently mentioned caprock in the literature and provides effective sealing due to its microporous structure and high tortuosity [394]. Anhydrites have slightly larger but isolated pores, which still lead to sufficiently low permeability [394]. Caprocks containing reactive minerals, such as carbonates or sulphates, are generally less ideal, as geochemical reactions may compromise long-term integrity [11, 395] (see Section 5.6). Therefore, careful evaluation of caprock composition is essential.

In conclusion, thickness and permeability are the most influential and easily screenable parameters, which are therefore considered in stage 1 and 2. However, other parameters such as caprock type, pore structure, wettability, composition, and its mechanical properties should be taken into account in the third stage.

5.7.2 Faults and Seismicity

Faults present a dual risk in UHS: they can act as potential leakage pathways and may also be reactivated under cyclic pressure changes, potentially compromising caprock integrity and triggering induced seismicity [19]. Therefore, sites with extensive faulting should be avoided [328, 338]. However, in specific cases faults can also be beneficial if they are sealing, as they may act as structural traps. If faults are present in shortlisted sites, a detailed geomechanical analysis should be conducted during stage 3 to assess their stability and sealing potential.

Sites near active faults or those that have experienced recent seismic events should be naturally eliminated early in the screening process, as pressure build-up may trigger fault reactivation [328, 338]. In addition, we recommend performing base-line monitoring surveys to quantify sensitive weak zones as well as the current level of activities before any operation starts.

5.8 Location & Techno-economics

Location and techno-economic considerations are not always directly considered in site selection studies on UHS. However, in real-world project development, these factors often become the primary drivers of site selection and overall feasibility. In the following sections, we focus on the key factors that influence the techno-economic performance and location of potential UHS sites.

5.8.1 Techno-economics

The techno-economics of Underground Hydrogen Storage are primarily governed by capital expenditures (CAPEX), such as drilling and cushion gas injection, and operational expenditures (OPEX), including monitoring and maintenance. The levelized cost of storage (LCOS) integrates these costs over the project's lifetime to evaluate the total costs per stored unit of H_2.

Depleted reservoirs are typically favored over aquifers due to the presence of existing infrastructure and residual gas which lowers the demand for cushion gas, which lowers both CAPEX and the need for extensive site characterization [396, 397]. The LCOS is also found to be lower for depleted gas reservoirs [398].

Cushion gas is typically the largest contributor to LCOS, often exceeding 50% of total costs [345, 397–399]. Selecting reservoirs with a high working gas to cushion gas (WG/CG) ratio can therefore significantly reduce costs [340]. Other major cost drivers include compression and gas cleaning, whereas wells and piping contribute relatively little (3 - 5%) according to [399]. However, this study does not consider leakage from piping. Baghirov et al. [400] found that the transportation of H_2 contributes 84% to the CO_2 equivalent emissions of green UHS projects. This was the case due to leakage from the pipelines. Therefore, we do consider the distance to any H_2 network as a factor in our ranking phase.

A common assumption is that depleted gas reservoirs require approximately 50% cushion gas (a WG/CG ratio of 1:1), while aquifers require up to 80% (a WG/CG ratio of 1:4) [401–403]. However, actual ratios vary widely depending on reservoir properties [404]. Site selection should therefore aim to minimize cushion gas requirements, but precise estimation of absolute volumes requires more data and can be time consuming. Therefore,

this is more appropriate for detailed feasibility studies. During the initial screening phase (Stage 2), if the WG/CG ratio is not known, we propose to assume 1 for depleted gas fields and 0.25 for aquifers, and to focus on more general geological criteria known to influence cushion gas demand.

Heinemann et al. [404] identified reservoir permeability, depth, and trap geometry as key controls on the WG/CG ratio. Zhao et al. [345] also found that reservoirs with higher porosity and permeability are more cost-effective for hydrogen storage, primarily due to lower cushion gas requirements. High permeability improves pressure dissipation, enabling greater working gas injection with less cushion gas. Greater depth provides a wider operational pressure window, which also reduces cushion gas needs. However, deeper reservoirs also require more compression electricity, which is also a significant part of the levelized costs [338]. Trap geometry may influence brine displacement and injection performance; lower dip angles reduce pressure buildup during injection, improving WG/CG ratios. However, in depleted gas fields where brine saturation is lower, the effect of dip angle is expected to be less significant. Conversely, steeper dips may improve hydrogen recovery by enhancing buoyancy-driven upward migration, as discussed in Section 5.5. The effect of the total reservoir capacity on the LCOS is expected to be minimal [398].

In conclusion, minimizing the WG/CG ratio is essential for reducing LCOS. This is best achieved in deeper, highly permeable reservoirs, which also offer advantages for injectivity, productivity, and geomechanical stability.

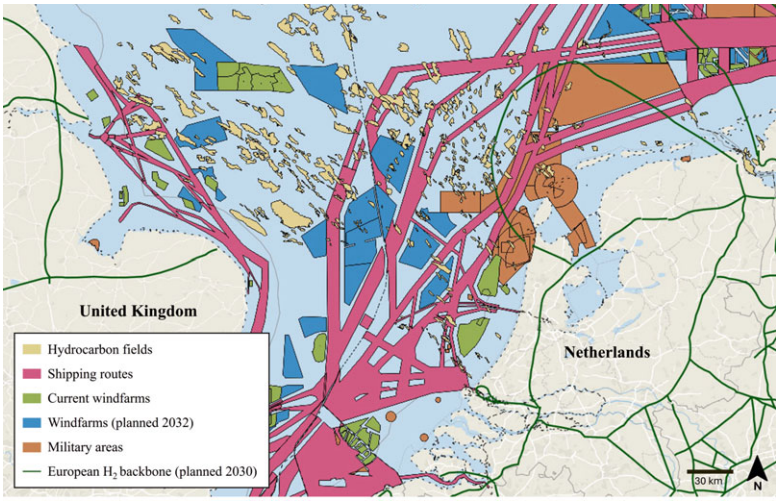

Figure 5.2: Map of the North Sea showing offshore hydrocarbon fields and key spatial constraints relevant to site selection, with permission from the North Sea Energy Atlas (https://north-sea-energy.eu/atlas) [405].

5.8.2 Location

In addition to the economic considerations discussed in the previous section, several spatial and regulatory factors must also be taken into account during site selection. Certain fields must be excluded from consideration if they fall within zones reserved for other purposes,

such as wind farms, shipping lanes, military operations, or environmentally protected areas. These constraints significantly reduce the number of viable locations for Underground Hydrogen Storage. Figure 5.2 presents a map of the hydrocarbon fields in the North Sea, in combination with other uses of the North Sea, illustrating the extent to which spatial constraints limit the availability of suitable sites.

Furthermore, public perception and the perceived risks associated with hydrogen storage, particularly for onshore sites, can influence the feasibility of a given location. In areas with high population density, these concerns are often more pronounced and may impact regulatory approval and project acceptance. While these societal factors play a crucial role in later project stages (as discussed in section 5.10), they are highly context specific and difficult to generalize and quantify. We therefore choose not to include them in the initial screening, and instead focus primarily on excluding fields located within restricted or protected zones and their distance to a H_2 network.

5.9 Framework

Based on the combined analysis of the previous sections, a multidisciplinary systematic framework is developed which focuses on the most influential and practically applicable criteria to enable effective field elimination and ranking. The criteria for both elimination and ranking are summarized in Figure 5.3. As described in the subsequent sections, many criteria might overlap between different categories. The criteria are displayed under the category which is most suitable.

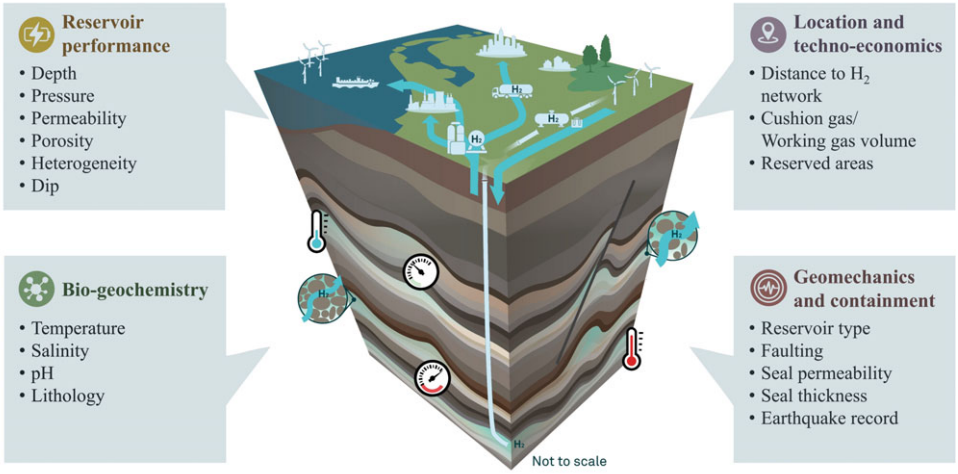

Figure 5.3: Most important site selection criteria for efficient ranking and elimination of potential fields for UHS.

The selection criteria are subdivided into elimination criteria and ranking criteria, which are quantified in the following sections. These criteria are, as much as possible, evidence-based—derived from experimental studies, numerical simulations, or well-established reasoning. However, quantifying precise values remains challenging, as they often depend on site-specific conditions and multiple interacting factors. As a result, we rely on general

trends that indicate whether a parameter is likely to have a positive or negative impact on the suitability of a site for Underground Hydrogen Storage. The methodology used to derive these values is described in detail within each respective category. The sources informing our criteria are listed in the subsequent tables though in some instances, we determined the final numerical values ourselves, based on a synthesis of multiple referenced studies.

5.9.1 Stage 1: Elimination

Table 5.3 presents the elimination criteria proposed in this study. Any field exhibiting one or more properties that fall within these thresholds should be excluded from consideration for Underground Hydrogen Storage, based on our proposed framework.

Criterion	Disqualifying condition
Reservoir Performance	
Depth	>3000 m [304, 338, 375]
Pressure	<Wellhead pressure + (0.01 bar/m) × reservoir depth [338]
Permeability	<50 mD [338]
Porosity	<10% [338, 352]
Net reservoir thickness	<10 m [338, 352]
Reservoir dip	<5 deg
Geomechanical Risks & Containment	
Distance to active faults	<4 km [406]
Earthquake record	<5 km, magnitude <5 (2015–present); <10 km, magnitude >5 (1769–present) [338, 406]
Top seal thickness*	>30 m [391]
Top seal permeability*	>0.02 mD [391]
Location & Techno-Economics	
Policies	Protected areas; reserved areas (oil/gas); shipping routes; wind farms; military activities

Table 5.3: Disqualifying thresholds used in Stage 1: site elimination. If a field meets any of the listed conditions, it is excluded from further consideration. *Only applicable when top seal integrity is unproven, such as aquifers without prior gas containment.

5.9.2 Stage 2: Ranking

Table 5.4 summarizes the most influential ranking criteria identified in this study. The ideal field characteristics are listed in the rightmost column, while the least favorable properties are shown in the second column from the left.

Depth and pressure are critical parameters influencing injectivity, recovery efficiency, gas purity, and cost in UHS. Higher depths generally lead to increased pressure, which improves volumetric energy density, reduces viscous fingering, and enhances hydrogen containment. However, deeper reservoirs require more compression energy, which increases operational costs and may reduce round-trip efficiency. Additionally, deeper reservoirs are harder to monitor, which is an important factor especially for pilot studies.

Pressure, more than depth, has been identified in several sensitivity analyses as the most influential operational parameter. Higher pressures can improve injectivity and reduce mixing but may lower net energy efficiency due to compression requirements. Additionally, while the storage density increases at greater depths, the risk for capillary leakage also increases at depth.

Taking this all into account, we suggest that intermediate depths are optimal for UHS, balancing the effect of various processes. Therefore, we suggest optimal depths between 1000 and 1500 m and corresponding pressures of 100 - 150 bar (assuming hydrostatic pressures), which is in the same range as proposed in the literature [304, 375].

Criteria	1 (worst)	2	3 (best)
Reservoir Performance			
Depth [m] [304, 338, 343, 348, 351, 360, 375]	<500; >2000	500 - 1000; 1500 - 2000	1000 - 1500
Pressure [bar] [304, 338, 343, 348, 351, 360, 375]	<50; >200	50 - 100; 150 - 200	100 - 150
Permeability [mD] [338, 344, 348]	<500	500 -1000	>1000
Permeability heterogeneity V [-] [338, 350]	0.8 - 1	0.5 - 0.8	0 - 0.5
Dip [deg] [31, 338, 350, 371]	5 - 10	10 - 15	>15
Purity: Bio-Geochemistry			
Salinity [g/L] [27, 28, 381]	<50	50 - 100	>100
Temperature [°C] [11, 27, 28]	40 - 60	60 – 80	>80
pH [11, 27, 28]	6 – 7.5	3 - 7.5 or 7.5 - 8	<3 or >8
Lithology [27, 343, 355, 380, 381, 384, 385]	Carbonate		Sandstone (pure)
Geomechanical Risks & Containment			
Type of reservoir	Aquifer		Depleted gas field
Faulting [328]	Extensively faulted	Moderately faulted	Limited faulted
Seal permeability [mD] [338, 351, 352, 390]	0.005 - 0.01	0.001 - 0.005	<0.001
Seal thickness [m] [19, 390]	20 - 40	40 - 100	>100
Location & Techno-Economics			
Distance to H_2 network	>60 km	30 - 60 km	<30 km
Working gas/Cushion gas ratio* [340]	<0.25	0.25 - 1	>1

Table 5.4: Evaluation criteria for Stage 2: site ranking. * If the absolute value of this ratio is not known, a value of 0.25 can be assumed for aquifers and a value of 1 can be assumed for depleted gas fields.

5.10 Challenges and Perspectives

Recently, substantial knowledge on underground hydrogen storage (UHS) has been gained. Significant advances have been made across the various disciplines involved, and when combined with existing experience from the oil and gas industry, carbon capture and storage (CCS), and underground gas storage (UGS), they provide a strong basis to derive the most influential screening and elimination criteria for UHS, as presented in Section 5.9.

This framework is developed to be applicable to any group of reservoirs. For example, in the Netherlands, there are over 500 depleted oil and gas fields [32]. These fields exhibit diverse characteristics, including large variations in depth, pressure, geometry, fluid properties, and more [32]. Identifying suitable fields among these options requires carefully balancing these different parameters. Applying the framework to such a dataset enables systematic screening and ranking, helping to select the most promising fields for further site-specific evaluation and final selection.

However, UHS in porous media still presents several unresolved challenges relevant for site selection that require multidisciplinary research. A key issue is the uncertainty regarding the relative importance of specific site selection criteria. For example, the importance of the bio-geochemical category in comparison to other criteria. Due to the limited number of operational projects, there is insufficient practical evidence on how microbial activity and chemical reactions in the subsurface may impact hydrogen purity

and storage performance in real fields. Pilot-scale projects are therefore essential to validate current assumptions and refine selection frameworks. The results of pilot-scale projects should be an important future research direction.

Recently, natural hydrogen extraction has gained increasing attention [322, 323, 407]. Numerous natural H_2 sources have been documented globally [407]. In the current absence of extensive practical experience with UHS, these natural hydrogen systems could serve as valuable "living laboratories". They offer the opportunity to study hydrogen behavior in the subsurface and may provide key insights currently lacking. For example, regarding the variety of structural traps in which H_2 can be safely stored [407].

In terms of economic feasibility, large uncertainties remain due to the early-stage development of the hydrogen market. For example, the future price and availability of hydrogen, as well as the demand for hydrogen, will play a large role in the economics of UHS projects, and consequently in the site selection.

Societal embeddedness is another critical challenge. Experiences from onshore CO_2 storage in Europe, e.g., the cancelled Barendrecht project in the Netherlands [408], have shown that technically sound projects may fail without public support. Although societal factors are not included in this framework because they are highly region-specific and difficult to quantify in a generalized way, they should be addressed explicitly in the later stages of site selection. As such, public perception and local regulatory responses must be taken into account during Stage 3 and all subsequent stages of project development [14, 15].

Some important technical aspects, such as reservoir thickness, caprock composition and integrity, abandoned wells, and fault activation, are suggested to be taken into account in the last stage of site selection (Stage 3), as they are highly case-dependent and essential data is not always easily accessible. However, these factors do define the suitability of a site. Therefore, future work should focus on describing in detail how such criteria can be evaluated in Stage 3, and how a final decision for the most suitable field can be made.

5.11 Conclusions

This study critically assesses existing literature and domain-specific studies spanning the multiple disciplines relevant to Underground Hydrogen Storage (UHS), to identify the most influential and practically assessable criteria for site selection. Drawing from this evaluation, we present a systematic framework for selecting UHS sites in porous media, integrating considerations from reservoir performance, geomechanics and containment, bio-geochemistry, and techno-economics. The resulting methodology enables efficient and reliable elimination and ranking of a large number of candidate fields. It consists of 11 site elimination criteria and 15 site screening criteria for early-stage decision-making in a scientifically grounded and efficient manner. While detailed site-specific assessments remain essential in later phases, this framework provides a robust foundation for consistent and transparent initial evaluations.

We recommend following the technical procedures presented in this article to screen all potential sites for UHS in depleted reservoirs and identify the most suited. However, as also identified in the IEA Technology Collaborative Program 42 on UHS reports [14, 15], it is crucially important to highlight the societal embeddedness and the availability of the infrastructure for final site selection strategies.

6

Conclusions and Future Work

6.1 Conclusions

By linking processes across scales and integrating numerical, experimental, and theoretical approaches, this thesis advances the understanding of the governing mechanisms in Underground Hydrogen Storage (UHS) within porous media. The findings provide critical insights into thermophysical properties, wettability, trapping, and site selection, supporting both the understanding of UHS systems and their safe and efficient development.

These outcomes were achieved through complementary investigations at the molecular, pore, and reservoir scales: molecular simulations, microfluidic experiments, pore-scale simulations, and the development of a systematic site selection framework. The studies addressed thermodynamics (Part I) and hydrodynamics (Part II), both essential for understanding and modelling UHS systems at larger scales. Insights from multiple disciplines and scales were then integrated into a site selection framework (Part III), providing a practical tool for identifying safe and efficient storage sites.

6.1.1 Part I: Thermodynamics

Part I focuses on the thermodynamics of Underground Hydrogen Storage, which describes how hydrogen and other reservoir fluids behave under various conditions such as pressure and temperature. Accurate thermodynamic data are essential for predicting hydrogen behaviour in the subsurface and are therefore critical inputs for Equations of State (EoS) and reservoir-scale simulations.

In **Chapter 2**, molecular simulations were used to generate comprehensive datasets for the H_2/brine system under reservoir-relevant conditions. Experimental data for key thermophysical properties are scarce, expensive to obtain, and often limited to narrow pressure, temperature, and salinity ranges. To address this gap, molecular dynamics (MD) and continuous fractional component Monte Carlo (CFCMC) simulations were applied to compute interfacial tensions, self-diffusivities, and solubilities of H_2 in brine across a wide range of conditions, while densities and viscosities of the NaCl solutions were derived from the simulations. The results agree well with available experimental data, with deviations smaller than 10% for most properties. New engineering correlations were developed for

interfacial tension and self-diffusivity, capturing the combined effects of temperature, pressure, and salinity, and providing fast and reliable inputs for reservoir-scale simulations of Underground Hydrogen Storage.

6.1.2 Part II: Hydrodynamics

Part II investigates the hydrodynamic mechanisms controlling hydrogen and brine flow in porous media, with a focus on wettability, multiphase displacement, and trapping phenomena at the pore scale. These insights provide key inputs for upscaled fluid functions, predicting reservoir-scale behaviour.

In **Chapter 3**, the dynamic wettability of H_2/brine systems was investigated using microfluidic experiments. Accurate wettability data are essential for modelling multiphase displacement in Underground Hydrogen Storage, yet H_2/brine contact angles were scarce at the time this research was conducted. Advancing and receding contact angles were systematically measured for H_2/water, N_2/water, and CO_2/water in microchannels covering typical sandstone pore sizes. All systems were strongly water-wet, with H_2/water advancing angles of 13°–39° and receding angles of 6°–23°. Contact angles decreased with increasing channel width, highlighting pore-size effects on wettability and flow functions. Minimal hysteresis was observed due to smooth channel walls and chemical homogeneity. Receding angles in the smallest channels (50 μm) closely matched sandstone core data, validating the microfluidic approach. No significant differences between H_2, N_2, and CO_2 were found, indicating gas-independent behaviour under these conditions. These results provide key inputs for pore- and reservoir-scale models, improving predictions of relative permeability, capillary pressure, and trapping in hydrogen systems.

In **Chapter 4**, it was systematically investigated how physical and geometrical conditions influence H_2 trapping due to bypassing. Pore-scale simulations using the lattice Boltzmann method (LBM) were performed across various geometries, including rectangular and rounded pore doublets, using fluid properties and contact angles obtained in Chapters 2 and 3 as input. The impact of channel width ratio, pore shape, capillary number, flow velocity, and fluid properties was assessed, with comparisons to CH_4 and CO_2, and results supported by theoretical analysis. Residual trapping occurs predominantly at low capillary numbers, highlighting the role of capillary forces, while higher flow rates reduce trapping due to the increased viscous forces. Trapping increases with channel width ratio, indicating that rocks with narrow distributions of channel widths are more favourable for Underground Hydrogen Storage. Local pore geometry affects isolation of the H_2 bubble: rounded pores reduce trapping, whereas angular pores enhance it. In addition, the mobility ratio strongly influences trapping, with H_2 and CH_4 behaving similarly, while CO_2, with higher viscosity, remains more mobile under the same conditions. These findings provide key insights for optimizing Underground Hydrogen Storage.

6.1.3 Part III: Site Selection

Part III develops a structured approach for site selection, translating thermodynamic, hydrodynamic, and other insights from various fields into practical criteria for identifying safe and efficient Underground Hydrogen Storage reservoirs.

In **Chapter 5**, a wide variety of studies at different scales and disciplines were reviewed to identify the most influential criteria for selecting suitable sites for Underground Hydrogen Storage. Reservoir simulation studies formed an important basis, but findings from other scales and disciplines were also incorporated to ensure robust, science-based criteria. Based on this evaluation, a systematic, multidisciplinary framework for early-stage reservoir screening was developed, integrating key factors from reservoir performance, geomechanics, containment, bio-geochemistry, and techno-economics. The framework defines 11 elimination and 15 screening criteria, enabling consistent and transparent identification of the most promising reservoirs using readily available data. While detailed site-specific analyses remain essential in later phases, this methodology provides a robust foundation for informed, efficient, and science-based decision-making in UHS site selection.

6.2 Recommendations for Future Work

Over the past years, research on Underground Hydrogen Storage has advanced significantly, yet several important knowledge gaps remain. Based on the findings of this thesis, the following recommendations for future research are proposed.

Regarding **thermodynamics**, as our understanding of pure hydrogen has increased significantly, future work should focus on the behaviour of gas mixtures representative of real reservoirs. In practice, injected hydrogen will interact with residual hydrocarbons, cushion gases, and other components, leading to mixing zones where accurate thermodynamic data are essential. Extending datasets and models to include binary and ternary mixtures will enable more realistic reservoir simulations and improve predictions of hydrogen distribution, storage efficiency, and purity.

Regarding **hydrodynamics**, recent studies have also significantly enhanced our understanding of contact angles and upscaled flow functions such as relative permeability and capillary pressure. However, reservoir-scale simulations remain highly sensitive to the choice of these functions, which depend strongly on rock type, gas composition, and local reservoir conditions. Future work should therefore focus on developing improved models for reservoir simulators that incorporate variations in rock properties and gas composition, enabling more accurate representation of spatial heterogeneities and mixed-gas effects on multiphase flow and correctly upscaling them to reservoir scale.

Hydrogen trapping directly influences the efficiency of UHS, especially during the initial storage and withdrawal cycles. Chapter 4 established a foundation for understanding trapping due to bypassing, revealing how geometry and flow conditions control this mechanism. However, bypassing represents only one of the two primary capillary trapping processes. Future research should also investigate trapping due to snap-off, as well as integrate pore-scale insights into reservoir-scale models or perform more realistic pore-scale simulations that reflect natural rock properties. A more complete understanding of both trapping mechanisms will improve predictions of storage efficiency and hydrogen recovery.

Regarding **site selection**, several challenges remain that require a multidisciplinary approach. Key uncertainties include the relative importance of specific selection criteria, particularly bio-geochemical effects, as UHS is not widely implemented yet. These aspects should be addressed through pilot-scale projects, which are essential to validate

current assumptions, refine predictive models, and improve weighting within selection frameworks. Additionally, the economic feasibility of UHS needs further investigation, as future hydrogen prices, demand, and supply dynamics will strongly influence project viability and prioritization. While societal acceptance and regulatory responses are not explicitly covered by the framework presented in Chapter 5, they are critical for successful implementation and should be explicitly considered in later stages of site selection. Finally, site-specific technical factors such as caprock integrity, fault activity, and well abandonment require dedicated research to develop detailed and standardized evaluation methods for incorporation into the final stage of site selection.

Overall, significant progress has been made in understanding Underground Hydrogen Storage, and the field has reached a much higher level of maturity compared to only a few years ago. Thanks to recent advances across multiple disciplines, the scientific foundation is now strong enough to support the design and implementation of pilot-scale projects, provided that robust monitoring strategies are in place. Nevertheless, UHS remains a highly multidisciplinary and multiscale challenge, and future research should focus on integrating insights across scales and disciplines. By closing remaining knowledge gaps and validating findings through well-designed pilot studies, the reliability, safety, and efficiency of UHS operations can be further enhanced. With continued collaborative research efforts, large-scale hydrogen storage can become a key enabler of the global energy transition.

A

Supplement to Chapter 3: Validation & Sensitivity analyses

A

A.1 Validation of the setup

The setup was successfully calibrated against the existing literature data of Jafari and Jung [218]. They performed microfluidic measurements of advancing and receding contact angles of CO_2/Water at P=10 bar and T=21°C using a chip identical to the chip used in this research. The cleaning method of Jafari and Jung was similar to our cleaning method. In order to match the setup of Jafari and Jung [218], for the first validation test (V1) a setup without filters and valves was used. However, because knowledge was gained about the behaviour and sensitivities of the system (A.2), two additional CO_2/water tests (V2 and V3) were performed with the regular setup (presented in 3.2.3 Figure 3.3). One test was done after saturating the water with CO_2, by filling the pump cylinders with half CO_2 and half pure water and leaving it overnight at a pressure of 20 bar. The other test was done with pure water. An overview of all validation tests and the test of Jafari and Jung can be found in Table A.1.

The results of the validation tests are shown in Figure A.1. The orange bars represent the measurements of Jafari and Jung [218] using a similar chip at P=10 bar and T=21°C , the green, yellow and purple bars represent respectively validation experiments V1, V2 and V3, all carried out at P=10 (±1) bar and T=20 (±2) °C.

Figure A.1 shows that the results of experiment V1, using a similar setup, match the results of Jafari and Jung. The deviation is within the experimental error.

Figure A.1 also indicates a clear effect of the filters in the setup on the advancing contact angles. When the system is not properly filtered, presence of contaminants can alter the glass wettability, resulting in an increase of advancing contact angles of up to 45°. This effect occurs especially when no valves are used, because the system has to be opened and closed for flushing before every experiment, which allows dust to attach on the open wet ends of the tubes. The effect on the receding contact angles is less evident. receding contact angles in unfiltered systems can be up to 5° higher, but this is still within the experimental error.

Lastly, when comparing the results of experiments V2 and V3, it can be seen that saturating the water with CO_2 had no significant influence on the results. This is in line with the finding that even though the water in experiment V1 was not saturated with CO_2, the results are still in agreement with the experiment of Jafari and Jung. The finding that saturating the water with a soluble gas like CO_2 does not impact the contact angle, confirms that pre-equilibrating the water during experiments with much less soluble gases, like H_2 and N_2, is not necessary, which is in agreement with Hashemi *et al.* [223].

Test Group	Gas	Liquid	Rate [µl/min]	Temperature [°C]	Pressure [bar]	Comments
JJ	CO_2	Saturated Water	0.1	21	10	Setup without filters
V1	CO_2	Pure Water	0.1	20	10	Setup without filters and valves
V2	CO_2	Saturated Water	0.1	20	10	
V3	CO_2	Pure Water	0.1	20	10	

Table A.1: Summary of the validation test groups. Test group JJ represents the results of Jafari and Jung [218].

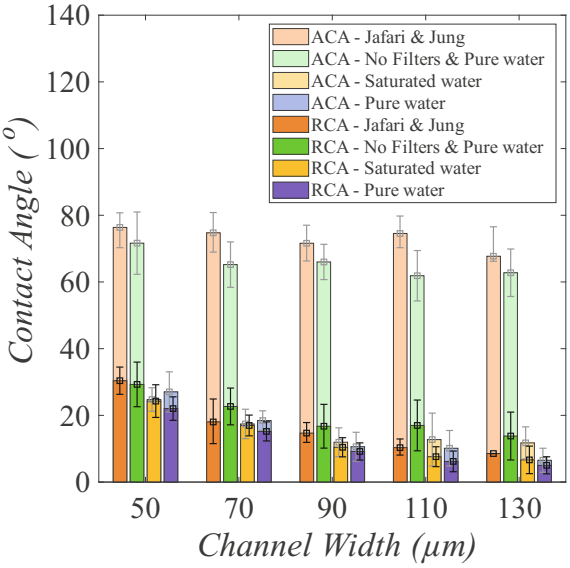

Figure A.1: Advancing and receding contact angles (ACA and RCA) of CO_2/water systems. The orange bars represent the results of Jafari and Jung [218] using a similar chip at P=10 bar and T=21°C. The green bars represent results of V1 with a setup similar to Jafari and Jung without filters and valves and with pure water, the yellow bars represent the results of V2 with water which was saturated with CO_2 and the purple bars represent the results of V3 with pure water. The error bars represent the standard deviation of the measurements.

A.2 Sensitivity analysis: Impurities

It was found that surface contamination can alter the wettability of the system. This was initially found when unfiltered ethanol was injected and the system became clearly less water-wet. In order to investigate the effect that presence of contaminants can have on the dynamic contact angles, three experiments were performed. For the first test, Chip 1, 2 and 3 were used, which were all injected with the unfiltered ethanol instead of the filtered ethanol during the cleaning procedure. This resulted in severe contamination of the system. Furthermore, the chips were heated up to 400 °C in an (unsuccessful) attempt to clean the chip. The second test was done using chip 4. This chip was cleaned with the filtered ethanol, but some tests were done without the inline filters in the gas and water lines (Filters 2 and 3 in Figure 3.3), which caused minor contamination. The third test was done with the unused chip, which was also cleaned with the filtered ethanol. Images of these chips can be seen in Figure A.2. All chips were used for tests to investigate the influence of this contamination. Contact angles were only measured if there were no visible contamination particles in the vicinity of the interface.

Figure A.3 shows the results of using different chips. The red bars represent the results of Chip 1-3, the green bars represent the results of chip 4 and the blue bars represent the results of chip 5. All experiments were carried out at P=10 (±1) bar and T=20 (±2) °C.

Figure A.3 indicates a clear effect of contamination on contact angles. It is clear that in Chip 1, 2 and 3, significantly higher advancing and receding contact angles were measured compared to chip 4 and 5. The difference between the results of chip 4 and chip 5 is less evident. The receding contact angles are very similar and the deviation are within the range of experimental error. The difference in advancing contact angles is more significant, but in most cases this is within experimental error as well. It is remarkable that the cleanest chip, chip 5, shows a wider range of advancing contact angles than chip 4. This is mainly because during imbibition experiments (measurement of advancing contact angle) in Chip 4, almost no water films were observed, while in Chip 5 the system was more water-wet because the chip was clean. In this case some interfaces used for advancing contact angle measurement had water films while others did not have a visible water film, like is shown in the images in Figure 3.8.

Because a clear effect of contamination was found, even though contact angles were not measured within the vicinity of visible pollution, all main experiments were carried out with filters, and only filtered fluids were injected. Furthermore, the system was opened inside the filters minimally in order to prevent dust from coming into the system. Installing valves 2 and 5 (Figure 3.3) enabled this, since the lines did not have to be disconnected for flushing when using valves. The findings of this appendix are in line with the findings of the CO_2 experiments in A.1.

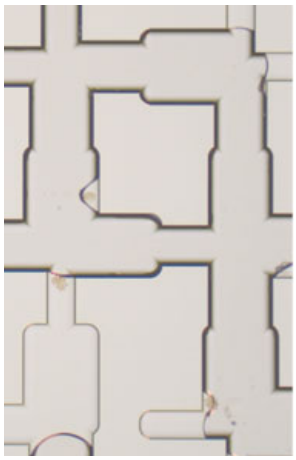

(a) Example of dirt in chip 1, 2 and 3. The chips are severely contaminated and the system is visibly less water-wet and there are no water films present.

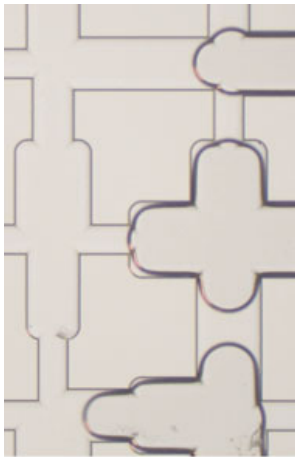

(b) Example of dirt in chip 4. A few dirt particles are visible, but the system is still very water wet and water films are observed.

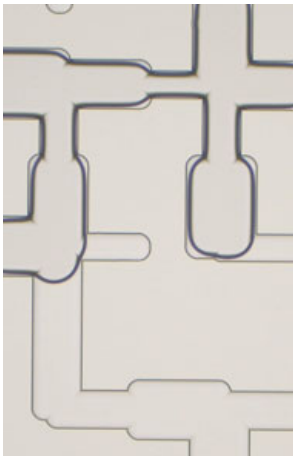

(c) Completely new chip, no dirt visible.

Figure A.2: Examples of contamination and its effect on the wettability.

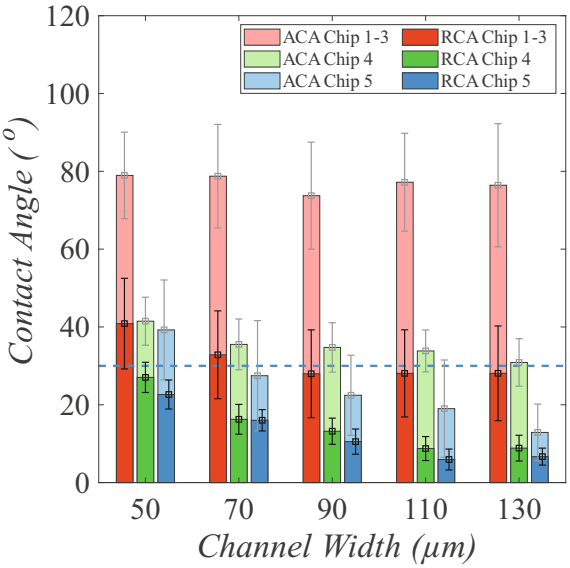

Figure A.3: Advancing and receding contact angles (ACA and RCA) of H_2 and Pure water measured at P=10 bar and T=20°C. The red bars represent measurements using chip 1, 2 and 3 which were severely contaminated, The green bars represent measurements using chip 4, which had minor contamination and the blue bars represent measurements using chip 5 which was clean. The dashed blue line represents the results found by Hashemi *et al.* [189] at P=20 bar and T=20 °C, using the captive bubble cell (CBC). The error bars are the standard deviation of all measurements.

A.3 Validation of image analysis

The image analysis code was validated against the generated specific curvature using MATLAB with the known angles at the contact points. The accuracy of the developed in-house code is ±4° which is shown in Figure A.4.

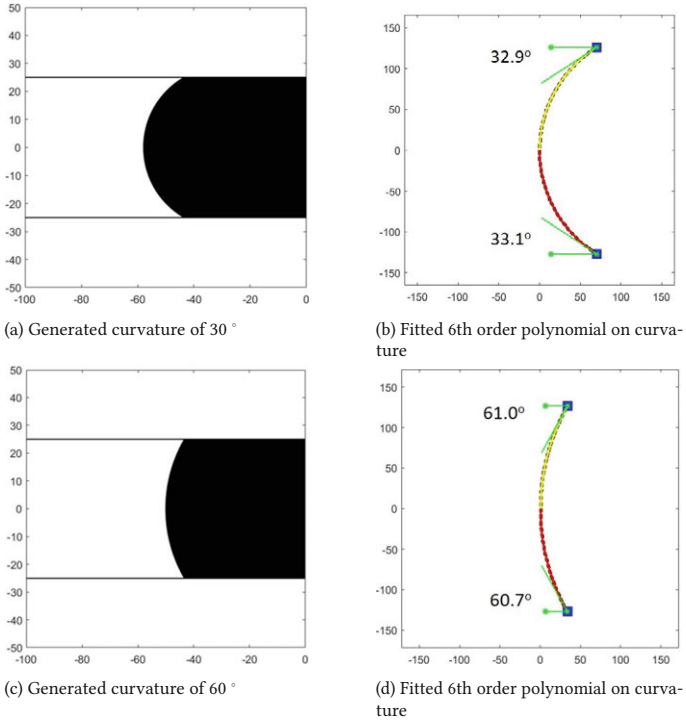

(a) Generated curvature of 30 °

(b) Fitted 6th order polynomial on curvature

(c) Generated curvature of 60 °

(d) Fitted 6th order polynomial on curvature

Figure A.4: Validation of the image analysis.

A

A.4 Sensitivity analysis: Velocity and Channel width

For one of the H_2/water drainage experiments, the velocity of each specific interface was measured using ImageJ. Figure A.5 shows the velocity distribution corresponding to the measured receding contact angles for different channel widths. No systematic relationship can be observed between receding contact angles and the velocity. This could possibly be explained by the fact that these measurements are influenced by many factors like local flow velocity, flow patterns, image analysis, image quality etc., which results in a relatively wide range of values.

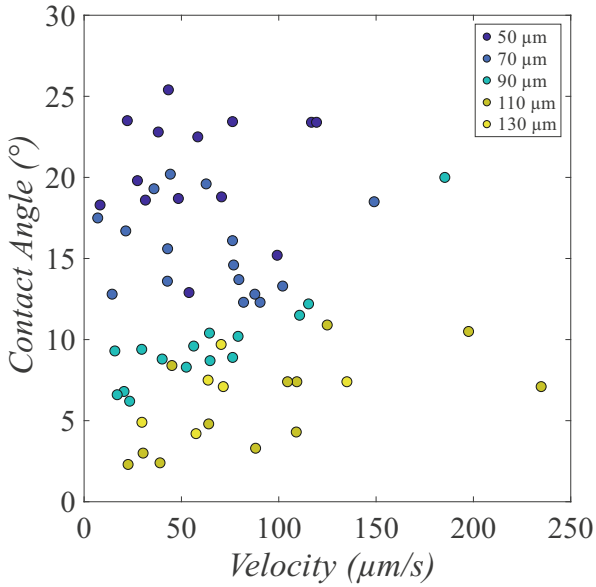

Figure A.5: Velocity of receding contact angles (RCA) of H_2/water systems. Different colors represent measurements in different channel widths.

Figure A.6 shows the average velocity of the receding contact angles of this test, and the error bars represent the standard deviation of the measurements. It can be observed that similar velocities were measured for each channel width, which suggests that the dependency of contact angles on channel width was not due to differences in velocity. Instead, one can fairly conclude that the average velocities across channel widths are in fact comparable.

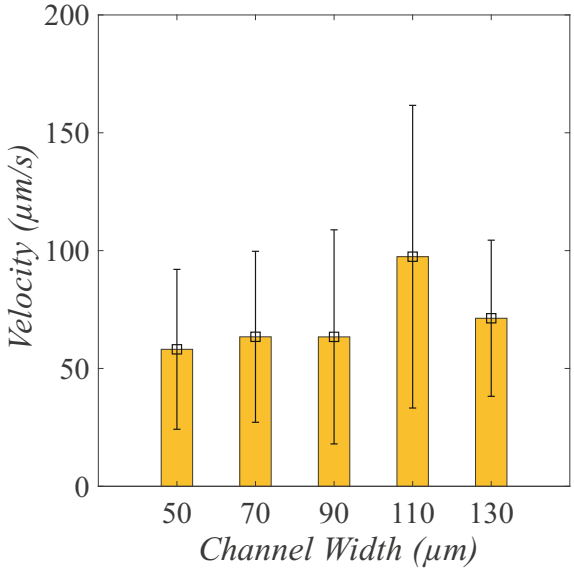

Figure A.6: Velocity range of receding contact angles (RCA) of H_2/water systems per channel width. The bars represent the average velocity of the receding contact angles (RCA) measurements of this test, and the error bars represent the standard deviation of the velocity measurements.

The contact angles are expected to be influenced by the pore size [202–204]. Our results show a relationship where dynamic contact angles increase with decreasing channel width, in agreement with the trend observed in the literature for CO_2 [218]. Multiple factors, like the shape of the channels, the capillary pressure and the velocity can influence the relationship between pore size and contact angles. Joekar Niasar *et al.* [239] found that the capillary pressure in rectangular channels can be expressed as

$$P_c = \sigma_{nw}\left(\frac{-(h+w)\cos\theta+\sqrt{(h+w)^2\cos^2\theta+4hw\left(\frac{\pi}{4}-\theta-\sqrt{2}\cos\left(\frac{\pi}{4}+\theta\right)\cos\theta\right)}}{4\left(\frac{\pi}{4}-\theta-\sqrt{2}\cos\left(\frac{\pi}{4}+\theta\right)\cos\theta\right)}\right)^{-1}, \quad \text{(A.1)}$$

where P_c is the capillary pressure, h is the channel depth and w is the channel width. The capillary pressure was calculated for a reference channel width, in this case 110 µm, using the measured contact angle θ. If the capillary pressure is assumed to be constant in the whole chip, because the regime is capillary dominated, the relationship between contact angles and channel width can be obtained by using the capillary pressure of the reference channel width and calculating the contact angles for other channel widths based on that value. However, because we deal with a dynamic system, where the capillary entry pressure needs be overcome in order for fluids to enter a channel, the assumption that capillary pressure is equal in each channel width, may not be valid. From Figure A.6, one

can conclude that the average velocities are comparable across channel widths. Berthier *et al.* [409] proposed

$$P_c = \mu \frac{p_W z}{\bar{\lambda} S_c} V \tag{A.2}$$

as the capillary pressure in rectangular channels, where

$$S_c = hw \tag{A.3}$$

$$p_W = 2(w+h) \tag{A.4}$$

$$\bar{\lambda} = \frac{\varepsilon q(\varepsilon)(w+h)}{2} \tag{A.5}$$

$$\varepsilon = h/w \tag{A.6}$$

$$q(\varepsilon) = \frac{1}{3} - \frac{64}{\pi^5} \varepsilon \tanh\left(\frac{\pi}{2\varepsilon}\right). \tag{A.7}$$

Here, μ is the viscosity and z is the distance from the inlet of the channel to the interface. Using the fact that in our experiments velocities across the channel widths are comparable ($V_i = V_{ref}$), and assuming that z is on average similar for each channel width, the equation can be rewritten as

$$\frac{P_{c_{ref}} \bar{\lambda_{ref}} S_{c_{ref}}}{p_{W_{ref}}} = \frac{P_{c_i} \bar{\lambda_{r_i}} S_{c_i}}{p_{W_i}}. \tag{A.8}$$

The left-hand-side term of this equations represents the velocity factor for the reference channel width. The capillary pressure $P_{c_{ref}}$ is calculated using equation 4.28. Equation A.8 was used to derive contact angle values for the other channel widths, using equation 4.28 to calculate P_{c_i}. The calculated contact angles represent the relationship between contact angle and channel width based on the assumption that velocity is equal in each channel width.

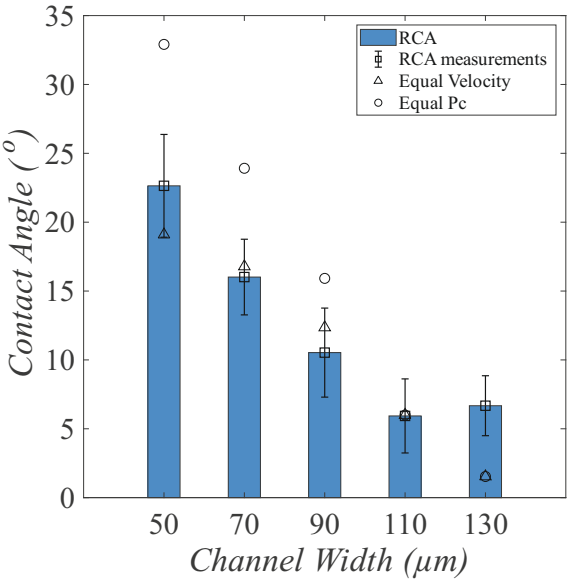

Figure A.7: Receding contact angles (RCA) of H_2 and pure water measured at P=10 bar and T=20°. The triangles represent the expected relationship between contact angle and channel width assuming the velocity to be equal in each channel width, and the circles represent the expected relationship between contact angle and channel width assuming the capillary pressure to be equal in each channel width.

Figure A.7 shows the average receding contact angles (RCA) of H_2 and pure water measurements. The triangles represent the expected relationship between contact angle and channel width assuming the velocity is equal for each channel width, and the circles represent the values assuming the capillary pressure is equal for all channel widths. For both relationships, the contact angle of the channel width of 110 μm was used as a reference point. It can be observed that the relationship assuming equal velocity resembles the measurements more closely.

B

Supplement to Chapter 4: Dimensionless variables for trapping

B.1 Motivation for dimensionless variables

In section 4.4, a theoretical analysis for the pore doublet model was presented to investigate trapping behaviour, and better understand the simulation results. As trapping due to bypassing is known to occur when capillary forces dominate over viscous foces, it was examined how key parameters influence the balance between viscous and capillary forces in the system by applying the Hagen–Poiseuille equation (Eq. 4.27) and the Young–Laplace equation (Eq. 4.28). This analysis provided a basis for understanding our simulation results.

However, predicting the system behaviour solely from these two equations remains challenging. The difficulty arises from several simplifying assumptions inherent to those two equations that do not fully capture the complexity of the pore doublet geometry and the dynamics of two-phase flow. In reality, additional factors such as the full pore doublet geometry, local interface dynamics at the junction of the channels, and multiphase flow properties significantly influence the viscous and capillary forces but are not accounted for in this simplified model.

A dimensionless analysis provides a systematic way to identify the complete set of dimensionless parameters governing the bahaviour of a system. By applying this approach to our pore doublet model, we can express the trapped saturation as a function of a minimal and independent set of dimensionless groups, which will help us understand which processes are affecting the trapped saturion. Therefore, in this section we derive the full set of dimensionless variables that describe the functional dependence of the trapped saturation, as a complementary approach to the theoretical analysis, to better understand and analyse the simulation results.

B.2 Simplifying Assumptions of the Theoretical Analysis

While section 4.4 provided a valuable basis for understanding the simulation results, its assumptions and simplifications must be considered when determining the complete set of dimensionless variables. The assumptions and simplifications are summarized below.

Simplification of the pore doublet geometry

As discussed in section 4.5, the junction where the two channels merge plays a central role in gas trapping within the pore doublet model (see figure 4.8). At this location, the interface must suddenly expand, which locally reduces the capillary pressure and can strongly influence the likelihood of snap-off, leading to trapping. This local pressure change therefore directly affects whether trapping occurs. By considering the Hagen–Poiseuille equation (Eq. 4.27) and the Young–Laplace equation (Eq. 4.28) using the methodology presented in section 4.4, the pore doublet was idealized as two straight, parallel channels without explicitly representing the junction geometry. The importance of this effect is also reflected in the large differences in trapping behaviour observed between the angular and rounded geometries (see section 4.5.2 and figure 4.11).

Viscosity ratio

The Hagen–Poiseuille equation used in the analysis describes the viscous pressure drop for a single-phase fluid. In reality, the system contains two fluids with different viscosities.

Determining a single effective viscosity for the two-phase flow is challenging because it depends on the local phase distribution (saturation) along the channels. This variability means that the viscous term in the simplified model does not fully capture the true, spatially varying resistance to flow.

Neglection of intertia
As described in section 4.3, the densities of both gas and brine were set equal to unity in the simulations, effectively neglecting inertial forces. This assumption is justified by the low Reynolds numbers and laminar flow conditions typical of the studied regime [306]. The resulting simplification removes any explicit dependence on fluid density, which we believe is a valid assumption. Therefore, the densities are not taken into account in the dimensionless variables.

B.3 Dimensionless variables

As a complementary approach to the Theoretical Analysis in section 4.4, which provides insights on how capillary pressure and viscous pressure drop are affected in the system, but do not fully capture all dynamics in the system, Buckingham's Pi theorem is applied to our system to find a set of dimensionless variables [410] that should describe the functional dependence of the trapped saturation.

First, the variables relevant to the problem and their fundamental units are listed, expressed in terms of mass M, length L, and time T. Since inertia is neglected, the same analysis could also be expressed in terms of force, length, and time, but here we use M, L, and T.

S_{trap}	Trapped saturation	$(-)$
d_1	Diameter of channel 1	(L)
d_2	Diameter of channel 2	(L)
l	Length of the channels	(L)
σ	Interfacial tension	$(M\,T^{-2})$
μ_1	Viscosity of fluid 1 (gas)	$(M\,L^{-1}\,T^{-1})$
μ_2	Viscosity of fluid 2 (liquid)	$(M\,L^{-1}\,T^{-1})$
Θ	Contact angle	$(-)$
ΔP	Imposed pressure difference (inlet–outlet)	$(M\,L^{-1}\,T^{-2})$
v_{inlet}	Average velocity at the inlet	$(L\,T^{-1})$
v_1	Average velocity in channel 1	$(L\,T^{-1})$
v_2	Average velocity in channel 2	$(L\,T^{-1})$

It is important to note that the exact junction geometry also influences the trapping behaviour. However, a geometric description is considerably more complex to quantify as a variable, and is therefore is not considered further in the dimensionless variables, but its effect is investigated in chapter 4.

B.3.1 Application of Buckingham's Pi theorem

Using this list, Buckingham's Pi theorem [410] can be applied to reduce the number of variables and identify the relevant dimensionless groups that govern the problem. In our

system we have 12 variables and three fundamental units (M, L and T). Besides that, v_{inlet}, and also v_1, and v_2 are directly dependent on ΔP. This dependency reduces the number of dimensionless variables to be found to describe the whole system by 3. This leads therefore to 12-3-3=6 dimensionless variables that are needed to describe the whole system. Two of our variables, S_{trap} and Θ are already dimensionless, which leaves us with 4 to be found dimensionless variables.

We select the repeating variables

$$d_1 \quad (L), \qquad \sigma \quad (M\,T^{-2}), \qquad \mu_1 \quad (M\,L^{-1}\,T^{-1}), \tag{B.1}$$

which together span the three fundamental units M, L, T. These variables are chosen solely to satisfy the requirements of the repeating-variable method (i.e., they are dimensionally independent and collectively span the base dimensions); the specific choice does not affect the final set of π groups, as any valid set of repeating variables would yield an equivalent dimensionless formulation. For any non-repeating variable X with dimensions

$$[M]^m\,[L]^\ell\,[T]^t \tag{B.2}$$

we form a product

$$\pi = X\,d_1^a\,\sigma^b\,\mu_1^c \tag{B.3}$$

and require π to be dimensionless. The combined dimensions of π are

$$M^{m+b+c}\,L^{\ell+a-c}\,T^{t-2b-c}. \tag{B.4}$$

Setting each exponent to zero, so that the variable will become dimensionless, gives the system

$$\begin{cases} m+b+c=0, \\ \ell+a-c=0, \\ t-2b-c=0. \end{cases} \tag{B.5}$$

We now apply this to each non-repeating variable.

d_2 ($m=0, \ell=1, t=0$)
From (B.5):

$$\begin{cases} 0+b+c=0, \\ 1+a-c=0, \\ 0-2b-c=0, \end{cases} \tag{B.6}$$

giving $a=-1$, $b=0$, $c=0$. Thus filling in equation B.3 gives

$$\pi_{d_2} = d_2\,d_1^{-1}\,\sigma^0\,\mu_1^0 = \frac{d_2}{d_1}. \tag{B.7}$$

l ($m=0, \ell=1, t=0$)
Identical algebra to d_2 yields

$$\pi_l = \frac{l}{d_1}. \tag{B.8}$$

μ_2 ($m = 1, \ell = -1, t = -1$)
From (B.5):

$$\begin{cases} 1 + b + c = 0, \\ -1 + a - c = 0, \\ -1 - 2b - c = 0, \end{cases} \tag{B.9}$$

giving $a = 0$, $b = 0$, $c = -1$. Thus

$$\pi_{\mu_2} = \mu_2 \, d_1^0 \, \sigma^0 \, \mu_1^{-1} = \frac{\mu_2}{\mu_1}. \tag{B.10}$$

V_{inlet} ($m = 0, \ell = 1, t = -1$)
From (B.5):

$$\begin{cases} 0 + b + c = 0, \\ 1 + a - c = 0, \\ -1 - 2b - c = 0, \end{cases} \tag{B.11}$$

giving $a = 0$, $b = -1$, $c = 1$. Thus

$$\pi_{V_{\text{inlet}}} = V_{\text{inlet}} \, d_1^0 \, \sigma^{-1} \, \mu_1^1 = \frac{V_{\text{inlet}} \, \mu_1}{\sigma}. \tag{B.12}$$

Variables already dimensionless
The trapped saturation S_{trap} and the contact angle Θ are already dimensionless and therefore each form a π group directly.

Summary of independent groups
This leads to the following set of six π groups

$$\begin{aligned} \pi_1 &= \frac{d_2}{d_1} && \text{(channel width ratio)}, \\ \pi_2 &= \frac{l}{d_1} && \text{(length/channel width ratio)}, \\ \pi_3 &= \frac{\mu_2}{\mu_1} && \text{(viscosity ratio)}, \\ \pi_4 &= \frac{V_{\text{inlet}} \, \mu_1}{\sigma} && \text{(capillary number)}, \\ \pi_5 &= \Theta && \text{(contact angle)}, \\ \pi_6 &= S_{\text{trap}} && \text{(trapped saturation)}. \end{aligned} \tag{B.13}$$

The dimensionless functional relationship for the problem can then be written as

$$S_{\text{trap}} = F\left(\frac{d_2}{d_1}, \, \frac{l}{d_1}, \, \frac{\mu_2}{\mu_1}, \, \frac{V_{\text{inlet}} \mu_1}{\sigma}, \, \Theta \right). \tag{B.14}$$

B.4 Evaluation of dimensionless variables

The aim of this study is to determine how the trapping percentage is influenced by various factors, thereby revealing the underlying physical and geometrical mechanisms that govern trapping in the pore doublet system. This understanding can then be used to interpret behaviour in larger, more realistic pore networks. Specifically, our objective is to identify how different dimensionless groups influence the trapped saturation, π_6.

In chapter 4, the influence of most dimensionless variables was investigated. It was found that the channel width ratio and the capillary number (π_1 and π_4) have a large effect on the trapped saturation π_6 (see Figure 4.7). Higher channel width ratios were associated with increased trapping, while trapping only occured at lower capillary numbers. Interestingly, at very low capillary numbers the trapping percentage decreased again, which can be attributed to the geometry of the junction. As noted below the list of variables, the junction geometry is not included as a variable due to its complexity. Nevertheless, it is an important factor, as it can significantly influence the trapping behavior. To investigate its effect, two junction geometries are considered in chapter 4: one with a rounded junction and one with an angular junction. The resulting impact is discussed in section 4.5, particularly in Figure 4.11 and the text refering to it.

In addition, the viscosity ratio (π_3) was also found to significantly influence trapping. Systems with different viscosity ratios, representative of H_2/brine, CH_4/brine, and CO_2/brine, were examined (see Figure 4.13). The results show that higher viscosity ratios lead to trapping at lower capillary numbers, which is consistent with the theoretical analysis.

The parameters π_2 and π_5 were not further investigated in this study, as this lies beyond its current scope. The contact angle (π_5) is assumed to be relatively similar across different UHS systems, as these systems are generally water-wet. In contrast to the channel width ratio π_1, which can be related to pore size distributions which are commonly measured for various reservoir rocks, this is not the case for the length-to-width ratio (π_2). The latter is not commonly reported and characterized in the literature for various storage rock types, making it less relevant to investigate in the present study. Nevertheless, future work could focus on quantifying π_2 and π_5, and investigating how it relates to various rock types, relevant for UHS.

Bibliography

[1] International Energy Agency, *World energy outlook 2024,* www.iea.org/weo (2024).

[2] United Nations, *The paris agreement,* (2015).

[3] I. Dincer, *Renewable energy and sustainable development: a crucial review,* Renew. Sustain. Energy Rev. **4**, 157 (2000).

[4] S. Krevor, H. de Coninck, S. E. Gasda, N. S. Ghaleigh, V. de Gooyert, H. Hajibeygi, R. Juanes, J. Neufeld, J. J. Roberts, and F. Swennenhuis, *Subsurface carbon dioxide and hydrogen storage for a sustainable energy future,* Nat. Rev. Earth Environ. **4**, 102 (2023).

[5] Netbeheer Nederland, *Netbeheer nederland scenario's editie 2025,* (2025), accessed: 13/05/2025.

[6] B. Johnston, M. C. Mayo, and A. Khare, *Hydrogen: the energy source for the 21st century,* Technovation **25**, 569 (2005).

[7] T. Mahlia, T. Saktisahdan, A. Jannifar, M. Hasan, and H. Matseelar, *A review of available methods and development on energy storage; technology update,* Renew. Sustain. Energy Rev. **33**, 532 (2014).

[8] A. Kovač, M. Paranos, and D. Marciuš, *Hydrogen in energy transition: A review,* Int. J. Hydrogen Energy **46**, 10016 (2021).

[9] L. Hashemi, M. Blunt, and H. Hajibeygi, *Pore-scale modelling and sensitivity analyses of hydrogen-brine multiphase flow in geological porous media,* Sci. Rep. **11**, 1 (2021).

[10] J. Andersson and S. Grönkvist, *Large-scale storage of hydrogen,* Int. J. Hydrogen Energy **44**, 11901 (2019).

[11] N. Heinemann, J. Alcalde, J. M. Miocic, S. J. Hangx, J. Kallmeyer, C. Ostertag-Henning, A. Hassanpouryouzband, E. M. Thaysen, G. J. Strobel, C. Schmidt-Hattenberger, *et al.*, *Enabling large-scale hydrogen storage in porous media–the scientific challenges,* Energy Environ. Sci. **14**, 853 (2021).

[12] D. Zivar, S. Kumar, and J. Foroozesh, *Underground hydrogen storage: A comprehensive review,* Int. J. Hydrogen Energy **46**, 23436 (2020).

[13] Q. Zhao, Y. Wang, and C. Chen, *Numerical simulation of the impact of different cushion gases on underground hydrogen storage in aquifers based on an experimentally-benchmarked equation-of-state,* Int. J. Hydrogen Energy **50**, 495 (2024).

[14] S. van Gessel, H. Hajibeygi, and et al., *Underground hydrogen storage: Technology monitor report. iea hydrogen tcp task 42,* https://www.ieahydrogen.org/download/17/task-reports/7067/task-42-technology-monitoring-report.pdf (2023).

[15] S. van Gessel, H. Hajibeygi, and et al., *Building confidence in underground hydrogen storage. iea hydrogen tcp task 42,* https://www.ieahydrogen.org/download/17/task-reports/9090/h2tcp-task-42-final-report.pdf (2025).

[16] R. Tarkowski, *Underground hydrogen storage: Characteristics and prospects,* Renew. Sustain. Energy Rev. **105**, 86 (2019).

[17] S. R. Thiyagarajan, H. Emadi, A. Hussain, P. Patange, and M. Watson, *A comprehensive review of the mechanisms and efficiency of underground hydrogen storage,* J. Energy Storage **51**, 104490 (2022).

[18] J. Wang, R. Wu, M. Wei, B. Bai, J. Xie, and Y. Li, *A comprehensive review of site selection, experiment and numerical simulation for underground hydrogen storage,* Gas Sci. Eng. **118**, 205105 (2023).

[19] K. R. Kumar, H. Honorio, D. Chandra, M. Lesueur, and H. Hajibeygi, *Comprehensive review of geomechanics of underground hydrogen storage in depleted reservoirs and salt caverns,* J. Energy Storage **73**, 108912 (2023).

[20] V. K. McElheny, *Hydrogen: A way out of the energy crisis?* The New York Times (1974).

[21] A. Réveillère, C. Fournier, M. Karimi-Jafari, and C. Courault, *Enabling large-scale hydrogen storage in salt caverns: recent developments,* in *Proceedings of the SMRI Spring 2022 Technical Conference*, Vol. 5 (SMRI Spring Rapid City, 2022).

[22] C. Sambo, A. Dudun, S. A. Samuel, P. Esenenjor, N. S. Muhammed, and B. Haq, *A review on worldwide underground hydrogen storage operating and potential fields,* Int. J. Hydrogen Energy **47**, 22840 (2022).

[23] Underground Sun Storage 2030 (USS 2030), *Underground sun storage 2030,* https://www.uss-2030.at/en/, accessed 2 September 2025.

[24] EUH2STARS, *Euh2stars – european underground hydrogen storage reference system,* https://www.euh2stars.eu/, accessed 2 September 2025.

[25] A. Misaghi Bonabi, W. A. van Rooijen, M. Al Kobaisi, C. Vuik, and H. Hajibeygi, *Comparative analysis of carbon dioxide and hydrogen plume migration in aquifers inspired by the fluidflower benchmark study,* Int. J. Hydrogen Energy **135**, 56 (2025).

[26] J. Miocic, N. Heinemann, K. Edlmann, J. Scafidi, F. Molaei, and J. Alcalde, *Underground hydrogen storage: a review,* Geol. Soc., London, Spec. Pub. **528**, 73 (2022).

[27] N. Dopffel, S. Jansen, and J. Gerritse, *Microbial side effects of underground hydrogen storage–knowledge gaps, risks and opportunities for successful implementation,* Int. J. Hydrogen Energy **46**, 8594 (2021).

[28] E. M. Thaysen, S. McMahon, G. J. Strobel, I. B. Butler, B. T. Ngwenya, N. Heinemann, M. Wilkinson, A. Hassanpouryouzband, C. I. McDermott, and K. Edlmann, *Estimating microbial growth and hydrogen consumption in hydrogen storage in porous media,* Renew. Sustain. Energy Rev. **151**, 111481 (2021).

[29] E. M. Thaysen, T. Armitage, L. Slabon, A. Hassanpouryouzband, and K. Edlmann, *Microbial risk assessment for underground hydrogen storage in porous rocks,* Fuel **352**, 128852 (2023).

[30] M. Boon and H. Hajibeygi, *Experimental characterization of H_2/water multiphase flow in heterogeneous sandstone rock at the core scale relevant for underground hydrogen storage (UHS),* Sci. Rep. **12**, 14604 (2022).

[31] Z. Bo, M. Boon, H. Hajibeygi, and S. Hurter, *Impact of experimentally measured relative permeability hysteresis on reservoir-scale performance of underground hydrogen storage (uhs),* Int. J. Hydrogen Energy **48**, 13527 (2023).

[32] TNO – Geological Survey of the Netherlands, *NLOG Dutch Oil and Gas portal,* https://www.nlog.nl (2025), accessed August 2025.

[33] D. Frenkel and B. Smit, *Understanding Molecular Simulation: from algorithms to applications*, 2nd ed. (Elsevier, San Diego, 2002).

[34] M. L. Porter, J. Jiménez-Martínez, R. Martinez, Q. McCulloch, J. W. Carey, and H. S. Viswanathan, *Geo-material microfluidics at reservoir conditions for subsurface energy resource applications,* Lab on a Chip **15**, 4044 (2015).

[35] S. Higgs, Y. Da Wang, C. Sun, J. Ennis-King, S. J. Jackson, R. T. Armstrong, and P. Mostaghimi, *In-situ hydrogen wettability characterisation for underground hydrogen storage,* Int. J. Hydrogen Energy **47**, 13062 (2022).

[36] A. M. Alhammadi, A. AlRatrout, K. Singh, B. Bijeljic, and M. J. Blunt, *In situ characterization of mixed-wettability in a reservoir rock at subsurface conditions,* Sci. Rep. **7**, 1 (2017).

[37] A. L. Herring, F. Gilby, Z. Li, J. McClure, M. Turner, J. Veldkamp, L. Beeching, and A. Sheppard, *Observations of nonwetting phase snap-off during drainage,* Adv. Water Resour. **121**, 32 (2018).

[38] J. Zheng, W. Lei, Y. Ju, and M. Wang, *Investigation of spontaneous imbibition behavior in a 3d pore space under reservoir condition by lattice boltzmann method,* J. Geophys. Res.: Solid Earth **126**, e2021JB021987 (2021).

[39] V. Joekar-Niasar, F. Doster, R. Armstrong, D. Wildenschild, and M. A. Celia, *Trapping and hysteresis in two-phase flow in porous media: A pore-network study,* Water Resour. Res. **49**, 4244 (2013).

[40] M. Alizadeh and M. Fatemi, *Pore-doublet computational fluid dynamic simulation of the effects of dynamic contact angle and interfacial tension alterations on the displacement mechanisms of oil by low salinity water,* Int. J. Multiph. Flow **143**, 103771 (2021).

[41] A. Q. Raeini, B. Bijeljic, and M. J. Blunt, *Numerical modelling of sub-pore scale events in two-phase flow through porous media,* Transport Porous Media **101**, 191 (2014).

[42] A. Nabizadeh, M. Adibifard, H. Hassanzadeh, J. Fahimpour, and M. K. Moraveji, *Computational fluid dynamics to analyze the effects of initial wetting film and triple contact line on the efficiency of immiscible two-phase flow in a pore doublet model,* J Mol Liq **273**, 248 (2019).

[43] Y. Mehmani, T. Anderson, Y. Wang, S. A. Aryana, I. Battiato, H. A. Tchelepi, and A. R. Kovscek, *Striving to translate shale physics across ten orders of magnitude: What have we learned?* Earth-Science Rev. **223**, 103848 (2021).

[44] S. Chen and G. D. Doolen, *Lattice boltzmann method for fluid flows,* Annu Rev Fluid mech **30**, 329 (1998).

[45] M. J. Blunt, *Multiphase flow in permeable media: A pore-scale perspective* (Cambridge university press, 2017).

[46] J. Lewandowska-Śmierzchalska, R. Tarkowski, and B. Uliasz-Misiak, *Screening and ranking framework for underground hydrogen storage site selection in poland,* Int. J. Hydrogen Energy **43**, 4401 (2018).

[47] W. A. Van Rooijen, P. Habibi, K. Xu, P. Dey, T. J. H. Vlugt, H. Hajibeygi, and O. A. Moultos, *Interfacial tensions, solubilities, and transport properties of the $H_2/H_2O/NaCl$ system: A molecular simulation study,* J. Chem. Eng. Data (2023).

[48] P. Carden and L. Paterson, *Physical, chemical and energy aspects of underground hydrogen storage,* Int. J. Hydrogen Energy **4**, 559 (1979).

[49] A. Ursúa, L. M. Gandía, and P. Sanchis, *Hydrogen production from water electrolysis: Current status and future trends,* Proc. IEEE **100**, 410 (2012).

[50] S. A. Grigoriev, V. N. Fateev, D. G. Bessarabov, and P. Millet, *Current status, research trends, and challenges in water electrolysis science and technology,* Int. J. Hydrogen Energy **45**, 26036 (2020).

[51] B. Pan, X. Yin, Y. Ju, and S. Iglauer, *Underground hydrogen storage: Influencing parameters and future outlook,* Adv. Colloid Interface Sci. **294**, 102473 (2021).

[52] P. Haug, M. Koj, and T. Turek, *Influence of process conditions on gas purity in alkaline water electrolysis,* Int. J. Hydrogen Energy **42**, 9406 (2017).

[53] P. Haug, B. Kreitz, M. Koj, and T. Turek, *Process modelling of an alkaline water electrolyzer,* Int. J. Hydrogen Energy **42**, 15689 (2017).

[54] A. Zarghami, N. Deen, and A. Vreman, *Cfd modeling of multiphase flow in an alkaline water electrolyzer,* Chem. Eng. Sci. **227**, 115926 (2020).

[55] B. E. Poling, J. M. Prausnitz, and J. P. O'Connell, *Properties of gases and liquids*, 5th ed. (McGraw-Hill Education, New York, 2001).

[56] E. Zoulias, E. Varkaraki, N. Lymberopoulos, C. N. Christodoulou, and G. N. Karagiorgis, *A review on water electrolysis,* Tcjst **4**, 41 (2004).

[57] J. Hnát, M. Paidar, K. Bouzek, A. Iulianelli, and A. Basile, *Current Trends and Future Developments on (Bio-) Membranes* (Elsevier, Amsterdam, 2020).

[58] A. Hauch, S. D. Ebbesen, S. H. Jensen, and M. Mogensen, *Highly efficient high temperature electrolysis,* J. Mater. Chem. **18**, 2331 (2008).

[59] D. Todd, M. Schwager, and W. Mérida, *Thermodynamics of high-temperature, high-pressure water electrolysis,* J. Power Sources **269**, 424 (2014).

[60] T. Holm, T. Borsboom-Hanson, O. E. Herrera, and W. Mérida, *Hydrogen costs from water electrolysis at high temperature and pressure,* Energy Convers. Manage. **237**, 114106 (2021).

[61] E. J. Slowinski, E. E. Gates, and C. E. Waring, *The effect of pressure on the surface tensions of liquids,* J. Phys. Chem. **61**, 808 (1957).

[62] L. Braun, *Über die absorption von stickstoff und von wasserstoff in wässerigen lösungen verschieden dissociierter stoffe,* Z. Phys. Chem. **33U**, 721 (1900).

[63] K. Gertz and H. Loeschcke, *Bestimmung der diffusions-koeffizienten von H_2, O_2, N_2, und he in wasser und blutserum bei konstant gehaltener konvektion,* Z. Naturforsch. B **9**, 1 (1954).

[64] Y. T. Chow, G. C. Maitland, and J. P. Trusler, *Interfacial tensions of (H_2O + H_2) and (H_2O + CO_2 + H_2) systems at temperatures of (298–448) k and pressures up to 45 mpa,* Fluid Phase Equilib. **475**, 37 (2018).

[65] R. Massoudi and A. D. King Jr, *Effect of pressure on the surface tension of water. adsorption of low molecular weight gases on water at 25 °c,* J. Phys. Chem. **78**, 2262 (1974).

[66] M. Hosseini, J. Fahimpour, M. Ali, A. Keshavarz, and S. Iglauer, *H_2-brine interfacial tension as a function of salinity, temperature, and pressure; implications for hydrogen geo-storage,* J. Pet. Sci. Eng. **213**, 110441 (2022).

[67] T. W. Richards and E. K. Carver, *A critical study of the capillary rise method of determining surface tension, with data for water, benzene, toluene, chloroform, carbon tetrachloride, ether and dimethyl aniline.[second paper.],* J. Am. Chem. Soc. **43**, 827 (1921).

[68] J. Drelich, C. Fang, and C. White, *Measurement of interfacial tension in fluid-fluid systems,* Encycl. Surf. Colloid Sci. **3**, 3158 (2002).

[69] S. Chabab, P. Théveneau, C. Coquelet, J. Corvisier, and P. Paricaud, *Measurements and predictive models of high-pressure H_2 solubility in brine (H_2O+nacl) for underground hydrogen storage application,* Int. J. Hydrogen Energy **45**, 32206 (2020).

[70] G. A. Torín-Ollarves and J. M. Trusler, *Solubility of hydrogen in sodium chloride brine at high pressures,* Fluid Phase Equilib. **539**, 113025 (2021).

[71] S. Ansari, M. Safaei-Farouji, S. Atashrouz, A. Abedi, A. Hemmati-Sarapardeh, and A. Mohaddespour, *Prediction of hydrogen solubility in aqueous solutions: Comparison of equations of state and advanced machine learning-metaheuristic approaches,* Int. J. Hydrogen Energy (2022).

[72] P. Steiner, *Ueber die absorption des wasserstoffs im wasser und in wässerigen lösungen,* Ann. Phys. **288**, 275 (1894).

[73] W. Knopp, *Über die löslichkeitsbeeinflussung von wasserstoff und stickoxydul in wässerigen lösungen verschieden dissoziierter stoffe,* Z. Phys. Chem. **48U**, 97 (1904).

[74] J. Gerecke and H. Bittrich, *The solubility of H_2, CO_2 and nh_3 in an aqueous electrolyte solution,* Wiss. Z. Tech. Hochsch. Chem. Carl Schorlemmer Leuna Merseburg **13**, 115 (1971).

[75] T. E. Crozier and S. Yamamoto, *Solubility of hydrogen in water, seawater, and nacl solutions,* J. Chem. Eng. Data **19**, 242 (1974).

[76] L. I. Gordon, Y. Cohen, and D. R. Standley, *The solubility of molecular hydrogen in seawater,* Deep-Sea Res. **24**, 937 (1977).

[77] J. Winkelmann, *Landolt-Bornstein: Numerical Data and Functional Relationships in Science and Technology, Group IV*, 1st ed., Vol. 15A (Springer-Verlag, New York, 2007).

[78] M. H. I. Baird and J. F. Davidson, *Annular jets—ii: Gas absorption,* Chem. Eng. Sci. **17**, 473 (1962).

[79] G. Houghton and D. L. Wise, *The diffusion coefficients of ten slightly soluble gases in water at 10–60° c,* Chem. Eng. Sci. **21**, 999 (1966).

[80] A. Akgerman and J. L. Gainer, *Predicting gas-liquid diffusivities,* J. Chem. Eng. Data **17**, 372 (1972).

[81] D. M. Himmelblau, *Diffusion of dissolved gases in liquids,* Chem. Rev. **64**, 527 (1964).

[82] P. T. H. M. Verhallen, L. J. P. Oomen, A. J. J. M. Elsen, J. Kruger, and J. M. H. Fortuin, *The diffusion coefficients of helium, hydrogen, oxygen and nitrogen in water determined from the permeability of a stagnant liquid layer in the quasi-s,* Chem. Eng. Sci. **39**, 1535 (1984).

[83] B. Jähne, G. Heinz, and W. Dietrich, *Measurement of the diffusion coefficients of sparingly soluble gases in water,* J. Geophys. Res.: Oceans **92**, 10767 (1987).

[84] W. J. De Blok and J. M. H. Fortuin, *Method for determining diffusion coefficients of slightly soluble gases in liquids,* Chem. Eng. Sci. **36**, 1687 (1981).

[85] L. C. Nielsen, I. C. Bourg, and G. Sposito, *Predicting CO_2–water interfacial tension under pressure and temperature conditions of geologic CO_2 storage,* Geochim. Cosmochim. Acta **81**, 28 (2012).

[86] X. Li, D. A. Ross, J. P. M. Trusler, G. C. Maitland, and E. S. Boek, *Molecular dynamics simulations of CO_2 and brine interfacial tension at high temperatures and pressures,* J. Phys. Chem. B **117**, 5647 (2013).

[87] Y. Liu, T. Lafitte, A. Z. Panagiotopoulos, and P. G. Debenedetti, *Simulations of vapor-liquid phase equilibrium and interfacial tension in the CO_2-H_2O-nacl system,* AIChE J. **59**, 3514 (2013).

[88] S. Tsuji, Y. Liang, M. Kunieda, S. Takahashi, and T. Matsuoka, *Molecular dynamics simulations of the CO_2-water-silica interfacial systems,* Energy Procedia **37**, 5435 (2013).

[89] S. Knauer, M. R. Schenk, T. Koddermann, D. Reith, and P. Jaeger, *Interfacial tension and related properties of ionic liquids in CH_4 and CO_2 at elevated pressures: experimental data and molecular dynamics simulation,* J. Chem. Eng. Data **62**, 2234 (2017).

[90] Y. Hosseinzadeh Dehaghani, M. Assareh, and F. Feyzi, *Simultaneous prediction of equilibrium, interfacial, and transport properties of CO_2-brine systems using molecular dynamics simulation: Applications to CO_2 storage,* Ind. Eng. Chem. Res. **61**, 15390 (2022).

[91] L. Zhao, J. Ji, L. Tao, and S. Lin, *Ionic effects on supercritical CO_2–brine interfacial tensions: Molecular dynamics simulations and a universal correlation with ionic strength, temperature, and pressure,* Langmuir **32**, 9188 (2016).

[92] Y. Yang, A. K. Narayanan Nair, and S. Sun, *Molecular dynamics simulation study of carbon dioxide, methane, and their mixture in the presence of brine,* J. Phys. Chem. B **121**, 9688 (2017).

[93] K. D. Papavasileiou, O. A. Moultos, and I. G. Economou, *Predictions of water/oil interfacial tension at elevated temperatures and pressures: A molecular dynamics simulation study with biomolecular force fields,* Fluid Phase Equilib. **476**, 30 (2018).

[94] A. Aminian and B. ZareNezhad, *Molecular dynamics simulations study on the shear viscosity, density, and equilibrium interfacial tensions of CO_2 + brines and brines + CO_2 + n-decane systems,* J. Phys. Chem. B **125**, 2707 (2021).

[95] S. Blazquez, I. Zeron, M. Conde, J. Abascal, and C. Vega, *Scaled charges at work: Salting out and interfacial tension of methane with electrolyte solutions from computer simulations,* Fluid Phase Equilib. **513**, 112548 (2020).

[96] D. T. Kallikragas, A. Y. Plugatyr, and I. M. Svishchev, *High temperature diffusion coefficients for O_2, H_2, and oh in water, and for pure water,* J. Chem. Eng. Data **59**, 1964 (2014).

[97] X. Zhao and H. Jin, *Investigation of hydrogen diffusion in supercritical water: A molecular dynamics simulation study,* Int. J. Heat Mass Transf. **133**, 718 (2019).

[98] I. N. Tsimpanogiannis, S. Maity, A. T. Celebi, and O. A. Moultos, *Engineering model for predicting the intradiffusion coefficients of hydrogen and oxygen in vapor, liquid, and supercritical water based on molecular dynamics simulations,* J. Chem. Eng. Data **66**, 3244 (2021).

[99] X. Zhao and H. Jin, *Correlation for self-diffusion coefficients of H_2, CH_4, co, O_2 and CO_2 in supercritical water from molecular dynamics simulation,* Appl. Therm. Eng. **171**, 114941 (2020).

[100] X. Zhao, H. Jin, Y. Chen, and Z. Ge, *Numerical study of H_2, CH_4, co, O_2 and CO_2 diffusion in water near the critical point with molecular dynamics simulation,* Comput. Math. with Appl. **81**, 759 (2021).

[101] D. Marx and P. Nielaba, *Path-integral monte carlo techniques for rotational motion in two dimensions: Quenched, annealed, and no-spin quantum-statistical averages,* Phys. Rev. A **45**, 8968 (1992).

[102] A. Köster, M. Thol, and J. Vrabec, *Molecular models for the hydrogen age: Hydrogen, nitrogen, oxygen, argon, and water,* J. Chem. Eng. Data **63**, 305 (2018).

[103] V. Buch, *Path integral simulations of mixed para-d_2 and ortho-d–2 clusters: The orientational effects,* J. Chem. Phys. **100**, 7610 (1994).

[104] J. O. Hirschfelder, C. F. Curtiss, and R. B. Bird, *Molecular theory of gases and liquids*, 1st ed. (John Wiley, New York, 1964).

[105] R. F. Cracknell, *Molecular simulation of hydrogen adsorption in graphitic nanofibres,* Phys. Chem. Chem. Phys. **3**, 2091 (2001).

[106] S. Alavi, J. Ripmeester, and D. Klug, *Molecular-dynamics study of structure ii hydrogen clathrates,* J. Chem. Phys. **123**, 024507 (2005).

[107] J. L. Abascal and C. Vega, *A general purpose model for the condensed phases of water: Tip4p/2005,* J. Chem. Phys. **123**, 234505 (2005).

[108] M. Garcia-Ratés, J.-C. de Hemptinne, J. B. Avalos, and C. Nieto-Draghi, *Molecular modeling of diffusion coefficient and ionic conductivity of CO_2 in aqueous ionic solutions,* J. Phys. Chem. B **116**, 2787 (2012).

[109] C. G. Aimoli, E. J. Maginn, and C. R. Abreu, *Transport properties of carbon dioxide and methane from molecular dynamics simulations,* J. Chem. Phys. **141**, 134101 (2014).

[110] H. Zhong, S. Lai, J. Wang, W. Qiu, H.-D. Ludemann, and L. Chen, *Molecular dynamics simulation of transport and structural properties of CO_2 using different molecular models,* J. Chem. Eng. Data **60**, 2188 (2015).

[111] H. Jiang, I. G. Economou, and A. Z. Panagiotopoulos, *Molecular modeling of thermodynamic and transport properties for CO_2 and aqueous brines,* Acc. Chem. Res. **50**, 751 (2017).

[112] C. Lopez-Lazaro, P. Bachaud, I. Moretti, and N. Ferrando, *Predicting the phase behavior of hydrogen in nacl brines by molecular simulation for geological applications,* BSGF-Earth Sci. Bulletin **190**, 7 (2019).

[113] Y. Liu, A. Z. Panagiotopoulos, and P. G. Debenedetti, *Monte carlo simulations of high-pressure phase equilibria of CO_2–H_2O mixtures,* J. Phys. Chem. B **115**, 6629 (2011).

[114] Y. Liu, T. Lafitte, A. Z. Panagiotopoulos, and P. G. Debenedetti, *Simulations of vapor–liquid phase equilibrium and interfacial tension in the CO_2–H_2O–nacl system,* AIChE J. **59**, 3514 (2013).

[115] P. Habibi, A. Rahbari, S. Blazquez, C. Vega, P. Dey, T. J. H. Vlugt, and O. A. Moultos, *A new force field for oh– for computing thermodynamic and transport properties of H_2 and O_2 in aqueous naoh and koh solutions,* J. Phys. Chem. B **126**, 9376 (2022).

[116] A. Rahbari, R. Hens, M. Ramdin, O. A. Moultos, D. Dubbeldam, and T. J. H. Vlugt, *Recent advances in the continuous fractional component monte carlo methodology,* Mol. Simul. **47**, 804 (2021).

[117] W. Shi and E. J. Maginn, *Continuous fractional component monte carlo: an adaptive biasing method for open system atomistic simulations,* J. Chem. Theory Comput. **3**, 1451 (2007).

[118] W. Shi and E. J. Maginn, *Improvement in molecule exchange efficiency in gibbs ensemble monte carlo: Development and implementation of the continuous fractional component move,* J. Comput. Chem. **29**, 2520 (2008).

[119] I. M. Zeron, J. L. F. Abascal, and C. Vega, *A force field of li^+, na^+, k^+, mg^{2+}, ca^+, cl^-, and so_4^{2-} in aqueous solution based on the tip4p/2005 water model and scaled charges for the ions,* J. Chem. Phys. **151**, 104501 (2019).

[120] S. Blazquez, M. Conde, and C. Vega, *Scaled charges for ions: An improvement but not the final word for modeling electrolytes in water,* J. Chem. Phys. **158** (2023).

[121] C. Vega and J. L. Abascal, *Simulating water with rigid non-polarizable models: a general perspective,* Phys. Chem. Chem. Phys. **13**, 19663 (2011).

[122] I. N. Tsimpanogiannis, O. A. Moultos, L. F. Franco, M. B. M. Spera, M. Erdős, and I. G. Economou, *Self-diffusion coefficient of bulk and confined water: a critical review of classical molecular simulation studies,* Mol. Simul. **45**, 425 (2019).

[123] M. A. González and J. L. Abascal, *The shear viscosity of rigid water models,* J. Chem. Phys. **132**, 096101 (2010).

[124] O. A. Moultos, I. N. Tsimpanogiannis, A. Z. Panagiotopoulos, and I. G. Economou, *Atomistic molecular dynamics simulations of CO_2 diffusivity in H_2O for a wide range of temperatures and pressures,* J. Phys. Chem. B **118**, 5532 (2014).

[125] R. Sakamaki, A. K. Sum, T. Narumi, R. Ohmura, and K. Yasuoka, *Thermodynamic properties of methane/water interface predicted by molecular dynamics simulations,* J. Chem. Phys. **134**, 144702 (2011).

[126] C. Vega and E. D. Miguel, *Surface tension of the most popular models of water by using the test-area simulation method,* J. Chem. Phys. **126**, 154707 (2007).

[127] M. F. Döpke, O. A. Moultos, and R. Hartkamp, *On the transferability of ion parameters to the tip4p/2005 water model using molecular dynamics simulations,* J. Chem. Phys. **152**, 024501 (2020).

[128] K. S. Deeg, J. J. Gutiérrez-Sevillano, R. Bueno-Pérez, J. B. Parra, C. O. Ania, M. Doblaré, and S. Calero, *Insights on the molecular mechanisms of hydrogen adsorption in zeolites,* J. Phys. Chem. C **117**, 14374 (2013).

[129] L. M. Sesé, *Study of the feynman-hibbs effective potential against the path-integral formalism for monte carlo simulations of quantum many-body lennard-jones systems,* Mol. Phys. **81**, 1297 (1994).

[130] L. M. Sesé, *Feynman-hibbs potentials and path integrals for quantum lennard-jones systems: Theory and monte carlo simulations,* Mol. Phys. **85**, 931 (1995).

[131] A. Rahbari, J. Brenkman, R. Hens, M. Ramdin, L. J. V. D. Broeke, R. Schoon, R. Henkes, O. A. Moultos, and T. J. H. Vlugt, *Solubility of water in hydrogen at high pressures: A molecular simulation study,* J. Chem. Eng. Data **64**, 4103 (2019).

[132] S. Plimpton, *Fast parallel algorithms for short-range molecular dynamics,* J. Comput. Phys. **117**, 1 (1995).

[133] J. P. Ryckaert, G. Ciccotti, and H. J. Berendsen, *Numerical integration of the cartesian equations of motion of a system with constraints: molecular dynamics of n-alkanes,* J. Comput. Phys. **23**, 327 (1977).

[134] M. P. Allen and D. J. Tildesley, *Computer simulation of liquids* (Oxford University Press, 2017).

[135] R. Hockney and J. Eastwood, *Computer Simulation Using Particles*, 1st ed. (CRC Press, New York, 1988).

[136] S. Plimpton, *Lammps documentation (15 sep 2022 version),* (2015), accessed: 26/10/2022.

[137] L. Martinez, R. Andrade, E. G. Birgin, and J. M. Martínez, *Packmol: A package for building initial configurations for molecular dynamics simulations,* J. Comput. Chem. **30**, 2157 (2009).

[138] R. E. Isele-Holder, W. Mitchell, and A. E. Ismail, *Development and application of a particle-particle particle-mesh ewald method for dispersion interactions,* J. Chem. Phys. **137**, 174107 (2012).

[139] H. S. Salehi, O. A. Moultos, and T. J. H. Vlugt, *Interfacial properties of hydrophobic deep eutectic solvents with water,* J. Phys. Chem. B **125**, 12303 (2021).

[140] J. S. Rowlinson and B. Widom, *Molecular theory of capillarity*, 1st ed. (Courier Corporation, Oxford, 1982).

[141] S. H. Jamali, L. Wolff, T. M. Becker, M. D. Groen, M. Ramdin, R. Hartkamp, A. Bardow, T. J. H. Vlugt, and O. A. Moultos, *Octp: A tool for on-the-fly calculation of transport properties of fluids with the order- n algorithm in lammps,* J. Chem. Inf. Model. **59**, 1290 (2019).

[142] D. Dubbeldam, D. C. Ford, D. E. Ellis, and R. Q. Snurr, *A new perspective on the order-n algorithm for computing correlation functions,* Mol. Simul. **35**, 1084 (2009).

[143] I.-C. Yeh and G. Hummer, *System-size dependence of diffusion coefficients and viscosities from molecular dynamics simulations with periodic boundary conditions,* J. Phys. Chem. B **108**, 15873 (2004).

[144] A. T. Celebi, S. H. Jamali, A. Bardow, T. J. H. Vlugt, and O. A. Moultos, *Finite-size effects of diffusion coefficients computed from molecular dynamics: a review of what we have learned so far,* Mol. Simul. **47**, 831 (2021).

[145] S. H. Jamali, A. Bardow, T. J. H. Vlugt, and O. A. Moultos, *Generalized form for finite-size corrections in mutual diffusion coefficients of multicomponent mixtures obtained from equilibrium molecular dynamics simulation,* J. Chem. Theory Comput. **16**, 3799 (2020).

[146] O. A. Moultos, Y. Zhang, I. N. Tsimpanogiannis, I. G. Economou, and E. J. Maginn, *System-size corrections for self-diffusion coefficients calculated from molecular dynamics simulations: The case of CO_2, n-alkanes, and poly (ethylene glycol) dimethyl ethers,* J. Chem. Phys. **145**, 074109 (2016).

[147] S. H. Jamali, R. Hartkamp, C. Bardas, J. Sohl, T. J. H. Vlugt, and O. A. Moultos, *Shear viscosity computed from the finite-size effects of self-diffusivity in equilibrium molecular dynamics,* J. Chem. Theory Comput. **14**, 5959 (2018).

[148] S. H. Jamali, L. Wolff, T. M. Becker, A. Bardow, T. J. H. Vlugt, and O. A. Moultos, *Finite-size effects of binary mutual diffusion coefficients from molecular dynamics,* J. Chem. Theory Comput. **14**, 2667 (2018).

[149] R. Hens, A. Rahbari, S. Caro-Ortiz, N. Dawass, M. Erdős, A. Poursaeidesfahani, H. S. Salehi, A. T. Celebi, M. Ramdin, O. A. Moultos, D. Dubbeldam, and T. J. H. Vlugt, *Brick-cfcmc: Open source software for monte carlo simulations of phase and reaction equilibria using the continuous fractional component method,* J. Chem. Inf. Model. **60**, 2678 (2020).

[150] H. M. Polat, H. S. Salehi, R. Hens, D. O. Wasik, A. Rahbari, F. de Meyer, C. Houriez, C. Coquelet, S. Calero, D. Dubbeldam, O. A. Moultos, and T. J. H. Vlugt, *New features of the open source monte carlo software brick-cfcmc: Thermodynamic integration and hybrid trial moves,* J. Chem. Inf. Model. **61**, 3752 (2021).

[151] A. Poursaeidesfahani, R. Hens, A. Rahbari, M. Ramdin, D. Dubbeldam, and T. J. H. Vlugt, *Efficient application of continuous fractional component monte carlo in the reaction ensemble,* J. Chem. Theory Comput. **13**, 4452 (2017).

[152] A. Rahbari, R. Hens, D. Dubbeldam, and T. J. H. Vlugt, *Improving the accuracy of computing chemical potentials in cfcmc simulations,* Mol. Phys. **117**, 3493 (2019).

[153] A. Rahbari, R. Hens, S. Jamali, M. Ramdin, D. Dubbeldam, and T. J. H. Vlugt, *Effect of truncating electrostatic interactions on predicting thermodynamic properties of water–methanol systems,* Mol. Simul. **45**, 336 (2019).

[154] F. Wang and D. P. Landau, *Efficient multiple-range random walk algorithm to calculate the density of states,* Phys. Rev. Lett. **86**, 2050 (2001).

[155] F. Wang and D. P. Landau, *Determining the density of states for classical statistical models: A random walk algorithm to produce a flat histogram,* Phys. Rev. E **64**, 056101 (2001).

[156] H. S. Salehi, R. Hens, O. A. Moultos, and T. J. H. Vlugt, *Computation of gas solubilities in choline chloride urea and choline chloride ethylene glycol deep eutectic solvents using monte carlo simulations,* J. Mol. Liq. **316**, 113729 (2020).

[157] B. Widom, *Potential-distribution theory and the statistical mechanics of fluids,* J. Phys. Chem. **86**, 869 (1982).

[158] B. Widom, *Some topics in the theory of fluids,* J. Chem. Phys. **39**, 2808 (1963).

[159] A. Rahbari, R. Hens, I. K. Nikolaidis, A. Poursaeidesfahani, M. Ramdin, I. G. Economou, O. A. Moultos, D. Dubbeldam, and T. J. H. Vlugt, *Computation of partial molar properties using continuous fractional component monte carlo,* Mol. Phys. **116**, 3331 (2018).

[160] A. Georgiadis, G. Maitland, J. M. Trusler, and A. Bismarck, *Interfacial tension measurements of the (H_2o+ CO_2) system at elevated pressures and temperatures,* J. Chem. Eng. Data **55**, 4168 (2010).

[161] S. Bachu and D. B. Bennion, *Interfacial tension between CO_2, freshwater, and brine in the range of pressure from (2 to 27) mpa, temperature from (20 to 125) °c, and water salinity from (0 to 334 000) mg· l^{-1},* J. Chem. Eng. Data **54**, 765 (2009).

[162] A. Hebach, A. Oberhof, N. Dahmen, A. Kögel, H. Ederer, and E. Dinjus, *Interfacial tension at elevated pressures measurements and correlations in the water+ carbon dioxide system,* J. Chem. Eng. Data **47**, 1540 (2002).

[163] Q.-Y. Ren, G.-J. Chen, W. Yan, and T.-M. Guo, *Interfacial tension of (CO_2 + CH_4)+ water from 298 k to 373 k and pressures up to 30 mpa,* J. Chem. Eng. Data **45**, 610 (2000).

[164] P. Naeiji, T. K. Woo, S. Alavi, and R. Ohmura, *Molecular dynamics simulations of interfacial properties of the CO_2–water and CO_2–CH_4–water systems,* J. Chem. Phys. **153**, 044701 (2020).

[165] X. Li, E. Boek, G. C. Maitland, and J. P. M. Trusler, *Interfacial tension of (brines+ CO_2):(0.864 nacl+ 0.136 kcl) at temperatures between (298 and 448) k, pressures between (2 and 50) mpa, and total molalities of (1 to 5) mol· kg^{-1},* J. Chem. Eng. Data **57**, 1078 (2012).

[166] C. A. Aggelopoulos, M. Robin, and O. Vizika, *Interfacial tension between CO_2 and brine (nacl+ $cacl_2$) at elevated pressures and temperatures: The additive effect of different salts,* Adv. Water Resour. **34**, 505 (2011).

[167] G. R. Jerauld and A. Kazemi, *An improved simple correlation for accurate estimation of CO_2-brine interfacial tension at reservoir conditions,* J. Pet. Sci. Eng. **208**, 109537 (2022).

[168] M. Manciu and E. Ruckenstein, *Specific ion effects via ion hydration: I. surface tension,* Adv. Colloid Interface Sci. **105**, 63 (2003).

[169] Y. Marcus, *Effect of ions on the structure of water: Structure making and breaking,* Chem. Rev. **109**, 1346 (2009).

[170] L. M. Pegram and M. T. Record, *Hofmeister salt effects on surface tension arise from partitioning of anions and cations between bulk water and the air-water interface,* J. Phys. Chem. B **111**, 5411 (2007).

[171] Y. Levin, A. P. D. Santos, and A. Diehl, *Ions at the air-water interface: An end to a hundred-year-old mystery?* Phys. Rev. Lett. **103**, 257802 (2009).

[172] S. Weisenberger and A. Schumpe, *Estimation of gas solubilities in salt solutions at temperatures from 273 k to 363 k,* AIChE J. **42**, 298 (1996).

[173] M. Laliberté, *Model for calculating the viscosity of aqueous solutions,* J. Chem. Eng. Data **52**, 321 (2007).

[174] M. Laliberté and W. E. Cooper, *Model for calculating the density of aqueous electrolyte solutions,* J. Chem. Eng. Data **49**, 1141 (2004).

[175] I. N. Tsimpanogiannis and O. A. Moultos, *Is stokes-einstein relation valid for the description of intra-diffusivity of hydrogen and oxygen in liquid water?* Fluid Phase Equilib. **563**, 113568 (2022).

[176] E. L. Cussler, *Diffusion Coefficients and Diffusion of Interacting Species*, 2nd ed. (Cambridge University Press, Cambridge, 2009).

[177] R. Taylor and R. Krishna, *Multicomponent mass transfer*, 1st ed., Vol. 2 (John Wiley & Sons, 1993).

[178] R. Krishna and J. Wesselingh, *The maxwell-stefan approach to mass transfer,* Chem. Eng. Sci. **52**, 861 (1997).

[179] R. Wiebe and V. L. Gaddy, *The solubility of hydrogen in water at 0, 50, 75 and 100° from 25 to 1000 atmospheres,* J. Am. Chem. Soc. **56**, 76 (1934).

[180] R. Wiebe, V. Gaddy, and C. Heins, *Solubility of hydrogen in water at 25° c. from 25 to 1000 atmospheres,* Ind. Eng. Chem. **24**, 823 – 825 (1932).

[181] G. Kling and G. Maurer, *The solubility of hydrogen in water and in 2-aminoethanol at temperatures between 323 k and 423 k and pressures up to 16 mpa,* J. Chem. Thermodyn. **23**, 531 (1991).

[182] V. R. Choudhary, M. G. Parande, and P. H. Brahme, *Simple apparatus for measuring solubility of gases at high pressures,* Ind. Eng. Chem. Fundam. **21**, 472 (1982).

[183] J. Chandrasekhar, D. C. Spellmeyer, and W. L. Jorgensen, *Energy component analysis for dilute aqueous solutions of lithium (1+), sodium (1+), fluoride (1-), and chloride (1-) ions,* J. Am. Chem. Soc. **106**, 903 (1984).

[184] F. Darkrim, J. Vermesse, P. Malbrunot, and D. Levesque, *Monte carlo simulations of nitrogen and hydrogen physisorption at high pressures and room temperature. comparison with experiments,* J. Chem. Phys. **110**, 4020 (1999).

[185] Z. Zhu, Y. Cao, Z. Zheng, and D. Chen, *An accurate model for estimating H_2 solubility in pure water and aqueous nacl solutions,* Energies **15**, 5021 (2022).

[186] W. A. van Rooijen, L. Hashemi, M. Boon, R. Farajzadeh, and H. Hajibeygi, *Microfluidics-based analysis of dynamic contact angles relevant for underground hydrogen storage,* Adv. Water Resour. **164**, 104221 (2022).

[187] D. MacKay, *Sustainable Energy-without the hot air* (UIT cambridge, 2008).

[188] M. Ali, N. K. Jha, A. Al-Yaseri, Y. Zhang, S. Iglauer, and M. Sarmadivaleh, *Hydrogen wettability of quartz substrates exposed to organic acids; implications for hydrogen trapping/storage in sandstone reservoirs,* J. Pet. Sci. Eng. , 109081 (2021).

[189] L. Hashemi, W. Glerum, R. Farajzadeh, and H. Hajibeygi, *Contact angle measurement for hydrogen/brine/sandstone system using captive-bubble method relevant for underground hydrogen storage,* Adv. Water Resour. **154**, 103964 (2021).

[190] M. Rücker, W.-B. Bartels, K. Singh, N. Brussee, A. Coorn, H. A. van der Linde, A. Bonnin, H. Ott, S. M. Hassanizadeh, M. J. Blunt, *et al.*, *The effect of mixed wettability on pore-scale flow regimes based on a flooding experiment in ketton limestone,* Geophysical Research Letters **46**, 3225 (2019).

[191] P. Kunz, S. Hassanizadeh, and U. Nieken, *A two-phase sph model for dynamic contact angles including fluid–solid interactions at the contact line,* Transport in Porous Media **122**, 253 (2018).

[192] M. J. Blunt, M. D. Jackson, M. Piri, and P. H. Valvatne, *Detailed physics, predictive capabilities and macroscopic consequences for pore-network models of multiphase flow,* Adv. Water Resour. **25**, 1069 (2002).

[193] V. Joekar-Niasar and S. Hassanizadeh, *Analysis of fundamentals of two-phase flow in porous media using dynamic pore-network models: A review,* Crit. Rev. Environ. Sci. Technol. **42**, 1895 (2012).

[194] M. A. Celia, P. C. Reeves, and L. A. Ferrand, *Recent advances in pore scale models for multiphase flow in porous media,* Rev. Geophys. **33**, 1049 (1995).

[195] G. N. Constantinides and A. C. Payatakes, *Network simulation of steady-state two-phase flow in consolidated porous media,* AIChE J. **42**, 369 (1996).

[196] P.-E. Oren, S. Bakke, and O. J. Arntzen, *Extending predictive capabilities to network models,* SPE J. **3**, 324 (1998).

[197] T. W. Patzek, *Verification of a complete pore network simulator of drainage and imbibition,* SPE J. **6**, 144 (2001).

[198] H. Dong, S. Fjeldstad, L. Alberts, S. Roth, S. Bakke, P.-E. Øren, *et al.*, *Pore network modelling on carbonate: a comparative study of different micro-ct network extraction methods,* in *International symposium of the society of core analysts, Society of Core Analysts* (2008).

[199] A. V. Ryazanov, M. I. J. Van Dijke, and K. S. Sorbie, *Two-phase pore-network modelling: existence of oil layers during water invasion,* Transport in Porous Media **80**, 79 (2009).

[200] P.-E. Øren and S. Bakke, *Reconstruction of berea sandstone and pore-scale modelling of wettability effects,* J. Pet. Sci. Eng. **39**, 177 (2003).

[201] J. Bear, *Dynamics of fluids in porous media* (Courier Corporation, 2013).

[202] D. Behnoudfar, M. I. Dragila, D. Meisenheimer, and D. Wildenschild, *Contact angle hysteresis: A new paradigm?* Adv. Water Resour. , 104138 (2022).

[203] H. S. Rabbani, V. Joekar-Niasar, and N. Shokri, *Effects of intermediate wettability on entry capillary pressure in angular pores,* J. Colloid Interface Sci. **473**, 34 (2016).

[204] H. S. Rabbani, V. Joekar-Niasar, T. Pak, and N. Shokri, *New insights on the complex dynamics of two-phase flow in porous media under intermediate-wet conditions,* Sci. Rep. **7**, 1 (2017).

[205] B. B. Sauer and T. E. Carney, *Dynamic contact angle measurements on glass fibers: influence of fiber diameter on hysteresis and contact line pinning,* Langmuir **6**, 1002 (1990).

[206] R. Tadmor, *Line energy and the relation between advancing, receding, and young contact angles,* Langmuir **20**, 7659 (2004).

[207] R. Juanes, E. Spiteri, F. Orr Jr, and M. Blunt, *Impact of relative permeability hysteresis on geological co2 storage,* Water resources research **42** (2006).

[208] S. Saraji, M. Piri, and L. Goual, *The effects of so2 contamination, brine salinity, pressure, and temperature on dynamic contact angles and interfacial tension of supercritical co2/brine/quartz systems,* Int. J. Greenh. Gas Control **28**, 147 (2014).

[209] J. L. Dickson, G. Gupta, T. S. Horozov, B. P. Binks, and K. P. Johnston, *Wetting phenomena at the co2/water/glass interface,* Langmuir **22**, 2161 (2006).

[210] D. N. Espinoza and J. C. Santamarina, *Water-co2-mineral systems: Interfacial tension, contact angle, and diffusion—implications to co2 geological storage,* Water resources research **46** (2010).

[211] L. E. Dalton, D. Tapriyal, D. Crandall, A. Goodman, F. Shi, and F. Haeri, *Contact angle measurements using sessile drop and micro-ct data from six sandstones,* Transport in Porous Media **133** (2020).

[212] X. Li, X. Fan, A. Askounis, K. Wu, K. Sefiane, and V. Koutsos, *An experimental study on dynamic pore wettability,* Chem. Eng. Sci. **104**, 988 (2013).

[213] M. Heshmati and M. Piri, *Experimental investigation of dynamic contact angle and capillary rise in tubes with circular and noncircular cross sections,* Langmuir **30**, 14151 (2014).

[214] E. Al-Zaidi and X. Fan, *Effect of aqueous electrolyte concentration and valency on contact angle on flat glass surfaces and inside capillary glass tubes,* Colloids Surf., A **543**, 1 (2018).

[215] E. R. Castro, M. D. Tarn, P. Ginterová, H. Zhu, Y. Xu, and P. Neužil, *Determination of dynamic contact angles within microfluidic devices,* Microfluidics and Nanofluidics **22**, 1 (2018).

[216] M. Arif, M. Lebedev, A. Barifcani, and S. Iglauer, *Co2 storage in carbonates: Wettability of calcite,* Int. J. Greenh. Gas Control **62**, 113 (2017).

[217] J.-H. Kim, H. P. Kavehpour, and J. P. Rothstein, *Dynamic contact angle measurements on superhydrophobic surfaces,* Physics of Fluids **27**, 032107 (2015).

[218] M. Jafari and J. Jung, *Direct measurement of static and dynamic contact angles using a random micromodel considering geological co2 sequestration,* Sustainability **9**, 2352 (2017).

[219] C. Sun, J. E. McClure, P. Mostaghimi, A. L. Herring, M. Shabaninejad, S. Berg, and R. T. Armstrong, *Linking continuum-scale state of wetting to pore-scale contact angles in porous media,* J. Colloid Interface Sci. **561**, 173 (2020).

[220] N. R. Morrow, *The effects of surface roughness on contact: angle with special reference to petroleum recovery,* J. Can. Pet. Technol. **14** (1975).

[221] A. E. Yekta, J.-C. Manceau, S. Gaboreau, M. Pichavant, and P. Audigane, *Determination of hydrogen–water relative permeability and capillary pressure in sandstone: application to underground hydrogen injection in sedimentary formations,* Transport Porous Media **122**, 333 (2018).

[222] S. Iglauer, M. Ali, and A. Keshavarz, *Hydrogen wettability of sandstone reservoirs: Implications for hydrogen geo-storage,* Geophysical Research Letters **48**, e2020GL090814 (2021).

[223] L. Hashemi, M. Boon, W. Glerum, R. Farajzadeh, and H. Hajibeygi, *A comparative study for H_2–CH_4 mixture wettability in sandstone porous rocks relevant to underground hydrogen storage,* Adv. Water Resour. **163**, 104165 (2022).

[224] N. Karadimitriou and S. Hassanizadeh, *A review of micromodels and their use in two-phase flow studies,* Vadose Zone Journal **11** (2012).

[225] N. K. Karadimitriou, H. Mahani, H. Steeb, and V. Niasar, *Nonmonotonic effects of salinity on wettability alteration and two-phase flow dynamics in pdms micromodels,* Water Resources Research **55**, 9826 (2019).

[226] Y. Kim, J. Wan, T. J. Kneafsey, and T. K. Tokunaga, *Dewetting of silica surfaces upon reactions with supercritical co2 and brine: pore-scale studies in micromodels,* Environmental science & technology **46**, 4228 (2012).

[227] N. S. K. Gunda, B. Bera, N. K. Karadimitriou, S. K. Mitra, and S. M. Hassanizadeh, *Reservoir-on-a-chip (roc): A new paradigm in reservoir engineering,* Lab on a Chip **11**, 3785 (2011).

[228] W. Song, T. W. de Haas, H. Fadaei, and D. Sinton, *Chip-off-the-old-rock: the study of reservoir-relevant geological processes with real-rock micromodels,* Lab on a Chip **14**, 4382 (2014).

[229] O. E. Godinez-Brizuela, N. K. Karadimitriou, V. Joekar-Niasar, C. A. Shore, and M. Oostrom, *Role of corner interfacial area in uniqueness of capillary pressure-saturation-interfacial area relation under transient conditions,* Adv. Water Resour. **107**, 10 (2017).

[230] J.-T. Cheng, L. J. Pyrak-Nolte, D. D. Nolte, and N. J. Giordano, *Linking pressure and saturation through interfacial areas in porous media,* Geophysical Research Letters **31** (2004).

[231] N. K. Karadimitriou, V. Joekar-Niasar, M. Babaei, and C. A. Shore, *Critical role of the immobile zone in non-fickian two-phase transport: A new paradigm,* Environmental science & technology **50**, 4384 (2016).

[232] N. K. Karadimitriou, V. Joekar-Niasar, and O. G. Brizuela, *Hydro-dynamic solute transport under two-phase flow conditions,* Sci. Rep. **7**, 1 (2017).

[233] A. Sharbatian, A. Abedini, Z. Qi, and D. Sinton, *Full characterization of co2–oil properties on-chip: solubility, diffusivity, extraction pressure, miscibility, and contact angle,* Analytical chemistry **90**, 2461 (2018).

[234] C. Chalbaud, M. Robin, J. Lombard, F. Martin, P. Egermann, and H. Bertin, *Interfacial tension measurements and wettability evaluation for geological co2 storage,* Adv. Water Resour. **32**, 98 (2009).

[235] R. Hu, J. Wan, Y. Kim, and T. K. Tokunaga, *Wettability effects on supercritical co2–brine immiscible displacement during drainage: Pore-scale observation and 3d simulation,* Int. J. Greenh. Gas Control **60**, 129 (2017).

[236] B. Gutiérrez, F. Juarez, L. Ornelas, S. Zeppieri, and A. L. De Ramos, *Experimental study of gas–liquid two-phase flow in glass micromodels,* Int. J. Thermophys. **29**, 2126 (2008).

[237] M. Ferer, C. Ji, G. S. Bromhal, J. Cook, G. Ahmadi, and D. H. Smith, *Crossover from capillary fingering to viscous fingering for immiscible unstable flow: Experiment and modeling,* Phys. Rev. E **70**, 016303 (2004).

[238] C. Zhang, M. Oostrom, T. W. Wietsma, J. W. Grate, and M. G. Warner, *Influence of viscous and capillary forces on immiscible fluid displacement: Pore-scale experimental study in a water-wet micromodel demonstrating viscous and capillary fingering,* Energy & Fuels **25**, 3493 (2011).

[239] V. Joekar Niasar, S. Hassanizadeh, L. Pyrak-Nolte, and C. Berentsen, *Simulating drainage and imbibition experiments in a high-porosity micromodel using an unstructured pore network model,* Water resources research **45** (2009).

[240] B. E. Rapp, *Microfluidics: modeling, mechanics and mathematics* (William Andrew, 2016).

[241] Imperial College London, *Micro-ct images and networks,* http://www.imperial.ac.uk/earth-science/research/research-groups/perm/research/pore-scale-modelling/micro-ct-images-and-networks (2022).

[242] A. E. Peksa, K.-H. A. Wolf, and P. L. Zitha, *Bentheimer sandstone revisited for experimental purposes,* Marine and Petroleum Geology **67**, 701 (2015).

[243] W. Yan, G.-Y. Zhao, G.-J. Chen, and T.-M. Guo, *Interfacial tension of (methane+ nitrogen)+ water and (carbon dioxide+ nitrogen)+ water systems,* J. Chem. Eng. Data **46**, 1544 (2001).

[244] E. Yusibani, Y. Nagahama, M. Kohno, Y. Takata, P. L. Woodfield, K. Shinzato, and M. Fujii, *A capillary tube viscometer designed for measurements of hydrogen gas viscosity at high pressure and high temperature,* Int. J. of Thermophys. **32**, 1111 (2011).

[245] M. Darzi and C. Park, *Optical distortion correction of a liquid-gas interface and contact angle in cylindrical tubes,* Physics of Fluids **29**, 052004 (2017).

[246] V. Heiskanen, K. Marjanen, and P. Kallio, *Machine vision based measurement of dynamic contact angles in microchannel flows,* J. Bionic Eng. **5**, 282 (2008).

[247] G. Hirasaki, *Wettability: fundamentals and surface forces,* SPE formation evaluation **6**, 217 (1991).

[248] C. Garing and S. Benson, *Co2 wettability of sandstones: Addressing conflicting capillary behaviors,* Geophysical Research Letters **46**, 776 (2019).

[249] A. Al-Menhali, B. Niu, and S. Krevor, *Capillarity and wetting of carbon dioxide and brine during drainage in b erea sandstone at reservoir conditions,* Water Resources Research **51**, 7895 (2015).

[250] Y. F. Chow, G. C. Maitland, and J. M. Trusler, *Interfacial tensions of (h2o+ h2) and (h2o+ co2+ h2) systems at temperatures of (298–448) k and pressures up to 45 mpa,* Fluid Phase Equilibria **475**, 37 (2018).

[251] W. A. van Rooijen, P. Fu, Y. Wang, and H. Hajibeygi, *Dynamic simulation of hydrogen trapping in bifurcating water-wet microchannels using the lattice boltzmann method,* Int. J. Hydrogen Energy **177**, 151274 (2025).

[252] A. Raza, M. Arif, G. Glatz, M. Mahmoud, M. Al Kobaisi, S. Alafnan, and S. Iglauer, *A holistic overview of underground hydrogen storage: Influencing factors, current understanding, and outlook,* Fuel **330**, 125636 (2022).

[253] M. Boon, T. Rademaker, C. W. Winardhi, and H. Hajibeygi, *Multiscale experimental study of h2/brine multiphase flow in porous rock characterizing relative permeability hysteresis, hydrogen dissolution, and ostwald ripening,* Sci. Rep. **14**, 1 (2024).

[254] A. Al-Yaseri, N. Yekeen, H. Al-Mukainah, M. Sarmadivaleh, and M. Lebedev, *Snap-off effects and high hydrogen residual trapping: Implications for underground hydrogen storage in sandstone aquifer,* Energy Fuels (2024).

[255] S. Higgs, Y. Da Wang, C. Sun, J. Ennis-King, S. J. Jackson, R. T. Armstrong, and P. Mostaghimi, *Comparative analysis of hydrogen, methane and nitrogen relative permeability: Implications for underground hydrogen storage,* J Energy Storage **73**, 108827 (2023).

[256] A. Al-Yaseri, L. Esteban, A. Giwelli, J. Sarout, M. Lebedev, and M. Sarmadivaleh, *Initial and residual trapping of hydrogen and nitrogen in fontainebleau sandstone using nuclear magnetic resonance core flooding,* Int. J. Hydrogen Energy **47**, 22482 (2022).

[257] M. Lysyy, N. Liu, C. M. Solstad, M. A. Fernø, and G. Ersland, *Microfluidic hydrogen storage capacity and residual trapping during cyclic injections: Implications for underground storage,* Int. J. Hydrogen Energy **48**, 31294 (2023).

[258] N. K. Jha, A. Al-Yaseri, M. Ghasemi, D. Al-Bayati, M. Lebedev, and M. Sarmadivaleh, *Pore scale investigation of hydrogen injection in sandstone via x-ray micro-tomography,* Int. J. Hydrogen Energy **46**, 34822 (2021).

[259] Z. Jangda, H. Menke, A. Busch, S. Geiger, T. Bultreys, H. Lewis, and K. Singh, *Pore-scale visualization of hydrogen storage in a sandstone at subsurface pressure and temperature conditions: Trapping, dissolution and wettability,* J Colloid Interface Sci **629**, 316 (2023).

[260] S. Krevor, M. J. Blunt, S. M. Benson, C. H. Pentland, C. Reynolds, A. Al-Menhali, and B. Niu, *Capillary trapping for geologic carbon dioxide storage–from pore scale physics to field scale implications,* Int. J. Greenh. Gas Control **40**, 221 (2015).

[261] S. Yu, M. Hu, C. I. Steefel, and I. Battiato, *Unraveling residual trapping for geologic hydrogen storage and production using pore-scale modeling,* Adv. Water Resour. , 104659 (2024).

[262] I. Chatzis, N. R. Morrow, and H. T. Lim, *Magnitude and detailed structure of residual oil saturation,* Soc Petrol Eng J **23**, 311 (1983).

[263] H. Ni, M. Boon, C. Garing, and S. M. Benson, *Predicting CO_2 residual trapping ability based on experimental petrophysical properties for different sandstone types,* Int. J. Greenh. Gas Control **86**, 158 (2019).

[264] W. Rose and P. A. Witherspoon, *Studies of waterflood performance ii. trapping oil in a pore doublet.* Circ no. 224 (1956).

[265] W. Rose and J. Cleary, *Further indications of pore doublet theory,* Prod Mon **22**, 20 (1958).

[266] T. Moore and R. Slobod, *Displacement of oil by water-effect of wettability, rate, and viscosity on recovery,* in *SPE Annual Technical Conference and Exhibition* (SPE, 1955) pp. SPE–502.

[267] F. A. Dullien, *Porous media: fluid transport and pore structure* (Academic press, 2012).

[268] I. Chatzis and F. Dullien, *Dynamic immiscible displacement mechanisms in pore doublets: theory versus experiment,* J Colloid Interface Sci **91**, 199 (1983).

[269] F. Shan, Z. Chai, B. Shi, and M. Zhao, *Optimal displacement of immiscible two-phase fluids in a pore doublet,* Phys. Fluids **35** (2023).

[270] Q. Gu, H. Liu, and L. Wu, *Preferential imbibition in a dual-permeability pore network,* J. Fluid Mech. **915**, A138 (2021).

[271] I. Chatzis, M. Kuntamukkula, and N. Morrow, *Effect of capillary number on the microstructure of residual oil in strongly water-wet sandstones,* SPE Reserv Eng **3**, 902 (1988).

[272] G. L. Stegemeier, *Relationship of trapped oil saturation to petrophysical properties of porous media,* in *SPE Improved Oil Recovery Conference* (SPE, 1974) pp. SPE–4754.

[273] C. H. Pentland, R. El-Maghraby, A. Georgiadis, S. Iglauer, and M. J. Blunt, *Immiscible displacements and capillary trapping in CO_2 storage,* Energy Procedia **4**, 4969 (2011).

[274] J.-Q. Shi, Z. Xue, and S. Durucan, *Supercritical CO_2 core flooding and imbibition in Berea sandstone—CT imaging and numerical simulation,* Energy Procedia **4**, 5001 (2011).

[275] A. Mehmani, S. Kelly, C. Torres-Verdín, and M. Balhoff, *Capillary trapping following imbibition in porous media: Microfluidic quantification of the impact of pore-scale surface roughness,* Water Resour. Res. **55**, 9905 (2019).

[276] M. Buchgraber, A. R. Kovscek, and L. M. Castanier, *A study of microscale gas trapping using etched silicon micromodels,* Transport Porous Media **95**, 647 (2012).

[277] S. Berg, M. Rücker, H. Ott, A. Georgiadis, H. Van der Linde, F. Enzmann, M. Kersten, R. T. Armstrong, S. De With, J. Becker, *et al.*, *Connected pathway relative permeability from pore-scale imaging of imbibition,* Adv. Water Resour. **90**, 24 (2016).

[278] J. Wang, Y. Yang, S. Cai, J. Yao, and Q. Xie, *Pore-scale modelling on hydrogen transport in porous media: Implications for hydrogen storage in saline aquifers,* Int. J. Hydrogen Energy **48**, 13922 (2023).

[279] M. Sussman, P. Smereka, and S. Osher, *A level set approach for computing solutions to incompressible two-phase flow,* J Comput Phys **114**, 146 (1994).

[280] D. L. Youngs, *Time-dependent multi-material flow with large fluid distortion,* Numer Methods Fluid Dyn (1982), https://api.semanticscholar.org/CorpusID:228295665.

[281] M. Tavares, C. Josserand, A. Limare, J. M. Lopez-Herrera, and S. Popinet, *A coupled vof/embedded boundary method to model two-phase flows on arbitrary solid surfaces,* Computers Fluids , 106317 (2024).

[282] L. Chen, Q. Kang, Y. Mu, Y.-L. He, and W.-Q. Tao, *A critical review of the pseudopotential multiphase lattice boltzmann model: Methods and applications,* Int. J. Heat Mass Transf. **76**, 210 (2014).

[283] T. Ramstad, N. Idowu, C. Nardi, and P.-E. Øren, *Relative permeability calculations from two-phase flow simulations directly on digital images of porous rocks,* Transport Porous Media **94**, 487 (2012).

[284] H. Huang, Z. Li, S. Liu, and X.-y. Lu, *Shan-and-chen-type multiphase lattice boltzmann study of viscous coupling effects for two-phase flow in porous media,* Int. J. Numer. Methods Fluids **61**, 341 (2009).

[285] Y. Wang and S. A. Aryana, *Pore-scale simulation of gas flow in microscopic permeable media with complex geometries,* J. Nat. Gas Sci. Eng. **81**, 103441 (2020).

[286] H. Wang, S. Chen, P. Deng, M. Wang, and Z. Xu, *Pore-scale investigation of caprock integrity in underground hydrogen storage,* in *SPE Canadian Energy Technology Conference* (SPE, 2024) p. D021S026R005.

[287] H. Song, Y. Zhou, Z. Xie, J. Lao, and M. Yue, *A pore-scale simulation of the effect of heterogeneity on underground hydrogen storage,* Water **16**, 3264 (2024).

[288] M. Lysyy, G. Ersland, and M. Fernø, *Pore-scale dynamics for underground porous media hydrogen storage,* Adv. Water Resour. **163**, 104167 (2022).

[289] Q. Zhao, H. Wang, and C. Chen, *Underground hydrogen storage: a recovery prediction using pore network modeling and machine learning,* Fuel **357**, 130051 (2024).

[290] E. M. Thaysen, I. B. Butler, A. Hassanpouryouzband, D. Freitas, F. Alvarez-Borges, S. Krevor, N. Heinemann, R. Atwood, and K. Edlmann, *Pore-scale imaging of hydrogen displacement and trapping in porous media,* Int. J. Hydrogen Energy **48**, 3091 (2023).

[291] M. Bagheri, H. Mahani, S. Ayatollahi, and D. Zivar, *Direct pore-scale simulation of the effect of capillary number and gas compressibility on cyclic underground hydrogen storage & production in heterogeneous aquifers,* Adv. Water Resour. **181**, 104547 (2023).

[292] H. Liu, A. J. Valocchi, C. Werth, Q. Kang, and M. Oostrom, *Pore-scale simulation of liquid CO_2 displacement of water using a two-phase lattice Boltzmann model,* Adv. Water Resour. **73**, 144 (2014).

[293] Z. Xu, H. Liu, and A. J. Valocchi, *Lattice boltzmann simulation of immiscible two-phase flow with capillary valve effect in porous media,* Water Resour. Res. **53**, 3770 (2017).

[294] A. K. Gunstensen, D. H. Rothman, S. Zaleski, and G. Zanetti, *Lattice boltzmann model of immiscible fluids,* Phys. Rev. A **43**, 4320 (1991).

[295] D. d'Humières, *Generalized lattice-boltzmann equations,* in *Rarefied Gas Dynamics: Theory and Simulations*, Vol. 159, edited by B. D. Shizgal and D. P. Weaver (AIAA, Washington, DC, 1992) pp. 450–458.

[296] P. Lallemand and L.-S. Luo, *Theory of the lattice boltzmann method: Dispersion, dissipation, isotropy, galilean invariance, and stability,* Phys. Rev. E **61**, 6546 (2000).

[297] Z. Chai and B. Shi, *Multiple-relaxation-time lattice boltzmann method for the navier-stokes and nonlinear convection-diffusion equations: Modeling, analysis, and elements,* Phys. Rev. E **102**, 023306 (2020).

[298] D. d'Humières, I. Ginzburg, M. Krafczyk, P. Lallemand, and L. Luo, *Multiple-relaxation-time lattice boltzmann models in three dimensions,* Philos. Trans. R. Soc. A **360**, 437 (2002).

[299] Z. Yu and L.-S. Fan, *Multirelaxation-time interaction-potential-based lattice boltzmann model for two-phase flow,* Phys. Rev. E **82**, 046708 (2010).

[300] Z. Guo, C. Zheng, and B. Shi, *Discrete lattice effects on the forcing term in the lattice boltzmann method,* Phys. Rev. E **65**, 046308 (2002).

[301] J. U. Brackbill, D. B. Kothe, and C. Zemach, *A continuum method for modeling surface tension,* J. Comput. Phys. **100**, 335 (1992).

[302] S. V. Lishchuk, C. M. Care, and I. Halliday, *Lattice boltzmann algorithm for surface tension with greatly reduced microcurrents,* Phys. Rev. E **67**, 036701 (2003).

[303] M. Latva-Kokko and D. H. Rothman, *Diffusion properties of gradient-based lattice boltzmann models of immiscible fluids,* Phys. Rev. E **71**, 056702 (2005).

[304] S. Iglauer, *Optimum geological storage depths for structural H_2 geo-storage,* J. Pet. Sci. Eng. **212**, 109498 (2022).

[305] F. Haeri, D. Tapriyal, S. Sanguinito, F. Shi, S. J. Fuchs, L. E. Dalton, J. Baltrus, B. Howard, D. Crandall, C. Matranga, *et al.*, *CO_2-brine contact angle measurements on navajo, nugget, bentheimer, bandera brown, berea, and mt. simon sandstones,* Energy Fuels **34**, 6085 (2020).

[306] Q. Zhao, R. Guo, N. K. Jha, M. Sarmadivaleh, M. Lebedev, A. Al-Yaseri, J. McClure, and C. Chen, *Using X-ray computed tomography and pore-scale numerical modeling to study the role of heterogeneous rock surface wettability on hydrogen-brine two-phase flow in underground hydrogen storage,* Fuel **366**, 131414 (2024).

[307] J. Zhao, F. Qin, R. Fischer, Q. Kang, D. Derome, and J. Carmeliet, *Spontaneous imbibition in a square tube with corner films: Theoretical model and numerical simulation,* Water Resour. Res. **57**, e2020WR029190 (2021).

[308] E. W. Lemmon, M. L. Huber, and M. O. McLinden, *Nist reference fluid thermodynamic and transport properties–refprop,* NIST Stand. Ref. database **23**, v7 (2002).

[309] V. Mirchi, M. Dejam, and V. Alvarado, *Interfacial tension and contact angle measurements for hydrogen-methane mixtures/brine/oil-wet rocks at reservoir conditions,* Int. J. Hydrogen Energy **47**, 34963 (2022).

[310] Q. Niu, Z. Dong, Q. Lv, F. Zhang, H. Shen, Z. Yang, M. Lin, J. Zhang, and K. Xiao, *Role of interfacial and bulk properties of long-chain viscoelastic surfactant in stabilization mechanism of CO_2 foam for ccus,* J. CO2 Util. **66**, 102297 (2022).

[311] Z. Wang, *Immiscible fluid displacement: From pore doublets to porous media,* Capillarity **15**, 1 (2025).

[312] Q. Zou and X. He, *On pressure and velocity boundary conditions for the lattice boltzmann bgk model,* Phys. Fluids **9**, 1591 (1997).

[313] Y. Zong, M. Li, and K. Wang, *Outflow boundary condition of multiphase microfluidic flow based on phase ratio equation in lattice boltzmann method,* Phys. Fluids **33**, 073304 (2021).

[314] A. Ladd, *Numerical simulations of particulate suspensions via a discretized boltzmann equation. part 1. theoretical foundation,* J. Fluid Mech. **271**, 285 (1994).

[315] A. Ladd, *Numerical simulations of particulate suspensions via a discretized boltzmann equation. part 2. numerical results,* J. Fluid Mech. **271**, 311 (1994).

[316] I. Gomez Mendez, W. M. El-Sayed, A. H. Menefee, and Z. T. Karpyn, *Insights into underground hydrogen storage challenges: A review on hydrodynamic and biogeochemical experiments in porous media,* Energy Fuels **38**, 20015 (2024).

[317] T. Moore and R. Slobod, *The effect of viscosity and capillarity on the displacement of oil by water,* Prod. Month **20**, 20 (1956).

[318] N. R. Morrow, I. Chatzis, and J. Taber, *Entrapment and mobilization of residual oil in bead packs,* SPE Res. Eng. **3**, 927 (1988).

[319] T. Suekane, N. Zhou, T. Hosokawa, and T. Matsumoto, *Direct observation of trapped gas bubbles by capillarity in sandy porous media,* Transp. Porous Media **82**, 111 (2010).

[320] A. L. Herring, E. J. Harper, L. Andersson, A. Sheppard, B. K. Bay, and D. Wildenschild, *Effect of fluid topology on residual nonwetting phase trapping: Implications for geologic CO_2 sequestration,* Adv. Water. Resour. **62**, 47 (2013).

[321] R. G. Hughes and M. J. Blunt, *Pore scale modeling of rate effects in imbibition,* Transp. Porous Media **40**, 295 (2000).

[322] A. Hassanpouryouzband, M. Wilkinson, and R. S. Haszeldine, *Hydrogen energy futures – foraging or farming?* Chem. Soc. Rev. **53**, 2258 (2024).

[323] A. Hassanpouryouzband, M. Jahanbani Veshareh, M. Wilkinson, H. M. Nick, B. T. Ngwenya, and R. S. Haszeldine, *In situ hydrogen generation from underground fossil hydrocarbons,* Joule (2025).

[324] W. A. van Rooijen and H. Hajibeygi, *Site selection for underground hydrogen storage in porous media: Critical review and outlook,* Energy Fuels **39**, 19600 (2025).

[325] D. Bennion, F. Thomas, T. Ma, and D. Imer, *Detailed protocol for the screening and selection of gas storage reservoirs,* in *SPE Unconventional Resources Conference/Gas Technology Symposium* (SPE, 2000) pp. SPE–59738.

[326] A. S. Lord, *Overview of geologic storage of natural gas with an emphasis on assessing the feasibility of storing hydrogen.*, Tech. Rep. (Sandia National Laboratories (SNL), Albuquerque, NM, and Livermore, CA (United States), 2009).

[327] J. Lewandowska-Śmierzchalska, S. Nagy, and B. Uliasz-Misiak, *Screening of sites for advanced natural gas and carbon dioxide storage in deep aquifers,* Int. J. Greenhouse Gas Control **132**, 104078 (2024).

[328] C. Callas, S. D. Saltzer, J. S. Davis, S. S. Hashemi, A. R. Kovscek, E. R. Okoroafor, G. Wen, M. D. Zoback, and S. M. Benson, *Criteria and workflow for selecting depleted hydrocarbon reservoirs for carbon storage,* Appl. Energy **324**, 119668 (2022).

[329] S. Bachu, *Sequestration of CO_2 in geological media: criteria and approach for site selection in response to climate change,* Energy Convers. Manage. **41**, 953 (2000).

[330] J. E. Aarnes, S. Selmer-Olsen, M. E. Carpenter, and T. A. Flach, *Towards guidelines for selection, characterization and qualification of sites and projects for geological storage of CO_2,* Energy Procedia **1**, 1735 (2009).

[331] M. Carpenter, K. Kvien, and J. Aarnes, *The co2qualstore guideline for selection, characterisation and qualification of sites and projects for geological storage of CO_2,* Int. J. Greenhouse Gas Control **5**, 942 (2011).

[332] J. Watt, S. Bricker, J. Ford, D. Lawrence, D. McInroy, A. Monaghan, M. Smith, A. Curtis, M. Edwards, P. Eke, R. S. Haszeldine, D. Naylor, M. JafarGandomi, A. Polson, D. Hamilton, S. Mackay, E. Jin, M. Olden, P. Pickup, G. Somerville, J. Sohrabi, M. Todd, A. C. Vivalda, C. Campbell, D. Ockendon, M. Carey, J. Roberts, and T. Mander, *CO_2 Aquifer Storage Site Evaluation and Monitoring (CASSEM): Understanding the challenges of CO_2 storage*, Technical Report (University of Edinburgh, Edinburgh Research Archive, 2012).

[333] A. Raza, R. Rezaee, R. Gholami, C. H. Bing, R. Nagarajan, and M. A. Hamid, *A screening criterion for selection of suitable CO_2 storage sites,* J. Nat. Gas Sci. Eng. **28**, 317 (2016).

[334] Q. Li, G. Liu, X. Liu, and X. Li, *Application of a health, safety, and environmental screening and ranking framework to the shenhua ccs project,* Int. J. Greenhouse Gas Control **17**, 504 (2013).

[335] T. D. Rodosta, J. T. Litynski, S. I. Plasynski, S. Hickman, S. Frailey, and L. Myer, *Us department of energy's site screening, site selection, and initial characterization for storage of CO_2 in deep geological formations,* Energy Procedia **4**, 4664 (2011).

[336] S. Grataloup, D. Bonijoly, E. Brosse, R. Dreux, D. Garcia, V. Hasanov, M. Lescanne, P. Renoux, and A. Thoraval, *A site selection methodology for CO_2 underground storage in deep saline aquifers: case of the paris basin,* Energy Procedia **1**, 2929 (2009).

[337] B. Nemati, M. Mapar, P. Davarazar, S. Zandi, M. Davarazar, D. Jahanianfard, and M. Mohammadi, *A sustainable approach for site selection of underground hydrogen storage facilities using fuzzy-delphi methodology.* J. Settlements Spatial Planning **SI(6)**, 5 (2020).

[338] E. R. Okoroafor, S. D. Saltzer, and A. R. Kovscek, *Toward underground hydrogen storage in porous media: Reservoir engineering insights,* Int. J. Hydrogen Energy **47**, 33781 (2022).

[339] T. Amirthan and M. Perera, *Underground hydrogen storage in australia: a review on the feasibility of geological sites,* Int. J. Hydrogen Energy **48**, 4300 (2023).

[340] S. Harati, S. R. Gomari, M. Ramegowda, and T. Pak, *Multi-criteria site selection workflow for geological storage of hydrogen in depleted gas fields: A case for the uk,* Int. J. Hydrogen Energy **51**, 143 (2024).

[341] L. Lankof, K. Luboń, Y. Le Gallo, and R. Tarkowski, *The ranking of geological structures in deep aquifers of the polish lowlands for underground hydrogen storage,* Int. J. Hydrogen Energy **62**, 1089 (2024).

[342] A. Safari, Y. Sugai, M. Sarmadivaleh, and M. Imai, *Screening and ranking japanese gas fields for underground H_2 storage potential: impact of the reservoir drive mechanism,* J. Energy Storage **70**, 107679 (2023).

[343] L. K. Sekar, H. G. Silva, and E. R. Okoroafor, *Development and implementation of a comprehensive multistage ranking criteria for underground hydrogen storage in saline aquifers,* J. Energy Storage **102**, 113931 (2024).

[344] M. L. Malki, B. Chen, S. Mao, F. Chen, and M. Mehana, *Operate–H_2: A tool for optimizing underground hydrogen storage,* J. Energy Storage **90**, 111715 (2024).

[345] W. Zhao, S. Mao, and M. Mehana, *-techno-economic analysis and site screening for underground hydrogen storage in intermountain-west region, united states,* Int. J. Hydrogen Energy **109**, 275 (2025).

[346] S. Baek, L. E. Hibbard, N. J. Huerta, G. Lackey, A. Goodman, and J. A. White, *Enhancing Site Screening for Underground Hydrogen Storage: Qualitative Site Quality Assessment – SHASTA: Subsurface Hydrogen Assessment, Storage, and Technology Acceleration Project*, Tech. Rep. (2024).

[347] M. Deveci, *Site selection for hydrogen underground storage using interval type-2 hesitant fuzzy sets,* Int. J. Hydrogen Energy **43**, 9353 (2018).

[348] F. Chen, B. Chen, S. Mao, M. Malki, and M. Mehana, *Integrating capacity and efficiency for optimal hydrogen storage site selection in saline aquifers,* Energy Fuels **38**, 4733 (2024).

[349] G. C. Mwakipunda, A. K. Franck Kouassi, E. T. Ayimadu, N. A. Komba, M. N. Nadege, M. M. Mgimba, M. R. Ngata, and L. Yu, *Underground hydrogen storage in geological formations: A review,* J. Rock Mech. Geotech. Eng. (2025), in press.

[350] Z. Bo, S. Hörning, J. R. Underschultz, A. Garnett, and S. Hurter, *Effects of geological heterogeneity on gas mixing during underground hydrogen storage (uhs) in braided-fluvial reservoirs,* Fuel **357**, 129949 (2024).

[351] M. Bouteldja, T. Acosta, B. Carlier, A. Reveillere, H. Jannel, and C. Fournier, *Definition of selection criteria for a hydrogen storage site in depleted fields or aquifers,* https://ec.europa.eu/research/participants/documents/downloadPublic?documentIds=080166e5da83228d&appId=PPGMS (2021), accessed: 2025-06-25.

[352] C. R. Matos, J. F. Carneiro, and P. P. Silva, *Overview of large-scale underground energy storage technologies for integration of renewable energies and criteria for reservoir identification,* J. Energy Storage **21**, 241 (2019).

[353] S. Narayanamoorthy, L. Ramya, D. Baleanu, J. V. Kureethara, and V. Annapoorani, *Application of normal wiggly dual hesitant fuzzy sets to site selection for hydrogen underground storage,* Int. J. Hydrogen Energy **44**, 28874 (2019).

[354] K. Alms, B. Ahrens, M. Graf, and M. Nehler, *Linking geological and infrastructural requirements for large-scale underground hydrogen storage in germany,* Front. Energy Res. **11**, 1172003 (2023).

[355] L. Hibbard, J. A. White, D. G. Clarke, S. Harrison, R. A. Schultz, F. Hasiuk, A. Goodman, and N. Huerta, *Underground hydrogen storage resource assessment for the cook inlet, alaska,* Appl. Energy **377**, 124135 (2025).

[356] J. M. Nordbotten, M. A. Celia, and S. Bachu, *Injection and storage of CO_2 in deep saline aquifers: analytical solution for CO_2 plume evolution during injection,* Transp. in Porous media **58**, 339 (2005).

[357] C. Callas, A. R. Kovscek, and S. M. Benson, *Assessing the impact of dip angle on carbon storage in saline reservoirs to aid site selection,* Int. J. Greenh. Gas Control **129**, 103966 (2023).

[358] F. Feldmann, B. Hagemann, L. Ganzer, and M. Panfilov, *Numerical simulation of hydrodynamic and gas mixing processes in underground hydrogen storages,* Environ. Earth Sci. **75**, 1 (2016).

[359] E. I. Epelle, W. Obande, G. A. Udourioh, I. C. Afolabi, K. S. Desongu, U. Orivri, B. Gunes, and J. A. Okolie, *Perspectives and prospects of underground hydrogen storage and natural hydrogen,* Sust. Energy Fuels **6**, 3324 (2022).

[360] A. Hassanpouryouzband, E. Joonaki, K. Edlmann, and R. S. Haszeldine, *Offshore geological storage of hydrogen: is this our best option to achieve net-zero?* ACS Energy Lett. **6**, 2181 (2021).

[361] L. W. Lake, *Enhanced Oil Recovery* (Prentice Hall, Old Tappan, NJ, 1989).

[362] G. Løvoll, Y. Méheust, K. J. Måløy, E. Aker, and J. Schmittbuhl, *Competition of gravity, capillary and viscous forces during drainage in a two-dimensional porous medium, a pore scale study,* Energy **30**, 861 (2005).

[363] D. Or, *Scaling of capillary, gravity and viscous forces affecting flow morphology in unsaturated porous media,* Adv. Water Resour. **31**, 1129 (2008).

[364] A. L. Herring, L. Andersson, S. Schlüter, A. Sheppard, and D. Wildenschild, *Efficiently engineering pore-scale processes: The role of force dominance and topology during nonwetting phase trapping in porous media,* Adv. Water Resour. **79**, 91 (2015).

[365] L. Hashemi, M. Boon, W. Glerum, R. Farajzadeh, and H. Hajibeygi, *A comparative study for h_2–CH_4 mixture wettability in sandstone porous rocks relevant to underground hydrogen storage,* Adv. Water Resour. **163**, 104165 (2022).

[366] B. Pan, T. Song, M. Yue, S. Chen, L. Zhang, K. Edlmann, C. W. Neil, W. Zhu, and S. Iglauer, *Machine learning – based shale wettability prediction: Implications for H_2, CH_4 and CO_2 geo-storage,* Int. J. Hydrogen Energy **56**, 1384 (2024).

[367] A. P. Indro, L. K. Sekar, G. V. Matey-Korley, C. C. Ikeokwu, and E. R. Okoroafor, *A compilation of losses related to hydrogen storage in porous media: Implications for hydrogen recovery and productivity from saline aquifers,* Int. J. Hydrogen Energy **78**, 1288 (2024).

[368] A. Amid, D. Mignard, and M. Wilkinson, *Seasonal storage of hydrogen in a depleted natural gas reservoir,* Int. J. Hydrogen Energy **41**, 5549 (2016).

[369] C. Hemme and W. Van Berk, *Hydrogeochemical modeling to identify potential risks of underground hydrogen storage in depleted gas fields,* Appl. Sci. **8**, 2282 (2018).

[370] A. Sáinz-García, E. Abarca, V. Rubí, and F. Grandia, *Assessment of feasible strategies for seasonal underground hydrogen storage in a saline aquifer,* Int. J. Hydrogen Energy **42**, 16657 (2017).

[371] J. T. Camargo, J. A. White, F. P. Hamon, V. Fakeye, T. A. Buscheck, and N. Huerta, *Managing reservoir dynamics when converting natural gas fields to underground hydrogen storage,* Int. J. Hydrogen Energy **49**, 1261 (2024).

[372] R. Ershadnia, M. Singh, S. Mahmoodpour, A. Meyal, F. Moeini, S. A. Hosseini, D. M. Sturmer, M. Rasoulzadeh, Z. Dai, and M. R. Soltanian, *Impact of geological and operational conditions on underground hydrogen storage,* Int. J. Hydrogen Energy **48**, 1450 (2023).

[373] T. A. Buscheck, A. Goodman, G. Lackey, J. D. T. Camargo, N. Huerta, F. Haeri, G. M. Freeman, and J. A. White, *Underground storage of hydrogen and hydrogen/methane mixtures in porous reservoirs: Influence of reservoir factors and engineering choices on deliverability and storage operations,* Int. J. Hydrogen Energy **49**, 1088 (2024).

[374] T. Hulikal Chakrapani, H. Hajibeygi, O. A. Moultos, and T. J. H. Vlugt, *Mutual diffusivities of mixtures of carbon dioxide and hydrogen and their solubilities in brine: Insight from molecular simulations,* Ind. Eng. Chem. Res. **63**, 10456 (2024).

[375] M. Ghaedi, P. Ø. Andersen, and R. Gholami, *Maximum column height and optimum storage depth for geological storage of hydrogen,* Int. J. Hydrogen Energy **50**, 291 (2024).

[376] Z. Bo, S. Hörning, K. Tang, J. R. Underschultz, and S. Hurter, *Insights into site evaluation for underground hydrogen storage (uhs) on gas mixing-the effects of meter-scale heterogeneity and associated reservoir characterization parameters,* Fuel **391**, 134677 (2025).

[377] S. Khandoozi, P. Li, R. Ershadnia, Z. Dai, Z. Zhang, P. H. Stauffer, M. Mehana, D. R. Cole, and M. R. Soltanian, *An integrated approach for optimizing geological hydrogen storage,* Appl. Energy **381**, 125182 (2025).

[378] H. Dykstra and R. Parsons, *The prediction of oil recovery by water flood,* Sec. Recovery Oil United States **2**, 160 (1950).

[379] J. Tremosa, R. Jakobsen, and Y. Le Gallo, *Assessing and modeling hydrogen reactivity in underground hydrogen storage: A review and models simulating the lobodice town gas storage,* Front. Energy Res. **11**, 1145978 (2023).

[380] A. Shojaee, S. Ghanbari, G. Wang, and E. Mackay, *Interplay between microbial activity and geochemical reactions during underground hydrogen storage in a seawater-rich formation,* Int. J. Hydrogen Energy **50**, 1529 (2024).

[381] Z. Bo, L. Zeng, Y. Chen, and Q. Xie, *Geochemical reactions-induced hydrogen loss during underground hydrogen storage in sandstone reservoirs,* Int. J. Hydrogen Energy **46**, 19998 (2021).

[382] K. Takai, K. Nakamura, T. Toki, U. Tsunogai, M. Miyazaki, J. Miyazaki, H. Hirayama, S. Nakagawa, T. Nunoura, and K. Horikoshi, *Cell proliferation at 122 c and isotopically heavy CH_4 production by a hyperthermophilic methanogen under high-pressure cultivation,* Proc. Natl. Acad. Sci. **105**, 10949 (2008).

[383] J. Holden, *Extremophiles: Hot environments,* in *Encyclopedia of Microbiology (Third Edition)*, edited by M. Schaechter (Academic Press, Oxford, 2009) third edition ed., pp. 127–146.

[384] R. Gholami, *Hydrogen storage in geological porous media: Solubility, mineral trapping, H_2S generation and salt precipitation,* J. Energy Storage **59**, 106576 (2023).

[385] A. Hassanpouryouzband, K. Adie, T. Cowen, E. M. Thaysen, N. Heinemann, I. B. Butler, M. Wilkinson, and K. Edlmann, *Geological hydrogen storage: geochemical reactivity of hydrogen with sandstone reservoirs,* ACS Energy Lett. **7**, 2203 (2022).

[386] L. Zeng, A. Keshavarz, Q. Xie, and S. Iglauer, *Hydrogen storage in majiagou carbonate reservoir in china: Geochemical modelling on carbonate dissolution and hydrogen loss,* Int. J. Hydrogen Energy **47**, 24861 (2022).

[387] A. Al-Yaseri, H. Al-Mukainah, N. Yekeen, and A. S. Al-Qasim, *Experimental investigation of hydrogen-carbonate reactions via computerized tomography: Implications for underground hydrogen storage,* Int. J. Hydrogen Energy **48**, 3583 (2023).

[388] A. Al-Yaseri, S. Rizwanullah Hussaini, A. Fatah, A. S. Al-Qasim, and P. D. Patil, *Computerized tomography analysis of potential geochemical reactions of carbonate rocks during underground hydrogen storage,* Fuel **361**, 130680 (2024).

[389] A. Al-Yaseri, H. Al-Mukainah, and N. Yekeen, *Experimental insights into limestone-hydrogen interactions and the resultant effects on underground hydrogen storage,* Fuel **344**, 128000 (2023).

[390] J. F. Carneiro, C. R. Matos, and S. Van Gessel, *Opportunities for large-scale energy storage in geological formations in mainland portugal,* Renew. Sustain. Energy Rev. **99**, 201 (2019).

[391] Y. Wang, T. H. Chakrapani, Z. Wen, and H. Hajibeygi, *Pore-scale simulation of H_2-brine system relevant for underground hydrogen storage: A lattice Boltzmann investigation,* Adv. Water Resour. , 104756 (2024).

[392] L. K. Sekar, R. Kiran, E. R. Okoroafor, and D. A. Wood, *Review of reservoir challenges associated with subsurface hydrogen storage and recovery in depleted oil and gas reservoirs,* J. Energy Storage **72**, 108605 (2023).

[393] M. Hosseini, J. Fahimpour, M. Ali, A. Keshavarz, and S. Iglauer, *Capillary sealing efficiency analysis of caprocks: Implication for hydrogen geological storage,* Energy Fuels **36**, 4065 (2022).

[394] S. Alafnan, *Factors influencing hydrogen migration in cap rocks: Establishing new screening criteria for the selection of underground hydrogen storage locations,* Int. J. Hydrogen Energy **83**, 1099 (2024).

[395] M. Hashemi and B. Sedaee, *Understanding caprock integrity in underground hydrogen storage: A geochemical study of mineral alteration and sealing efficiency,* Int. J. Hydrogen Energy **154**, 150300 (2025).

[396] A. S. Lord, P. H. Kobos, and D. J. Borns, *Geologic storage of hydrogen: Scaling up to meet city transportation demands,* Int. J. Hydrogen Energy **39**, 15570 (2014).

[397] S. K. Mishra, G. M. Freeman, S. Ganguli, and N. J. Huerta, *Which factors dominate the levelized costs of subsurface hydrogen storage in pennsylvania, united states,* Int. J. Hydrogen Energy **91**, 814 (2024).

[398] F. Chen, Z. Ma, H. Nasrabadi, B. Chen, M. Z. S. Mehana, and J. Van Wijk, *Capacity assessment and cost analysis of geologic storage of hydrogen: A case study in intermountain-west region usa,* Int. J. Hydrogen Energy **48**, 9008 (2023).

[399] S. H. Yousefi, R. Groenenberg, J. Koornneef, J. Juez-Larré, and M. Shahi, *Techno-economic analysis of developing an underground hydrogen storage facility in depleted gas field: A dutch case study,* Int. J. Hydrogen Energy **48**, 28824 (2023).

[400] B. Baghirov, D. Voskov, and R. Farajzadeh, *Exergetic efficiency and CO_2 intensity of hydrogen supply chain including underground storage,* Energy Convers. Manage.: X **24**, 100695 (2024).

[401] M. Talukdar, P. Blum, N. Heinemann, and J. Miocic, *Techno-economic analysis of underground hydrogen storage in europe,* Iscience **27**, 108771 (2024).

[402] A. Jahanbakhsh, A. L. Potapov-Crighton, A. Mosallanezhad, N. T. Kaloorazi, and M. M. Maroto-Valer, *Underground hydrogen storage: A uk perspective,* Renew. Sustain. Energy Rev. **189**, 114001 (2024).

[403] S. Prigmore, O. A. Okon-Akan, I. P. Egharevba, C. C. Ogbaga, P. U. Okoye, E. Epelle, and J. A. Okolie, *Cushion gas consideration for underground hydrogen storage,* Encyclopedia **4**, 847 (2024).

[404] N. Heinemann, J. Scafidi, G. Pickup, E. Thaysen, A. Hassanpouryouzband, M. Wilkinson, A. Satterley, M. Booth, K. Edlmann, and R. Haszeldine, *Hydrogen storage in saline aquifers: The role of cushion gas for injection and production,* Int. J. Hydrogen Energy **46**, 39284 (2021).

[405] North Sea Energy, *North sea energy atlas,* https://north-sea-energy.eu/atlas.

[406] T. W. Kim, C. Callas, S. D. Saltzer, and A. R. Kovscek, *Assessment of oil and gas fields in california as potential CO_2 storage sites,* Int. J. Greenhouse Gas Control **114**, 103579 (2022).

[407] A. Hassanpouryouzband, T. Armitage, T. Cowen, E. M. Thaysen, S. McMahon, H. Hajibeygi, D. S. Stevenson, M. Stahl, and R. S. Haszeldine, *The search for natural hydrogen: A hidden energy giant or an elusive dream?* ACS Energy Lett. **10**, 3887 (2025).

[408] S. van Egmond and M. P. Hekkert, *Analysis of a prominent carbon storage project failure–the role of the national government as initiator and decision maker in the barendrecht case,* Int. J. Greenh. Gas Control **34**, 1 (2015).

[409] J. Berthier, D. Gosselin, and E. Berthier, *A generalization of the lucas–washburn–rideal law to composite microchannels of arbitrary cross section,* Microfluidics and Nanofluidics **19**, 497 (2015).

[410] E. Buckingham, *On physically similar systems; illustrations of the use of dimensional equations,* Phys. Rev. **4**, 345 (1914).

Acknowledgments

Four years of PhD, and more than ten years at TU Delft. It has been a very valuable journey. Along the way, I've had the support of many people who contributed to this thesis and to my personal development.

I would like to start by thanking Prof. Dr. Hadi Hajibeygi. Hadi, you noticed me during the MSc courses, started talking to me about research, and encouraged me to pursue a PhD. It was, and still is, a great honour that you took that step and saw something in me that I hadn't yet recognized myself. You gave me many opportunities throughout the PhD, set up collaborations, and enabled me to explore a wide range of projects. This meant a lot to me, and I sincerely thank you for that. I also thank Prof. Dr. Ir. Jan Dirk Jansen. I deeply valued your perspective, feedback and advice throughout the process. Thank you for your sincere interest in me and my work.

During the PhD, I had the chance to work with many people from very different fields. Various times, I joined projects without prior experience in their domain, and I'm very grateful for their patience and guidance. Special thanks to Dr. Rouhi Farajzadeh, Dr. Sian Jones, Dr. Maartje Boon, Dr. Leila Hashemi, Michiel Slob, Prof. Dr. Ir. Thijs Vlugt, Dr. Othon Moultos, Dr. Parsa Habibi, Prof. Dr. Stéphane Zaleski, Dr. Yuhang Wang, and Pengyu Fu. I would also like to thank the support staff for their help and friendliness over the years.

A good work environment matters just as much as scientific discussions, and I was fortunate to be surrounded by a diverse and amazing group of colleagues, and to develop some very valuable friendships. My thanks go to the ADMIRE group, the RSV section, and many others: Leila, Carolin, Kishan, Sara, Fanxiang, Artur, Mengjie, Thejas, Herminio, Amin, Mahsa, Saeed, Naomi, Sijmen, Filipi, Ryan, Milad, Michiel, George, Aga, Sian, Yuan, Gabriel, Patricia, David, Sajjad, Sadegh, Zahra, Xiaoming, Mohsen, Kiarash, Aleks, John, Kai, and Guofeng. It was often the chats in the office, the hallway, or during coffee breaks and lunches that made my days.

I am lucky to have many friends around me, also outside of work, and even though I do not mention all names here, I want to thank all of you. I truly appreciate having so many wonderful people in my life.

Floris, Jorien, and Emma, thank you for all your help, advice, and the fun we've had growing up together. I am very fortunate to have you as my older brother and sisters, and cherish the relationship that we have.

Papa and mama, you supported me in every way possible, and I am deeply grateful for this and the warmth you have always given me. You were feeling with me every single day, and every single step along the process. Thank you for everything.

And finally, Matthijs, the fact that you are there for me gives me confidence, strength, and happiness every day. I can't tell you enough how grateful I am to be with you.

Willemijn
Delft, August 2025

Curriculum Vitæ

Willemijn Adriënne van Rooijen

1996/08/19 Date of birth, Nieuwegein, The Netherlands

Education

2021 - 2025 **PhD Underground Hydrogen Storage**
Delft University of Technology, Delft, The Netherlands

Promotor: Prof. Dr. H. Hajibeygi
Promotor: Em. Prof. Dr. Ir. J. D. Jansen

2019 - 2021 **MSc Geo-Energy Engineering**
Delft University of Technology, Delft, The Netherlands

2016 **Minor Environmental Engineering**
KTH Royal Institue of Technology, Stockholm, Sweden

2014 - 2017 **BSc Applied Earth Sciences**
Delft University of Technology, Delft, The Netherlands

Work experience and Internships

2024 **Guest PhD Researcher: Volume of Fluid Method**
Sorbonne Université, Paris, France

2020 - 2021 **Research Intern: Lithium mining in Geothermal Systems**
GFZ, Potsdam, Germany

2018 - 2021 **Geothermal Engineer**
Veegeo Geothermal Energy (Currently Sproule),
Rotterdam, The Netherlands

Scientific Contributions

Journal papers

5. **Van Rooijen, W.A.**, Hajibeygi, H. (2025). Site Selection for Underground Hydrogen Storage in Porous Media: Critical Review and Outlook. *Energy & Fuels,* 39(41), 19600-19613..
4. **Van Rooijen, W.A.**, Fu, P., Wang, Y., Hajibeygi, H. (2025). Dynamic simulation of hydrogen trapping in bifurcating water-wet microchannels using the lattice Boltzmann method. *International Journal of Hydrogen Energy,* 177, 151274.
3. Bonabi, A. M.,**Van Rooijen, W.A.**, Al Kobaisi, M., Vuik, C., Hajibeygi, H. (2025). Comparative analysis of carbon dioxide and hydrogen plume migration in aquifers inspired by the FluidFlower benchmark study. *International Journal of Hydrogen Energy,* 135, 56-68.
2. **Van Rooijen, W.A.**, Habibi, P., Xu, K., Dey, P., Vlugt, T. J. H., Hajibeygi, H., Moultos, O. A. (2023). Interfacial tensions, solubilities, and transport properties of the H_2/H_2O/NaCl system: A molecular simulation study. *Journal of Chemical & Engineering Data*, 69(2), 307-319.
1. **Van Rooijen, W.A.**, Hashemi, L., Boon, M., Farajzadeh, R., Hajibeygi, H. (2022). Microfluidics-based analysis of dynamic contact angles relevant for underground hydrogen storage. *Advances in Water Resources*, 164, 104221.

Conferences

4. **Van Rooijen, W.A.**, Fu, P., Wang, Y., Hajibeygi, H. (2025). Micro-scale transport of H_2-Brine multiphase flow in porous media, Burgers Symposium 2025, Lunteren, The Netherlands.
3. **Van Rooijen, W.A.**, Chen. X., Han. T., Hajibeygi, H., Zaleski, S., (2024). VOF-based study of the three-phase contact line. Interpore conference 2024, Qindao, China
2. **Van Rooijen, W.A.**, Habibi, P., Xu, K., Dey, P., Vlugt, T. J. H., Hajibeygi, H., Moultos, O. A. (2023). Thermodynamics of Underground Hydrogen Storage. Interpore Conference 2023, Edinburgh, Scotland.
1. **Van Rooijen, W.A.**, Hashemi, L., Boon, M., Farajzadeh, R., Hajibeygi, H. (2022). Microfluidics-based analyses of underground hydrogen storage: dynamic contact angles. Interpore Conference 2022, Abu Dhabi, United Arab Emirates.